Title

An Integrated Multiscale Modeling Framework for Unconventional Stimulation and Production

Authors

Birkholzer, Jens
Morris, Joseph
Bargar, John
et al.

Publication Date

2021-12-30

Peer reviewed

Final Project Report

An Integrated Multiscale Modeling Framework for Unconventional Stimulation and Production

J.T. Birkholzer[1], J. Morris[2], J.R. Bargar[3], F. Brondolo[3], A. Cihan[1], D. Crandall[4], H. Deng[1], W. Fan[3], W. Fu[2], P. Fu[2], A. Hakala[4], Y. Hao[2], J. Huang[2], A.D. Jew[3], T. Kneafsey[1], Z. Li[1], C. Lopano[4], J. Moore[4], G. Moridis[1], S. Nakagawa[1], V. Noël[3], M. Reagan[1], C.S. Sherman[2], R. Settgast[2], C. Steefel[1], M. Voltolini[1], W. Xiong[4]

[1] *Lawrence Berkeley National Laboratory, Berkeley, CA, USA*
[2] *Lawrence Livermore National Laboratory, Livermore, CA, USA*
[3] *SLAC National Accelerator Laboratory, Menlo Park, CA, USA*
[4] *National Energy Technology Laboratory, Pittsburgh, PA, USA and Morgantown, WV, USA*

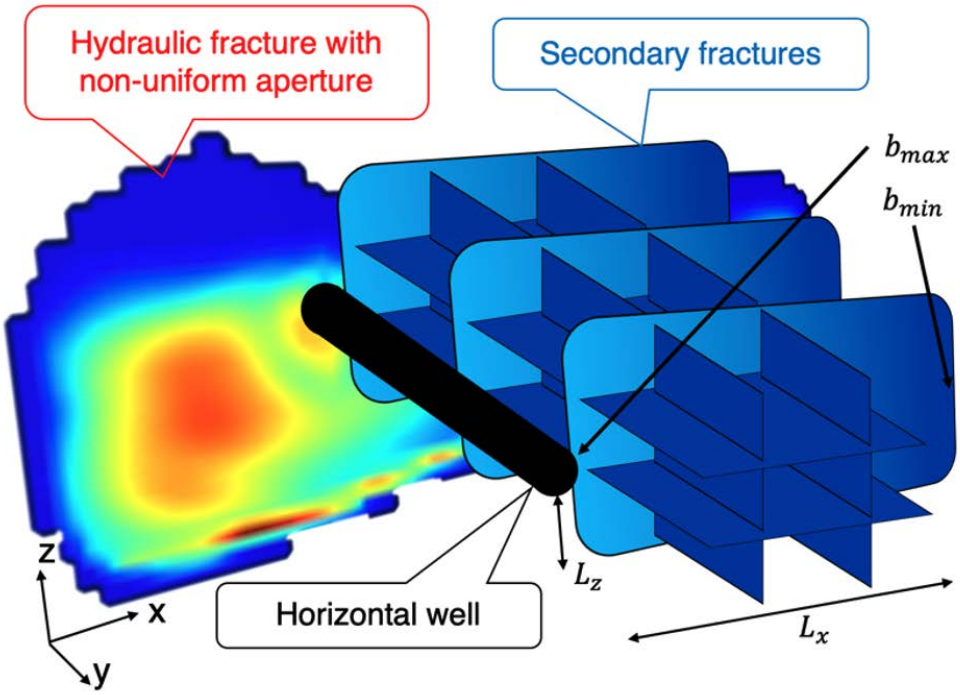

December 30, 2021

This page intentionally left empty.

Executive Summary

The production of oil and gas from unconventional reservoirs largely depends upon two main features operating at different scales: (1) the establishment of a reservoir scale stimulated fracture network that effectively communicates with the rock volume, enhancing permeability and transport to the wellbore and (2) the coupled multi-phase flow, chemical and mechanical processes affecting the migration of hydrocarbons from the low permeability country rock adjacent to the stimulated fracture network. To date, there has been no simulation framework that allows seamless and integrated prediction of these features across spatial scales extending from the pore structure of the reservoir rock to the volume of the reservoir. In addition, there has been a lack of suitable field measurements to test such models, as stimulation and production data are often proprietary and not freely available to national laboratories and academic institutions. New multi-scale simulation capabilities are needed that are validated against suitable field-based research experiments on hydraulic fracturing and shale production.

This report summarizes a multi-lab effort to develop and demonstrate such multi-scale simulation capabilities. The resulting product is an advanced modeling framework for microscopic to reservoir-scale simulations of hydraulic fracturing and hydrocarbon production. The approach builds upon a fusion of two existing high-performance simulators for reservoir-scale behavior: the GEOS code for hydromechanical evolution during stimulation and the TOUGH+ code for multi-phase flow during production. The reservoir-scale simulations are informed by experimental and modeling studies at the laboratory scale to incorporate important micro-scale mechanical processes and chemical reactions occurring within the fractures, the shale matrix, and at the fracture-fluid interfaces. These processes include, among others, changes in stimulated fracture permeability as a result of proppant behavior rearrangement or embedment, and mineral scale precipitation within pores and microfractures, at μm to cm scales. In the new modeling framework, such micro-scale testing and modeling provides upscaled hydro-mechanical parameters for the reservoir scale models. Testing of the new modeling framework has been done using high-quality field data and core samples from the Hydraulic Fracturing Field Test (HFTS), a field-based joint research experiment with intense monitoring of hydraulic fracturing and shale production in the Wolfcamp Formation in the Permian Basin, USA.

This report presents the approach coupling the reservoir simulators GEOS and TOUGH+ informed by upscaled parameters from micro-scale experiments and modeling, provides a brief overview of the HFTS and the available field data, and then describes the project findings and achievements made in four critical interconnected areas: (1) reservoir-scale hydraulic fracturing modeling, (2) reservoir-scale production modeling, (3) micro- and mesoscale fracture and proppant mechanics, and (4) micro-scale reactions within fractures and at fracture-matrix interfaces. While the modeling framework is applied to hydraulic fracturing and production, the new coupled simulation capabilities have broad applicability across multiple other subsurface applications, such as subsurface energy storage, geologic carbon sequestration, geothermal energy production, or waste isolation. The three-year project described in this report has been a close collaboration of four of DOE's national labs, namely Lawrence Berkeley National Laboratory (LBNL), Lawrence Livermore National Laboratory (LLNL), National Energy Technology Laboratory (NETL), and SLAC National Accelerator Laboratory (SLAC).

Table of Contents

List of Figures

Figure 4.7: The interaction between a main hydraulic fracture and potential child fractures initiated near the main fracture. Each of the child fractures is 12 m "tall". The horizontal distance between the main fracture and the child fractures varies between 5 m and 40 m. The values in the figure are stress intensity factors (in $MPa \cdot m^{0.5}$) at fracture tips. The deformation is exaggerated by 1000 times. A negative SIF value indicates the fracture should be closed near this tip.

Figure 4.8: A conceptual illustration of hypothetical mechanism #3 for generating closely-spaced parallel hydraulic fractures. Rock Layer A and Layer B have misaligned S_{hmin} orientations. The three rod dots denote where Fracture A spins off three parallel fractures in Layer B.

Figure 4.9: Example results from the near-wellbore fracture imitation sensitivity analysis for a model containing eight initial perforations aligned 45° from the direction of the far-field σ_{hmin}. For each fracture cluster, we show (a) the pressure at the perforation, (b) the maximum radius, (c) the maximum aperture over time, and (d) a 3D snapshot of the fractures after 12.5 seconds of pumping (showing aperture in color, with an exaggerated scale in the z-direction).

Figure 4.10: Results from near wellbore fracture initiation models each with eight perforations aligned at different angles with respect to the far-field σ_{hmin}.

Figure 5.1: Illustration of the proposed secondary fracture model, with (a) a concept figure shows the spatial relation between the primary hydraulic fracture, the secondary fracture network and the horizontal well, and (b) the multi-scale fracture network represented on MINC mesh, where the dashed boxes represent computational grids, red color represents the hydraulic fracture, blue color represents the fracture of the MINC grids and orange color represents the matrix of the MINC grids. White arrows indicate flow direction. Color gradients indicate non-uniform permeability, with darker color implying smaller permeability.

Figure 5.2: Geometry of the two hydraulic fractures used in this study. The colormap indicates the magnitude of aperture (mm). The first column (a, d) shows the propped aperture modeled with GEOS. The second column (b, e) shows the corresponding modified aperture. The third column (c, f) shows the closed aperture, where the unpropped region is removed. The black dots represent the wellbore. The red dots are pressure monitoring locations.

Figure 5.3: Cumulative production of (a) water, (b) gas and (c) oil from well 4SM. The parameters for the secondary fractures and the oil saturation are adjusted to investigate their effects on history matching.

Figure 5.4: Cumulative production of (a) water, (b) gas and (c) oil from well 4SM. At 150 days, the fracture properties are changed from the 4M Base scenario to represent fracture closure.

Figure 5.5: Cumulative production of (a) water, (b) gas and (c) oil from well 4SU. At 150 days, the fracture properties are changed from the 4U Base scenario to represent fracture closure.

Figure 5.5: Cumulative production of (a) water, (b) gas and (c) oil from well 4SU. At 150 days, the fracture properties are changed from the 4U Base scenario to represent fracture closure.

Figure 6.1: a) the compliance curve of an indentation experiment (Green River shale) with white point representing radiographs and red points representing tomographic scans. b) the pressure on the indenter imprint (equivalent to the Meyer's hardness) as a function of the applied load.

Figure 6.2: Series of volume renderings (Green River shale) showing the sample at zero loading (top row), and maximum load (bottom). From left to right, the volume renderings display the sample as: viewed from the top, virtually cut normal with respect to the bedding, under the indenter tip, and cut parallel to the bedding.

Figure 6.3: Volume renderings of the sample at the end of the loading cycle. The vertical section (normal to the bedding) volume rendering of the sample (in grays) has been overlaid with the cumulative local strain along Z (left) and radial (right), in color scale.

Figure 6.4: Custom radiolucent triaxial holder for µCT. Confining stress is applied to the outer cylindrical surface of the ~0.6 cm diameter sample contained in the holder, and axial stress is imposed using the axial loading piston. This setup enables in situ imaging experiments (right).

Figure 6.5: µCT images of the initial (a) and final (b) states of the application of increasing axial stress on a confined Eagle Ford sample. Warmer colors indicate more rapid computed flow. Calculated normalized permeability plot is shown in (c).

Figure 6.6: Top – tomographic data sets showing fracture closure as temperature increases. Bottom - Applied temperature (red) and aperture (green) of the sample over time. Circles represents tomographic datasets shown above.

Figure 6.7: Scanning electron micrograph (back-scattered electrons/energy dispersive X-ray spectroscopy -SEM BSE/EDS) image with overlaid map of carbonates (red) in the sample. Orientation of bedding is vertical. Notice the absence of carbonates in proximity with the surface as a result of the acid.

Figure 6.8: Example showing the evolution of the active proppant grains (red) and proppant-shale contact areas (yellow) in the proppant layer between two different stages of the fracture forced closure.

Figure 6.9: The results of the analysis of the stress evolution in the two propped fracture closure sequences (pristine and acid-treated weathered).

Figure 6.10: MicroCT image of acid-treated calcite-rich sample (field of view ~ 4 mm).

Figure 6.11: MicroCT image of acid-treated clay-rich sample. Note: the weathered layer (darker grey) is on the top of the sample.

Figure 6.12: Top left, right - images of fracture closure experiments for pristine, and acid-treated shale samples. bottom left. Computed flow through the propped fracture with warmer colors indicating greater flow. bottom right. Normalized fracture conductivity comparison of for the acid treated and pristine samples.

Figure 6.13: Proppant (quartz sand) shattering and fracture development in the shale during loading.

Figure 6.14: Mineralogical compositions of two types of Wolfcamp shale used in the experiment. Samples 3P (HFTS-3P) and 16P (HFTS-16P) have similar, relatively high carbonate contents (~25%). In contrast, sample 11P (HFTS-11P) contains a large percentage of clay (~37%) with little carbonate. Samples 3P and 11P have approximately same abundance of lithics (55–56%).

Figure 6.15: Wolfcamp shale discs (diameter=44.4 mm, thickness=6.4 mm) used in the experiment. Clay-rich HFTS-11Pa and 11Pb samples and carbonate-rich HFTS16a and 16b samples had a visibly smooth and homogenous texture. In contrast, carbonate-rich HFTS-3Pa and 3Pb samples exhibited heterogeneous layers.

Figure 6.16: Images of microscopic regions of the acid-treated sample surfaces. The height of the images is 500 µm. Compared to the clay-rich 11Pb (a) and the clay-rich zone in 3Pb (e), pyrite and carbonate-rich zones of 3Pb (c and d, respectively) exhibit a strong impact of dissolution by acid. Note that the pyrite-rich layer also contains a large amount of carbonate mineral grains. Pyrite itself showed little dissolution. Sample 16Pb shows less dissolution than 3Pb, with smaller pore sizes.

Figure 6.17: A schematic view of a propped shale fracture under compression. The top half of the fracture is replaced by transparent sapphire blocks for in-situ visualization.

Figure. 6.18: UV fluorescence assisted, in-situ optical visualization of a shale(-glass) fracture within a pressure vessel under elevated temperature and stress/pressure.

Figure 6.19: Overall test system diagram.

Figure 6.20: Fluorescence optical images of fracture closure/proppant changes. From the initial state (left column) to the beginning of the time-lapse compaction at the highest effective stress (middle column) to the 2-week point of the experiment under sustained effective stress on the proppant and the fracture (right column). Circular black dots in the images are Viton discs which are used to determine the fracture aperture. Note that the initial image for 3Pb sample is darker—indicating a smaller fracture aperture—because the sample was accidentally loaded prematurely before the experiment was started.

Figure 6.21: Direct fracture aperture measurement using the deformation of a Viton dot on the fracture, determined from the optical images as shown in Figure 6.20. For comparison, measurements using LVDT (referenced at the maximum effective stress at 27 MPa) are also shown in broken lines. Because LVDT measurements include deformation of the entire test system (test cell wall, view window, sample-vessel interfaces), they overestimate the aperture changes. Clay-rich samples show more deformation than carbonate-rich samples. Acid treatment seemed to have little impact on this short-term deformation behavior (duration ~ 1 hour).

Figure 6.22: Long-term measurements of (additional) fracture closure (a) and flow resistance (b) from the start of the creep test (0 hour). The solid circles indicate untreated samples, and the open circles are acid-treated samples. Although the flow measurement is quite noisy, there is a general trend indicating gradual decreases in the fracture permeability. For heterogeneous, carbonate-rich samples, untreated 3Pa sample shows higher compaction than acid-treated 3Pb during the first ~10 hours of the test. Interestingly, carbonate-rich samples exhibited faster rates of compaction compared to clay-rich samples.

Figure 6.23: Photographs of the sample surfaces after the 2-week compaction experiment. The loose proppant and debris have been removed.

Figure 6.24: Comparison of Proppant Survivability Index (PSI) for all the samples. Although the overall values are similar (PSI=15-20%), notably, both carbonate-rich shales exhibited ~5% improvement in proppant crushing as a result of the acid treatment.

Figure 6.25: For the HFTS 3a and 3b samples, microscope images are used to identify three-types of mineral zones [blue shade=clay-rich zones, green shade=carbonate-rich zones, and yellow shade= pyrite (and carbonate)-rich zones].

Figure 6.26: Comparison of PSI (the ratio of proppant grains which survived crushing) in each zone of dominant mineral type, between untreated and acid-treated HFTS 3P samples. For the untreated sample, higher ductility of clay resulted in higher survival rate. In contrast, for the acid-treated sample, increase in the ductility due to porosity increases may have resulted in the survival rate, while the transfer of the force to the clay-rich zone caused more proppant crushing there.

Figure 6.27: False-colored microscope images of the HFTS 3Pb sample after the experiment, for locations with different shale-matrix mineralogy. Compared to the pyrite and carbonate-rich zones where acid treatment increased the matrix porosity, clay-rich areas showed smaller indentation depths. In the carbonate-rich section with large grains of carbonate minerals, acid treatment resulted in highly porous matrix which collapsed by indentation from proppant grains.

Figure 7.1: Schematic showing where mineral reactions may occur at the fracture-matrix interface in hydraulically-fractured shale reservoirs.

Figure 7.2: Schematic showing where fluid-shale chemical alteration is expected to affect flow in the reservoir.

Figure 7.3: Semi-quantitative XRD analysis of unreacted and reacted Wolfcamp shale from clay-rich and carbonate-rich horizons. All clays are listed as illite and all feldspars are listed as albite.

Figure 7.4: (a) Bulk XRF data for select elements for unreacted and reacted clay-rich and carbonate-rich samples; and (b) Calcium and Mg solution values for Timed reactors.

Figure 7.5: XRF mapping of Fe(II) and Fe(III) for reacted Wolfcamp shale. Significant Fe oxidation was seen in both sample types. Carbonate-rich samples had no detectable Fe in solution throughout the experimental time while clay-rich had measurable Fe in solution. Fe(III) bearing phases are primarily hematite, goethite, and magnetite, while clay-rich consisted of lower crystalline ferrihydrite, goethite, and magnetite.

Figure 7.6: Synchrotron XRF mapping of bromide tracer in Wolfcamp shale reacted with a simpler HFF formulation used in the Marcellus shale play. Little to no new skin precipitated in these samples.

Figure 7.7: (a) Electron microprobe images of Bromine for unreacted (Top), 3 hours reaction (middle), and 24 hours reaction (bottom) for clay-rich Wolfcamp shale. No additional Br was detected in the interior of the shale when a 1 M NaBr tracer was included in the HFF solution. The low Br skin on the left side of the core is thought to prevent the penetration of solution into the core and thus no additional Br would be detected. (b) Electron microprobe imaging of Mg, O, Si, and Al for 24-hour reacted clay-rich Wolfcamp clay. Imaged region is similar to that for Br in bottom panel of (a). Of particular note is that in edge of the core is clearly defined in all 4 images with Al not being present in the skin. This provides evidence that this new skin is a precipitation of new material on the surface and not infilling of the original shale matrix.

Figure 7.8: Schematic of diffusion cell experiment. A high concentration containing 0.5 M bromide (2) is located on the left, while a low concentration reservoir is maintained on the right. The shale sample is located in (1).

List of Tables

Table of Acronyms

DVC	Digital Volume Correlation
EDL	Electric Double Layer
GTI	Gas Technology Institute
HFTS	Hydraulic Fracturing Test Site
LBNL	Lawrence Berkeley National Laboratory
LLNL	Lawrence Livermore National Laboratory
MMP	Multiscale Modeling Project
MINC	Multiple Interactive Continua
NETL	National Energy Technology Laboratory
OGB	OilGasBrine
RVD	Relative vertical depth
SLAC	SLAC National Accelerator Laboratory (SLAC formerly Stanford Linear Accelerator Center)
SRV	Stimulated reservoir volume
TVD	True vertical depth
µCT	Micro Computed Tomography

Abstract

This project entitled “An Integrated Multiscale Modeling Framework for Unconventional Stimulation and Production” (short form: Multiscale Modeling Project, or MMP) is a modeling effort with the goal of improving the understanding of the processes that drive the mechanical and geochemical/hydrologic response to stimulation and oil/gas production from shale resources (Birkholzer et al., 2021). The ultimate objective is the development, application, and validation of a new framework for microscopic-to-reservoir-scale simulations of hydraulic fracturing and production, built upon a fusion of existing high-performance simulation capabilities available at four of DOE’s national labs, namely Lawrence Berkeley National Laboratory (LBNL), Lawrence Livermore National Laboratory (LLNL), National Energy Technology Laboratory (NETL), and SLAC National Accelerator Laboratory (SLAC). High-quality field data acquired from the HFTS, led by the Gas Technology Institute (GTI) and NETL at a site contributed by Laredo Petroleum in the Midland Basin, TX, are utilized for analysis, model development, and validation. The focus of the investigation encompasses a spatial scale extending from the micro- to reservoir scale.

1. Introduction

Production of oil and gas from unconventional reservoirs largely depends upon two main features operating at different scales: (1) the reservoir-scale stimulated fracture network providing permeability and transport from the formation to the production wells, and (2) the coupled multi-phase flow, mechanical and chemical processes affecting the migration of hydrocarbons from the low-permeability shale into the fracture network. Together they represent a complex coupled system operating over a broad range of length scales.

The revolution in unconventional resource recovery has been largely enabled by horizontal drilling and large-volume hydraulic stimulation; however, the impact of the operational choices to optimize the stimulated volume and maximize production (e.g., distance between adjacent wells, stages/well, perforations/stage, fluid rheology and pumping schedule) is not well understood today. Moreover, a steep decline in production within a relatively short time (compared to that for conventional reservoirs) following stimulation reflects, in part, the decreasing rate of hydrocarbon transport from the intact formation to the fractures. Processes leading to decrease in fracture aperture and loss of conductivity, such as proppant crushing, embedment and possible adverse chemical reactions within the reservoir, can also contribute to production decline. Decreasing efficiency is a primary motivation for drilling and stimulating additional wells, thus increasing the associated environmental footprint. Understanding how micro-scale processes (flow, geomechanics, geochemistry, etc.) control fluid flow in the fractures and the shale matrix is critical for predicting field-scale behavior, yet no modeling framework is available that incorporates these processes across all relevant scales. Such a framework would yield new insights into field-scale behavior and provide opportunities for model-driven scientific discovery to optimize hydrocarbon recovery from these complex shale systems.

The economics of resource exploitation and the minimization of associated environmental impacts will both benefit from increasing the efficiency of unconventional operations. Better predictive models for stimulation and production, capable of coupling various processes across multiple spatial and temporal scales, provide a path to achieving this goal. Historically, reservoir modeling tools have been limited to a subset of processes operating at a specific scale in order to reduce algorithmic complexity and increase computational performance. For example, fast-running models for hydraulic fracture design — such as ResFrac (McClure et al., 2020) typically focus on flow and mechanics at larger scales in order to provide a rapid solution. Reservoir production models — such as Eclipse (Kempka et al., 2013) or CMG-STARS/GEM (CMG, 2018) — solve for multiphase flow, with somewhat limited consideration of chemistry and mechanics, in order to achieve a timely solution. These approaches are suitable when engineering a system for which the upscaling of the fundamental processes is well understood;

however, as we have already discussed, shale reservoirs involve couplings of poorly understood processes across a wide range of scales.

Here we describe a new integrated modeling framework for microscopic to reservoir-scale simulations of hydraulic fracturing and production, capable of representing, connecting, and quantifying the major types of reservoir responses (flow, geomechanics, and geochemistry) that extend spatially from the pore structure of the reservoir rock to the volume of the reservoir, and temporally from the initiation and propagation of hydraulically-induced fractures to hydrocarbon production (**Figure 1**). At the reservoir-scale, the framework is built upon integration of two existing high-performance simulators for reservoir-scale behavior: the GEOS code for hydromechanical evolution during stimulation (Settgast et al., 2017) and the TOUGH+ code for multi-phase flow and chemical evolution during production (Moridis & Pruess, 2014). At the micro-scale, we deploy sophisticated imaging and testing methods (Voltolini and Ajo-Franklin, 2020; Hakala et al., 2017; Li et al., 2019), combined with reactive transport simulations (Tournassat & Steefel, 2019; Steefel & Tournassat, 2021) to develop a fundamental understanding of the mechanical and chemical processes within the propped fractures and across the fracture-rock interfaces. Constitutive upscaling relationships built upon this fundamental understanding are then incorporated in the reservoir-scale simulators. This multi-scale integration allows to directly evaluate the impact of cluster spacing, fluid injection rate, proppant volume, fluid chemistry and other operational choices on the effectiveness of a hydraulic fracturing treatment and the potential for long-term production, while ensuring that micro-scale property changes are adequately accounted for.

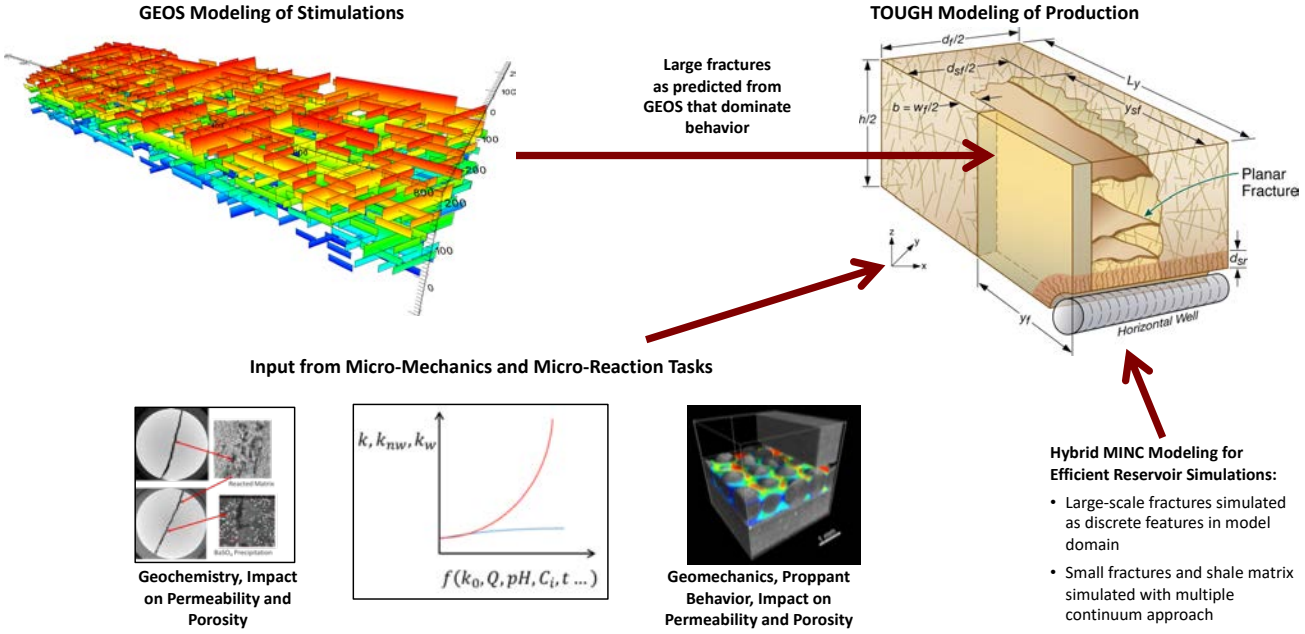

Figure 1: Schematic showing the framework for reservoir- scale stimulation and production simulations informed by micro-scale processes.

The new workflow starts with hydraulic fracturing simulations. In contrast to earlier hydraulic fracturing predictions which were often based on empirical relationships or simplified models (Adachi et al., 2017; Lecampion et al., 2018), the GEOS simulator used in this study is based on a rigorous numerical treatment of the hydraulic fracturing mechanics and deploys a fully coupled finite element/finite volume approach for fractures with arbitrary three-dimensional geometries (Settgast et al., 2017). Using GEOS, fracture growth and the associated seismicity are simulated in space and time and the resulting fracture geometries are handed over to the next step in the workflow. Simulation of hydrocarbon production is done with the TOUGH+ family of

simulators for multi-phase flow of water, gas, and oil phases in fractured and unfractured rock (Moridis & Pruess, 2014). Embedded in a high-performance computational framework, TOUGH+ has the option of discrete representation of major fractures in addition to the description of other fractures (induced or natural) embedded in the rock matrix as a multi-continuum domain using a double-porosity, dual permeability or Multiple Interactive Continua (MINC) approach. This approach (1) allows for explicit representation of all relevant hydraulic fractures provided by GEOS, while (2) capturing the detailed fracture-matrix flow and transport processes without the need to discretize the largely unknown individual fractures within the matrix blocks. While this modeling workflow is applied here to unconventional oil and gas production, the GEOS-TOUGH+ simulation capabilities have broad applicability across multiple other subsurface applications (which are aligned with the current administrations priorities), such as subsurface energy storage, geologic carbon sequestration, or geothermal energy production.

As mentioned above, the GEOS-TOUGH+ simulations incorporate the transient property changes induced by micro-scale mechanical and chemical processes that occur in individual fractures and near the fracture-shale interfaces. Several recent studies involving a variety of sophisticated imaging and testing methods have improved our fundamental understanding of such processes and have provided a basis for developing constitutive upscaling relationships that can be used in reservoir models. These include, for example, the permeability evolution of propped fractures in different types of shales over a range of stress conditions (Voltolini et al., 2017) or the fracture aperture changes and proppant embedment in shales exposed to different types of fracturing fluids (Vankeuren et al., 2017; Moore et al., 2018). Researchers also studied dissolution and precipitation reactions across the fracture-matrix interface (Hakala et al., 2017; Marcon et al., 2017; Harrison et al., 2017; Jew et al., 2017a, Jew et al., 2017b; Jew et al., 2018; Li et al., 2018) and demonstrated that properties of the shale matrix and fractures can be affected by mineral precipitation arising from the injected fluids (fracture to rock) and chemical alterations to the shale itself (matrix to fracture). In ultra-low permeability rocks, especially those with > 20 wt.% clay, geochemical reactions can reduce overall permeability by more than 40% (Allali et al., 2018).

The integrated modeling framework was tested using high-quality data and core samples from the Hydraulic Fracturing Field Test (HFTS), a field experiment with extensive monitoring of the hydraulic fracturing process and the associated shale oil and gas production in the Permian Basin (Ciezobka et al., 2018; Weijermars et al., 2020; Salahshoor et al., 2020; Courtier et al., 2017). In addition to a full set of geophysical and other observations (such as microseismic signals, tilt, downhole pressure variations, tracer transport, and production data) which can be used to test the GEOS-TOUGH+ reservoir-scale simulations, the HFTS project obtained core samples from a science observation well that was drilled through the stimulated volume after hydraulic fracturing. This core provided a rare opportunity to observe and evaluate the geometry and properties of hydraulic fractures, and to compare their characteristics with pre-existing natural fractures. We employed measurements using HFTS core samples to gain insight into the transient property changes induced by micro-scale mechanical and chemical processes that occur in individual fractures and in the vicinity of the fracture-shale interfaces.

This report describes the new modeling framework including the coupling scheme between GEOS and TOUGH+ (Section 2), followed by a short description of the HFTS Project (Section 3). The report then discusses the numerical and experimental application to HFTS. At the reservoir-scale, the project team applied the advanced fracture simulation tool GEOS to predict the fracture network evolution upon stimulation and the influence of geologic and engineering parameters (Section 4). These simulations provide, in an automated workflow, the fracture geometries and properties for reservoir-scale production simulations using TOUGH+ (Section 5). The reservoir-scale models are informed by micro-scale studies of fracture proppant mechanics (Section 6) and chemical reactions (Section 7). The laboratory and simulation studies investigate (1) how these micro-scale processes impact both the permeability within fractures and at the fracture-shale interface and (2) how these studies can provide upscaled flow and transport parameters for the reservoir-scale stimulation and production modeling.

2. High-Performance Modeling Framework with GEOS and TOUGH+

This project brought together two best-of-breed HPC simulators for geomechanics (GEOS) and multiphase, multicomponent flow (TOUGH+). The following sections provide a brief overview of these codes and the approach taken to couple them into a unified simulation framework.

2.1 Geomechanical Simulator GEOS

GEOS was developed for high-performance simulations of complex subsurface processes involving fluid flow, mechanics and chemistry. Particular emphasis is placed on the algorithmic details that are necessary to adapt the fully coupled finite element/finite volume approach to model large-scale problems on massively parallel high-performance computing platforms. Applications of GEOS have included prediction of the performance of hydraulic fracturing strategies in shale formations (Settgast et al., 2017) with forward modeling of geophysical variables for validation against field data (such as microseismic and distributed acoustic sensing, Sherman et al., (2019a; 2019b). GEOS accommodates detailed descriptions of 3D features such as stress and modulus variability, along with a discrete, mechanically-coupled representation of numerous preexisting natural fractures. More recent development has extended GEOS to include coupled chemical processes (Iyer et al., 2018), and the prediction of hydrocarbon production in fractured, unconventional reservoirs (Hao et al, 2016a; 2016b; 2017) although in this project we focused upon leveraging its ability to capture coupled flow and mechanics during stimulation.

2.2 Multi-Phase, Multi-Component Simulator TOUGH+

The TOUGH+ reservoir simulator (Moridis & Pruess, 2014) accounts for multiphase fluid flow under pressure, viscous, and gravity forces according to Darcy's law. It models all processes involved in the non-isothermal, multi-component, three-phase flow of fluids and heat through porous and/or fractured geologic media. The OilGasBrine (OGB) module for TOUGH+ simulates conventional and/or unconventional (fractured tight- and shale-oil) reservoirs and accounts for heat and up to 13 mass components (H_2O, oil, and a gas phase of up to 11 components) partitioned between organic (oil), gas, aqueous, and (if necessary) solid hydrate phases. TOUGH+OGB can describe all phase combinations of a H_2O, oil, and non-condensing-gas-mixture system. It has a fully implicit, Newton-Raphson-based formulation that solves the Jacobian resulting from the mass and energy balance of all components involved in the system. The Jacobian-based approach, with strict mass and heat balance error criteria, can handle the phase changes, state transitions, strong nonlinearities, and steep solution surfaces found in unconventional reservoir simulations. The capabilities of TOUGH+OGB have been included in the pTOUGH+ framework (Zhang et al., 2008) to allow large-scale parallel processing for simulations of large reservoirs with highly refined meshes.

2.3 Coupling Scheme Between GEOS and TOUGH+

The GEOS-TOUGH+ coupled framework is illustrated in Birkholzer et al. (2021), and described again here. The coupling procedure begins with building a structured base mesh for TOUGH+, in which a hydraulic fracture is explicitly represented as one layer of grid cells with locally refined grid resolutions (**Figure 2.1**). This layer of fracture cells initially has uniform properties (e.g., fracture permeability k_f, grid resolution Δy). The horizontal well is perpendicular to the fracture plane. The SRV surrounding the primary fracture is implemented by a dual-porosity, dual-permeability model that represents stimulated secondary fractures and the neighboring unfractured matrix with the need to explicitly mesh each secondary or background fracture. The rest of the domain is the single-porosity matrix with permeability (k_m) on the nano-Darcy scale.

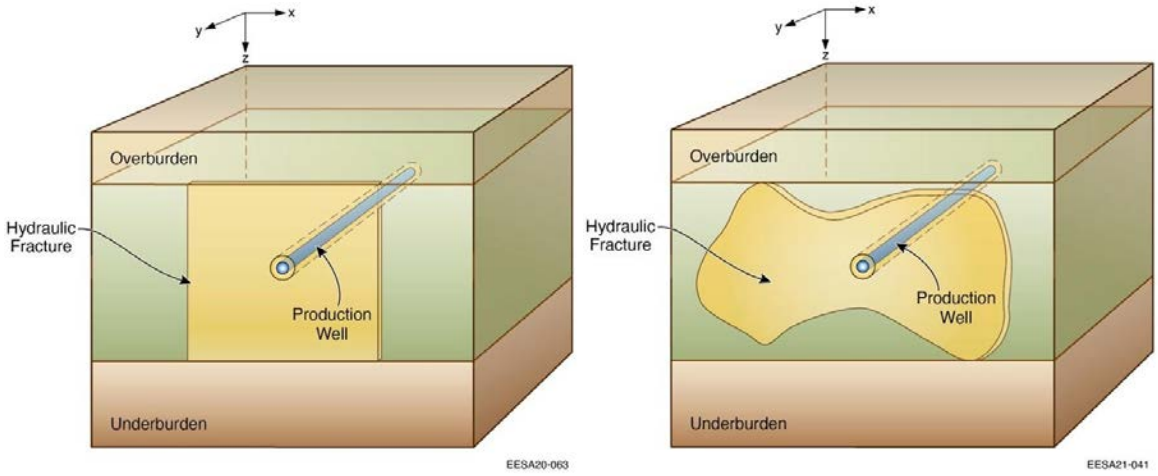

Figure 2.1: (a) Half of the stencil used in this study. It contains one primary hydraulic fracture, the stimulated volume zone(s), the shale matrix and the production well. The overburden and the under burden are excluded from the computational domain. (b) A similar stencil with a homogeneous rectangular hydraulic fracture.

GEOS generates hydraulic fractures with spatially heterogeneous apertures at the time of shut-in. We refer to these as the "raw" apertures to distinguish them from the subsequent apertures we predict under subsequent closure stress. These raw apertures are converted into effective propped apertures (b_{prop}) and are mapped to the corresponding fracture cells in the base mesh. The "propped aperture" is calculated following Eq. 2.1 (Huang et al, 2018), where b and φ are the raw aperture and the proppant volume fraction modeled by GEOS, φ_{max} is the maximum proppant volume fraction in the hydraulic fracture, b_{closed} is an empirical parameter representing the closure aperture of an unpropped fracture. The use of an effective propped aperture considers the combined effects of post-stimulation fracture closure and the effects of heterogeneous proppant transport. This approach provides a more accurate estimate of the true post-stimulation aperture distribution than the raw GEOS-generated aperture.

$$b_{prop} = max\left(\frac{\varphi b}{\varphi_{max}}, b_{closed}\right) \qquad \text{(Equation: 2.1)}$$

To resolve the heterogeneous aperture field within a TOUGH+ mesh, the resolutions of the fracture cells in the base mesh are adjusted such that $\Delta y(x,z) = b_{prop}(x,z)$. The porosity and the connection areas of the fracture cells are adjusted accordingly. These post-adjustments of the TOUGH+ mesh reflect heterogeneity in the geometrical properties of the fracture, which exert a strong influence on the modeled production (Liu et al., 2019).

The permeability of a fracture cell is calculated with the modified cubic law (Eq. 2.2). It has been observed that multiple parallel, closely spaced hydraulic fractures are generated from single perforation clusters (e.g. Gale et al., 2018; Fu et al., 2021). The upscaling approach by Fu et al. (2020) is applied to form exactly one upscaled fracture for each cluster. The parameter n is used to adjust permeability, and is selected to guarantee that the flow rate is not overestimated during upscaling. Its physical meaning is the number of individual fractures in a fracture swarm. The present study uses $n = 8$, which is consistent with observations from the HFTS and is the value utilized by the GEOS stimulation models.

$$k_f = \frac{b_{prop}^2}{12n^2} \qquad \text{(Equation: 2.2)}$$

An example of the hydraulic fractures modeled by GEOS is shown in **Figure 2.2**. It consists of five parallel fracture clusters, which are spaced 16 m apart and use the swarm upscaling model with $n = 8$. As the fracture

propagates, it compresses the adjacent rock and creates a stress shadow that affects other nearby fractures (Duan et al., 2020; Wan et al., 2020) and leads to regions of large and small apertures alternating between adjacent fractures, or can cause fractures to avoid a region entirely. This behavior is often reinforced when proppant is injected into the system, leading to regions of large and small proppant volume fraction.

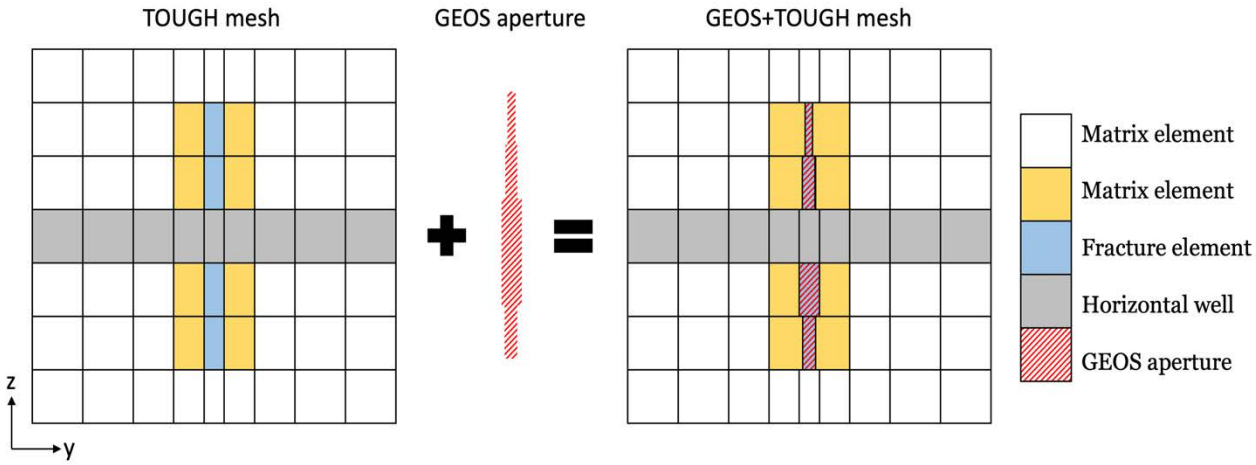

Figure 2.2: Coupling scheme between GEOS and TOUGH+ that shows the mesh adjustments with respect to GEOS aperture. Only one layer is shown here for illustration purposes.

The stress-shadow effect poses challenges to the simulation of production when it creates localized zones of reduced aperture. These aperture bottlenecks act as flow barriers, creating isolated zones with minimal contribution to production away from the horizontal well. The TOUGH+ numerical solvers are challenged (and often unable to converge) when the inflow into the isolated zone is much greater than the outflow across the flow barrier. To avoid non-convergence caused by the aperture bottlenecks and the resulting isolated zones, we note that outflow from the isolated zone is determined by the bottleneck aperture, allowing a reduction of the aperture inside the isolated zone to improve convergence without affecting the net production rate of the fracture. This is achieved by replacing b_{prop} with a uniform modified aperture, b_{mod}, inside the isolated zone. The modified aperture is defined as:

$$b_{mod} = \left(\frac{\sum_{i=1}^{N} (b_{bot})_i^3}{N}\right)^{\frac{1}{3}} \left(\frac{\partial p}{\partial x}\right)_{bot} \left(\frac{\partial p}{\partial x}\right)_{iso}^{-1} \qquad \text{(Equation: 2.3)}$$

A detailed discussion of how this modified aperture was derived and validated can be found in Li et al. (2021). This method is a significant contribution to the modeling of flow in fractured reservoirs, allowing necessary heterogeneity in the representation of the fractures in a computationally efficient manner.

3. Hydraulic Fracturing Field Test Site in the Permian Basin, USA

The HFTS project, fielded within the Wolfcamp Formation in the Permian Basin, provides an excellent opportunity to further develop our understanding of the hydromechanical response to hydraulic stimulation and associated fluid transport in shale lithologies. Supported by the U.S. Department of Energy and a consortium of industry sponsors, the experiment was designed to elucidate the intra- and inter-well stress interactions within a single horizon and also among vertically separated wells in different lithologic units, and their influence on hydrocarbon production (Ciezobka et al., 2018; Weijermars et al., 2020; Salahshoor et al., 2020; Courtier et al., 2017). The project involved the drilling of 11 horizontal wells within the Upper and Middle Wolfcamp Formation in the Midland basin of West Texas, at a site hosted by Laredo Petroleum, Inc. The wells were drilled approximately 200 m (660 feet) apart laterally and 137 m (450 feet) apart diagonally in what is often referred to as a "wine-rack" pattern (**Figure 3.1**, Stegent et al., 2019). Substantial data from the HFTS has been published and well-documented in special sessions of the URTeC conference (see **Figure 3.2**).

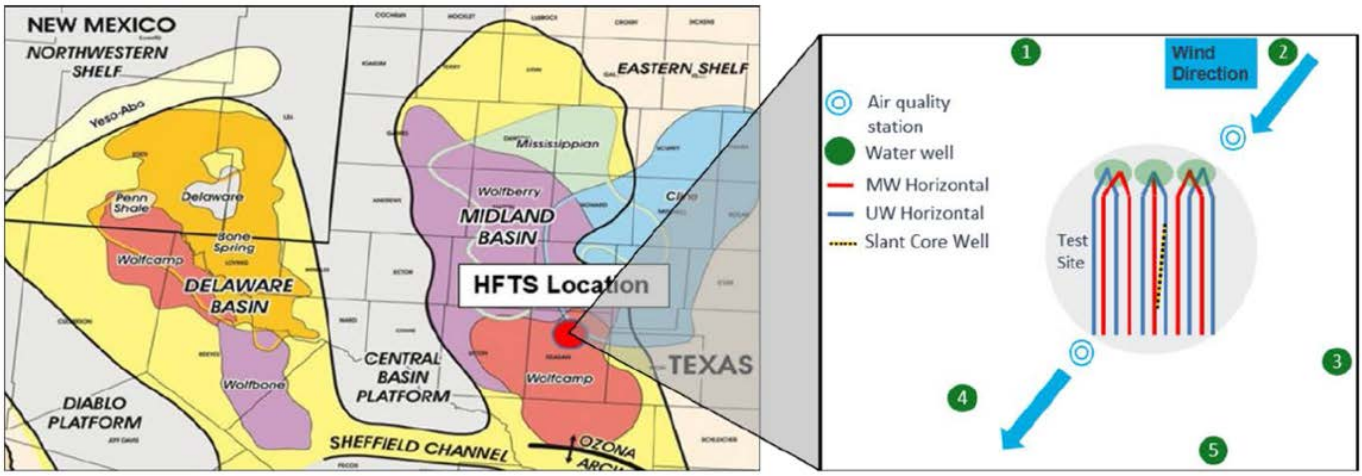

Figure 3.1: Left—Map showing the location of the HFTS experiment in the Permian Basin. Right—Details of the HFTS (from Salahshoor et al., 2018).

The HFTS project featured a very comprehensive characterization and monitoring effort before, during, and after the completion of about 400+ fracture stages in 2015. As mentioned above, in addition to a full set of geophysical measurements and various other observations of reservoir behavior during stimulation and production, the project featured a unique post-stimulation core well drilled through the stimulated volume. The obtained cores provide a rare opportunity for (1) direct characterization of fracture and proppant distribution, (2) determination of the potential modification of the rock matrix adjacent to hydraulic fractures, and (3) for state-of-the art micro-scale characterization and testing (**Figure 3.3**). As such, HFTS provides a unique opportunity for the testing of a modeling framework that involves reservoir-scale modeling while incorporating impact from micro-scale processes occurring in individual fractures and fracture/shale interfaces.

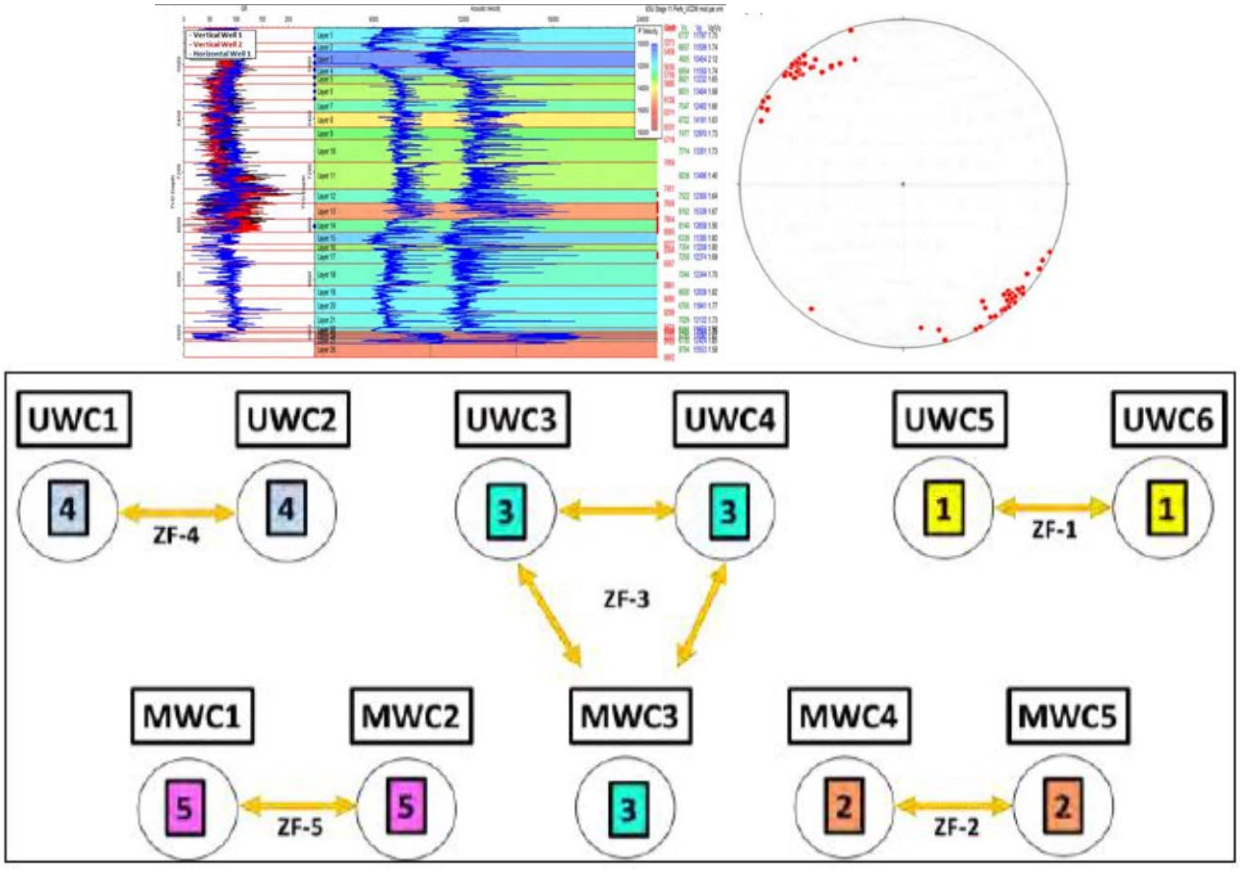

Figure 3.2: Examples of HFTS-specific data obtained from the proceedings of HFTS special sessions at URTeC in 2018. Top left: velocity model. Top right: natural fracture orientations. Bottom: Well stimulation sequence.

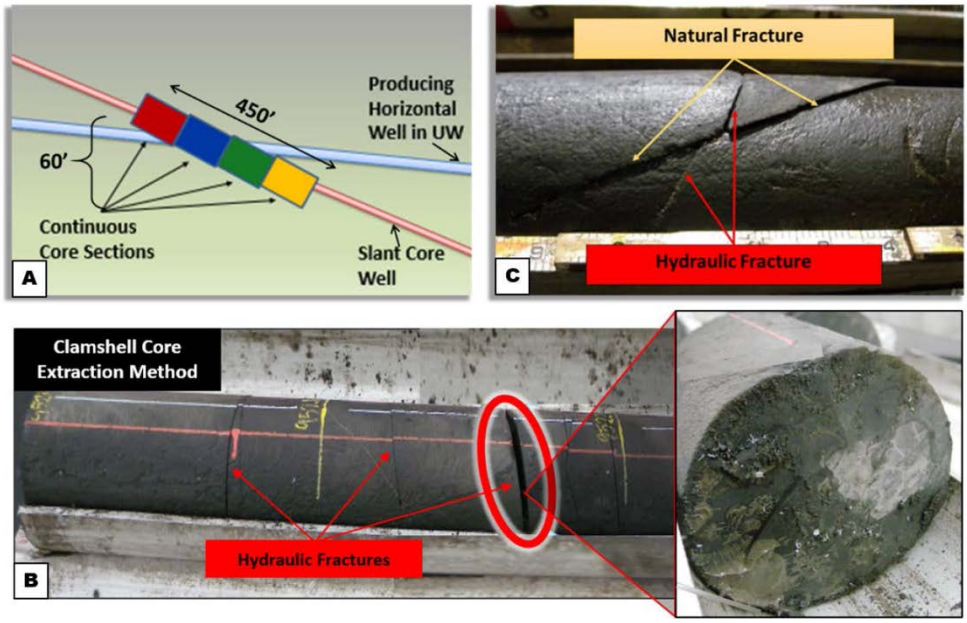

Figure 3.3: (A) Depiction of the continuous core sections collected adjacent to the stimulated producing Upper Wolfcamp well. (B) Example of a whole core interval. Hydraulic fracture shown in right panel. (C) Examples of hydraulic fractures cutting a natural fracture captured in the core (from Ciezobka et al., 2018).

Of particular importance for understanding height containment mechanisms, we developed a refined stress model through digitization of logs provided as part of the HFTS data set. **Figure 3.4** compares this stress model published stress data. We observe similar trends in stress, but the HFTS data provides significantly more complex structure in the stress which must be captured because it influences height growth in the modelling.

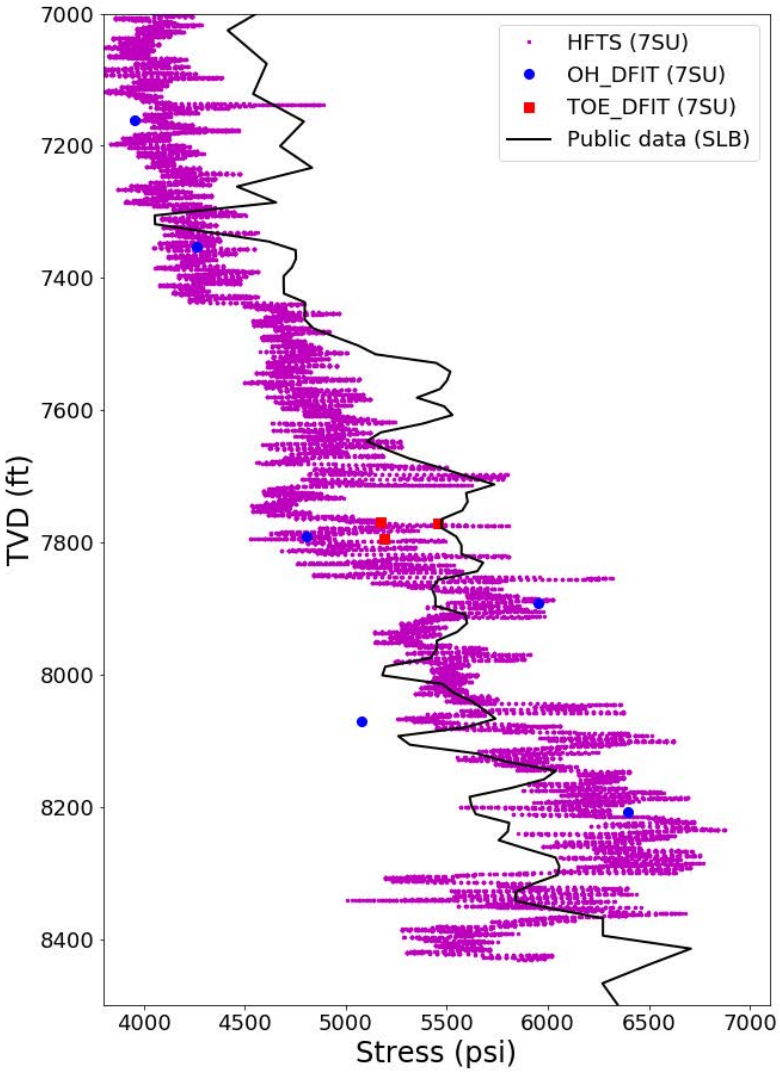

Figure 3.4: LLNL stress model obtained via digitization of the 7SU logs provided by the HFTS project. Another stress model, based upon public sources for a neighboring area, is shown for comparison.

We developed a complex 3D geologic model that conforms to the known location of key interfaces in the surface (see **Figure 3.5**) to allow us to explore the impact of 3D heterogeneity in the HFTS reservoir. This 3D model was incorporated into our analyses regarding fracture heigh growth throughout the reservoir. The effect of this 3D heterogeneity was found to introduce predictable trends in fracture growth and our analysis suggests that these factors should be considered when designing stimulation plans (see Sections 4.4).

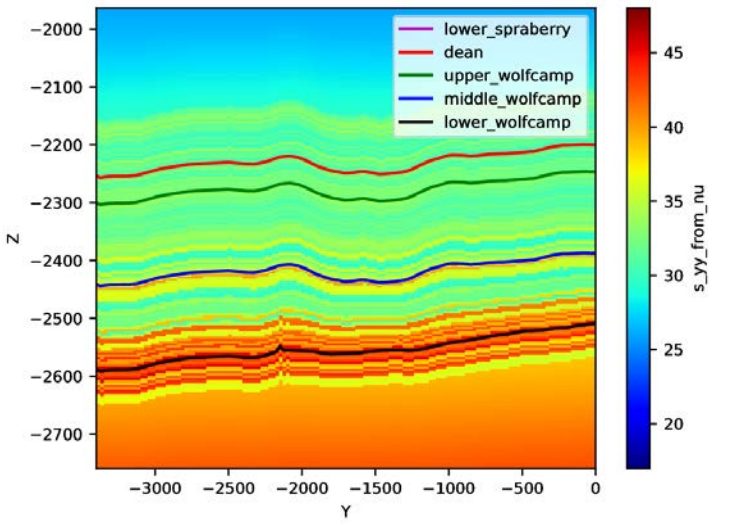

Figure 3.5: Cross-section along through the center of the 3D model showing the estimated minimum horizontal stress and key layer locations.

Microseismic data proved to be one of the more important validation data sources. We built a unified model including well trajectories, layer tops, and the microseismic to assist with interpretation of the microseismic and potential use for validation (**See Figure 3.6**)

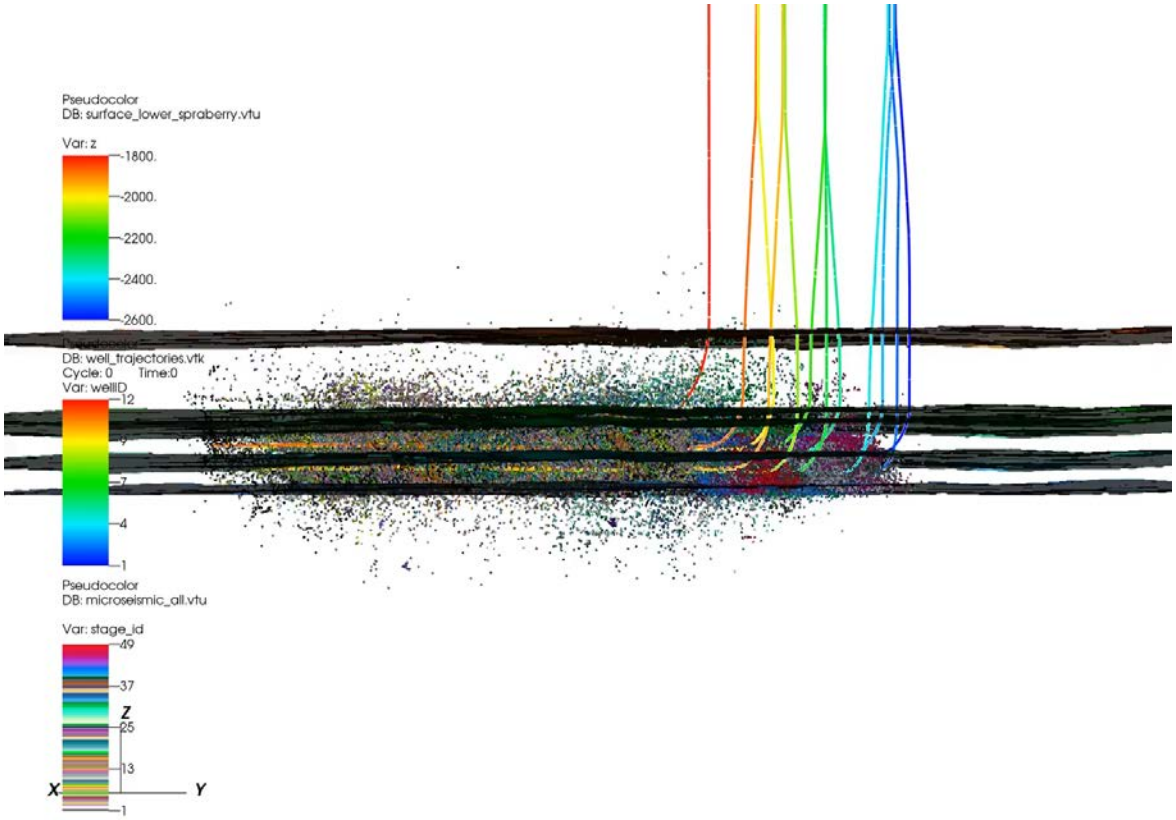

Figure 3.6: Well trajectories, layer boundaries, and microseismic data were integrated into a single model to assist with analysis and interpretation of microseismic data.

We also studied the distributed temperature sensing data (DTS) and derived a number of conclusions from this investigation. In particular, the DTS indicates strong peaks associated with cluster locations (as expected) that can quantify the effectiveness of the individual clusters along the length of the well (see **Figure 3.7**).

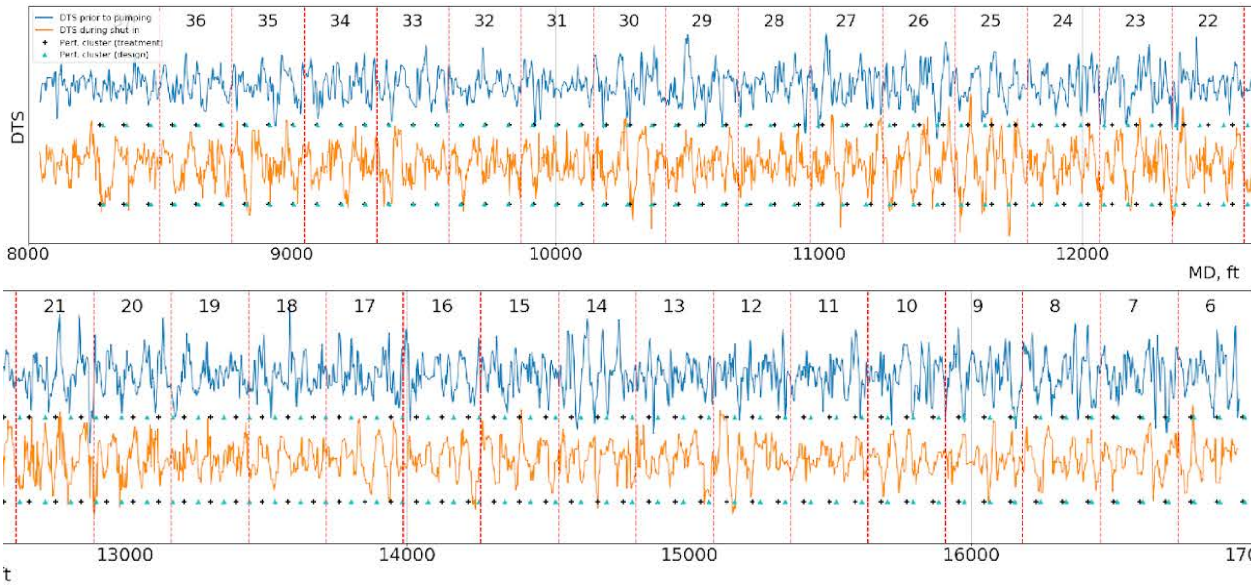

Figure 3.7: HFTS Distributed Temperature Sensing (DTS) data.

A distinguishing feature of the HFTS data set is the core acquired via drill-back through the stimulated zone. We focused upon obtaining as much insight as possible from this source, including both statistical analyses and laboriously looking through all core imagery. This exercise was particularly important in order to establish any uncertainties in the interpretations of the fractures and proppant observed on the core (see **Figure 3.8**).

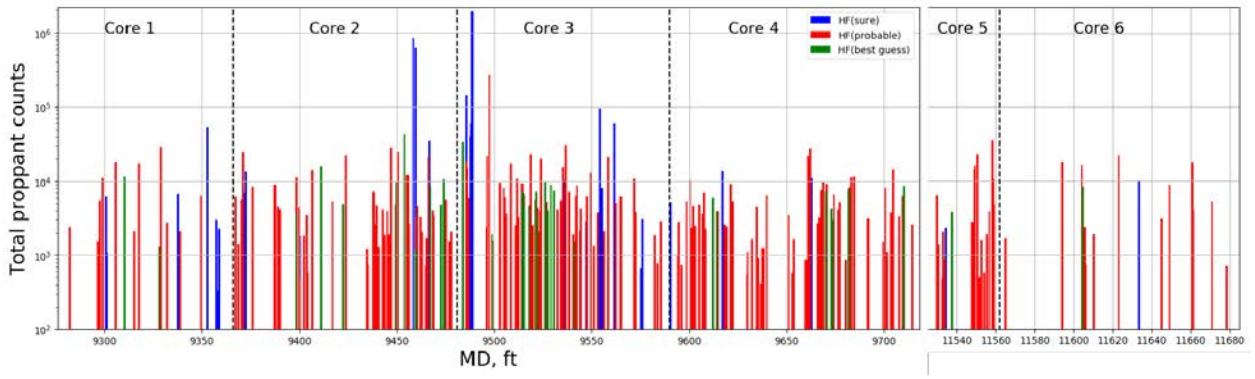

Figure 3.8: LLNL reanalysis of the proppant observed on the core, relating its presence to the hydraulic fracture confidence level.

4. Reservoir-scale Hydraulic Fracturing Modeling

Reservoir-scale hydraulic fracturing modeling, mainly performed by MMP's LLNL team, has three main objectives: (1) gaining insights into key observations from the HFTS experiment, particularly the high hydraulic fracture density unexpected by conventional wisdoms, (2) developing practical methods to model hydraulic fracturing that incorporate HFTS learnings, and (3) exploring methods that can further optimize resource recovery.

Note that the observed high-density hydraulic fractures have been customarily called "fracture swarms". Literally the word "swarm" refers to a collective behavior of entities to "aggregate together". Applied to fracturing patterns, it implies that fractures tend to propagate in groups, maintaining a dense spacing. Though we do not necessarily agree with the apparent implications of this term, we generally adopt this term in this report for the convenience of narrative. The high hydraulic fracture density in recovered cores has been corroborated by other similar field experiments involving coring back. Those experiments include ConocoPhillips's experiment in the Eagle Ford (Raterman et al., 2018; 2019) and the Hydraulic Fracture Test Site 2 (HFTS-2) in the Permian Delaware Basin, both in Texas. Each of the three projects involved coring through the "stimulated volume" along a trajectory largely parallel to the horizontal wells and orthogonal to the expected the hydraulic fracturing planes. The Eagle Ford experiment saw a total of 2,466 hydraulic fractures along core wells (Well S3 and its three sidetracks) with a total length of 6444 ft; the HFTS project's slant core well saw 361 hydraulic fractures along 600 ft of cores; the HFTS-2 project's 948 ft of cores revealed 500 hydraulic fractures. Such closely spaced hydraulic fractures with an average spacing of 1 to 2 ft were unanticipated. This observation also poses a great challenge to hydraulic fracturing modeling because existing codes, including GEOS, had been devised based on the underlying assumption of much lower hydraulic fracture density.

In the following four sections, we document how our set objectives were met. We first recognize that before a concrete understanding of the underlying mechanism for fracture swarming can be established, we need a method to at least phenomenologically represent the "effects" of high-density fractures. An up-scaling method that represents a group of closely spaced fractures with one equivalent fracture is first presented in Section 4.1. Using this method and HFTS data, we studied how one can control hydraulic fracture growth through precise vertical placement of lateral wells, as summarized in Section 4.2. A statistical analysis in Section 4.3 reveals whether it is possible that the observed "swarming" pattern is the appearance of a random Poisson process. We then present our investigation of the swarming mechanism in Section 4.4 through a critical analysis of four hypothetical mechanisms.

4.1 An Upscaling Method to Represent Fracture Swarms

Recognizing that fracture swarms may be the key mechanism required to explain the geophysical observations at HFTS, we created a new and highly efficient method to model fracture swarms in GEOS. A detailed description of the approach was published in the journal article Fu et al. (2021).

Given the observed spacing of fractures present within a swarm (often less than 1 m), it would not be feasible to regularly model a fracture swarm over the large spatial and time scales expected for a swarm (hours of pumping, and extents reaching several hundred meters). Instead, we developed an approach to treat fractures as upscaled swarms by modifying the viscosity of the fracturing fluid and toughness of the surrounding rock. Following the arguments we published in Fu et al. (2021), for a swarm consisting of N tightly spaced, parallel hydraulic fractures that take equal amounts of fluid, the effective viscosity, μ^*, will be:

$$\mu^* = \mu N^2 \qquad \text{(Equation: 3.1)}$$

and the effective toughness, *K**, will be:

$$K^* = K\sqrt{N}\,. \qquad \text{(Equation: 3.2)}$$

To validate the model assumptions, we created a model that directly simulates the dynamics of a fracture swarm using a highly refined numerical mesh, and we compared the results to an equivalent model using the new upscaling approach (see **Figure 4.1**). The extents of the fracture swarm match very well over time, and the aperture of the upscaled model matches the sum of apertures across the swarm, especially outside of some minor variations in the fracture tip region. In addition, these models produce a very similar stress field, with tensile stress dominating near the tip(s) and compressive stress dominating near along the sides.

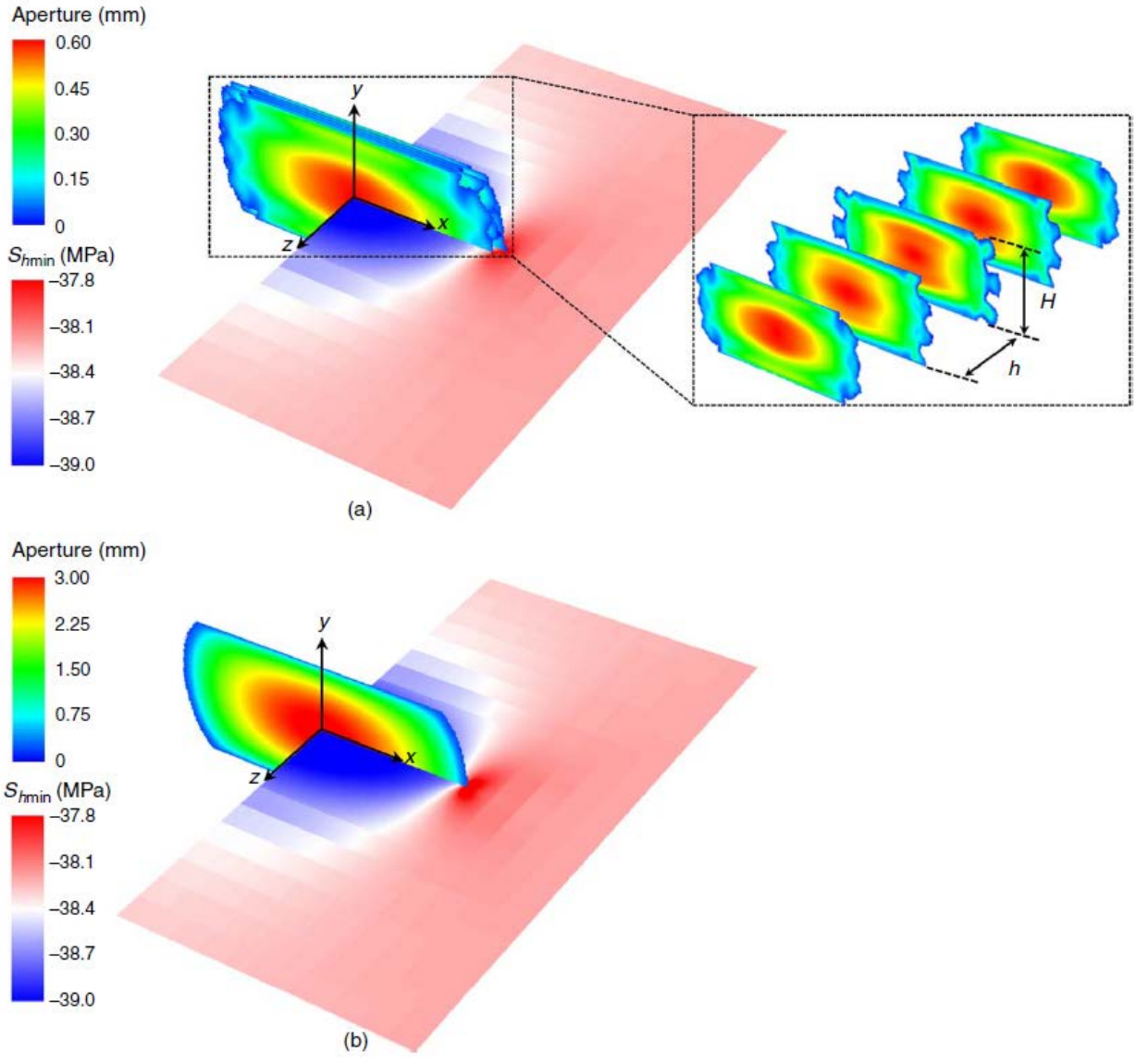

Figure 4.1: Comparison between the GEOS simulations that (a) directly model the hydraulic fracture swarm, and (b) models the fracture swarm using the upscaling approach. The extents of the fractures and the sum of the fracture apertures are an excellent match, especially outside of the tip-region.

Further testing of the upscaling model indicated that the spacing between fractures in the swarm does not necessarily need to be even, and that as long as it is relatively small compared to the fracture extents, the approach holds. The model also holds under conditions where the swarm encounters stress shadowing from nearby fractures (or swarms).

After developing the upscaling approach, we used it to model hydraulic fracture propagation at the HFTS. Unlike before with the conventional monolithic fracture model, we found that it was straightforward to calibrate individual hydraulic fracturing stages against the geophysical observables assuming that there were eight fractures per swarm (N=8). From this point, our analysis split in two directions: investigating the mechanisms surrounding the fracture swarming phenomenon, and using the upscaled model to evaluate the behavior of fractures throughout the HFTS reservoir.

4.2 Controlling Hydraulic Fracture Growth Through Precise Vertical Placement of Lateral Wells

Controlling the geometry of hydraulic fractures is a significant challenge for the design of reservoirs, due to the inherent variability of in-situ properties, stress, and wells. In our analysis of the microseismic data recorded in the down-hole array in the HFTS reservoir, we identified a sequence of stages with high-quality recordings (e.g., appear to have complete catalogs, minimal recording bias, and high semblance with nearby stages). Using these data, we estimated the extents of the induced fractures over time, being careful to reject any outliers that could be associated with other stages or measurement error. In our analysis, we found it useful to look at the "relative vertical depth" (RVD), which we defined as the vertical distance between a point of interest and the upper surface of the relevant rock layer, rather than the more common "true vertical depth" (TVD).

It is challenging to estimate the full-3D stress field in a reservoir with the limited measurements available. In our work, we developed a new method to use a combination of conventional stress analyses, seismic survey information, and mechanical modeling to produce such a model. To begin, we followed the approach of Kohli & Zoback (2021) to construct a 1D model of Shmin as a function of RVD by analyzing available ISIP, DFIT, and wireline log data. This procedure involves using the highest quality DFIT data to constrain the magnitude of the stress in key locations, using calibrated ISIP measurements to estimate stress in regions adjacent to wells, and using log-data to extrapolate the stress field into other regions of the reservoir. To build a 3D model of the reservoir, we take the available 1D data along the key wells, and map them into the reservoir using the estimated locations of the key geologic surfaces. Due to the 3D structure, this new model will be out of static equilibrium. To address this, we constructed a large-scale, purely mechanical model in GEOS using the initial 3D model, and then solve for equilibrium conditions under the influence of gravity. The stress estimates from this final model are shown in **Figure 4.2**.

Using this 3D model and the previously discussed fracture swarm upscaling method, we simulated the hydraulic fracturing processes using as as-pumped fluid and proppant schedules for the sequence of stages identified as having excellent microseismic data. The fracture heights of the simulated stages generally agree with the trend inferred from the microseismic data. We found that for this sequence, the height of simulated fractures changes from ~300 m to ~100 m, while the fracture height based on microseismic data changes from ~250 m to ~150 m, as the RVD increases (deeper within the layer) from Stage 25 to Stage 37. A key feature of the microseismic and modeling results is the transition region around Stage 28, where the overall shape of the generated fractures changes dramatically (see **Figure 4.3**). This transition likely occurs due to interaction with key stress barriers in the reservoir, which fractures tend to break through when generated at a critical value of RVD. This approach highlights the power of using a high-quality, physics-based simulator to identify these potential trends, which can in turn be used to make engineering decisions. In practice, such 3D analysis could readily be used ahead of time to tailor individual stage pumping schedules to achieve the desired reservoir contact.

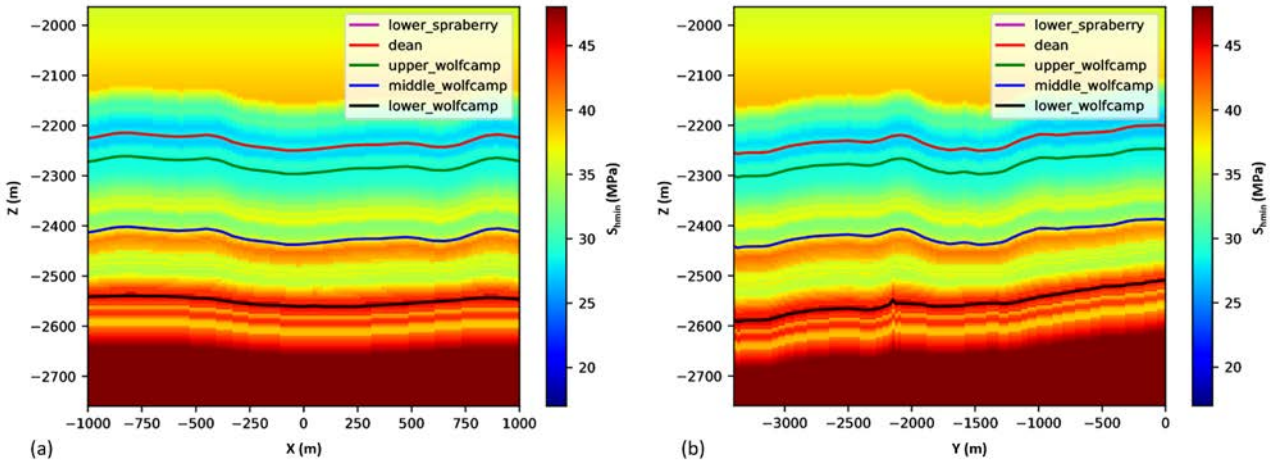

Figure 4.2: Slices through the 3D stress model for the HFTS reservoir.

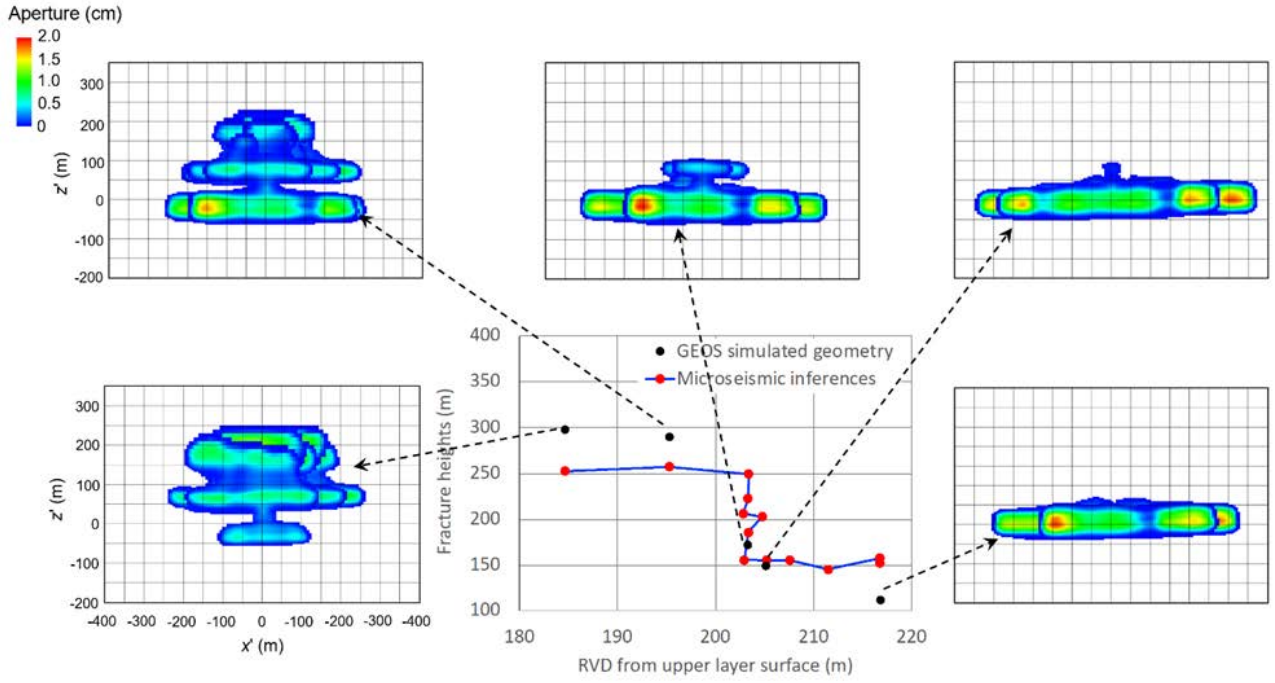

Figure 4.3: Simulated hydraulic fracture geometries at different RVD and comparison with the corresponding fracture height estimated from microseismic clouds.

4.3 Statistical Analysis of the "Swarming" Patterns

When fracture patterns from the Eagle Ford experiment were first published in Raterman et al. (2018), the authors noted "the hydraulic fractures form swarms in which many fractures are spaced a few inches apart and are separated by lengths of core with several feet between fractures". Similar fracture spacing patterns were also observed in HFTS cores, though the HFTS team did not use the term "swarm" or "swarming" in characterizing the observed patterns. In presenting the fracture spacing pattern observed in HFTS-2 cores, the same authors used terms such as "four-fracture swarm" and "five-fracture swarm".

The word “swarm” refers to a collective behavior of entities to “aggregate together”. Applied to fracturing patterns, it implies that fractures tend to propagate in groups, maintaining a dense spacing. This pattern, if established, has a profound implication for understanding the mechanism underlying the high fracture density. In other words, a hypothetical mechanism needs to explain why fracture tend to grow while maintaining small inter-fracture distances.

In this section, we perform a rigorous statistical analysis to determine whether the fractures indeed tend to propagate in a “swarming fashion”. The “null hypothesis” (H_0) is that the hydraulic fractures propagate in a largely independent way. If this is true, fracture density, in terms of fracture counts per unit length along the core, should follow a Poisson distribution.

We focus on Cores 1 to 4 in the Upper Wolfcamp formation, which form a contiguous, 440 ft-long segment. 310 out of the 361 hydraulic fractures are in this segment. **Figure 4.4(c)** shows that the pattern of fracture spacing is not consistent throughout the lengths of the cores. Because the TVD of this core segment covers a range of 60 ft, the varying spacing pattern could reflect different fracture growth patterns in various sub-layers. We therefore need to perform the analyses on subsegments, or analysis windows, each with a relatively cohesive fracture spacing patter. The subsegments are manually determined based on visual inspection. In selecting the analysis windows, we consider two scenarios:

- Subsegments within each of which spacing among hydraulic fractures exhibits a cohesive pattern; and
- Subsegments within each of which spacing among hydraulic fractures and “reactivated” natural fractures, when pooled together, exhibits a cohesive pattern.

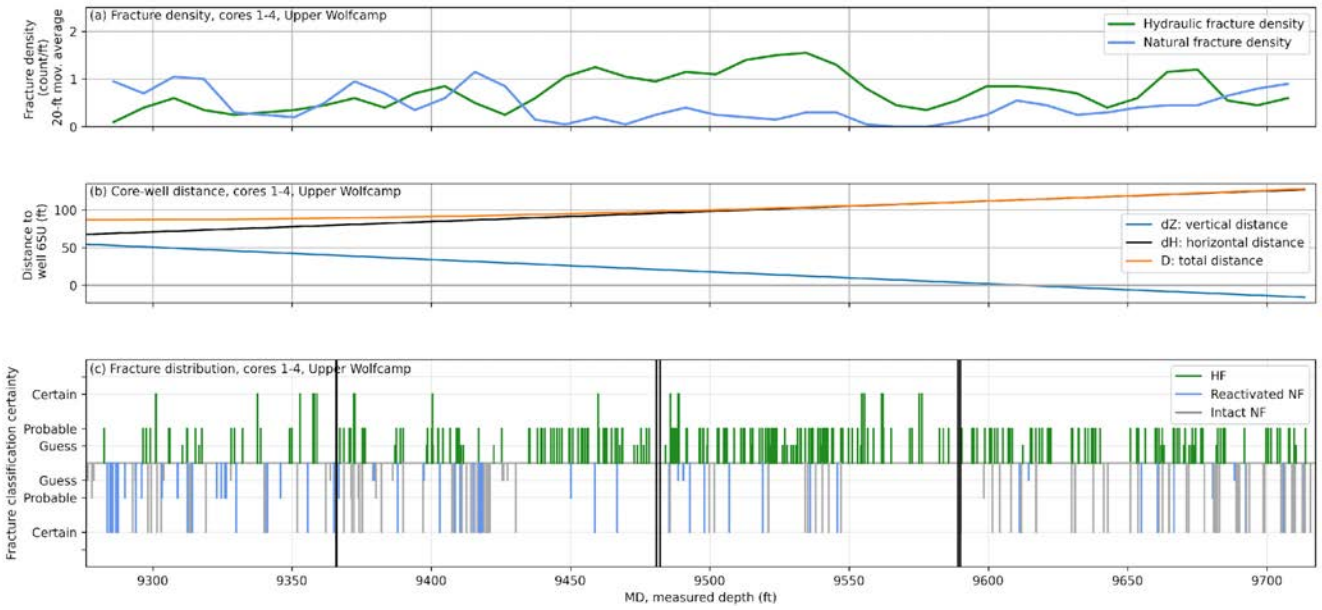

Figure 4.4: Visualizations of hydraulic fracture and natural fracture distributions along the four cores retrieved by the HFTS experiment in the upper Wolfcamp formation. (a) Hydraulic fracture density and natural fracture density calculated on 20-ft moving-average intervals. (b) Distances from cores 1-4 to the nearest well, 6SU. (c) Fracture distribution along cores 1 to 4. The lengths of the vertical bars denote certainties in fracture attribution. Hydraulic fractures are placed on the upper half of the plot while natural fractures are on the lower half. See Gale et al. (2018) for detailed definitions of “sure” (certain), “probable”, and “best guess” (guess) fracture attributions, as well as the differences between “intact” and “reactivated” natural fractures.

For each scenario, we selected five analysis windows (as shown in the **Table 4.1**), each 100 ft long, and perform hypothesis test for each analysis window to determine whether the null hypothesis should be accepted or rejected. In each analysis window, we use the following procedures to calculate a *p*-value, which is the probability of falsely rejecting the null hypothesis. In other words, a higher p-value indicates that the null hypothesis, namely the fractures in the analysis window follow a Poisson distribution, is more likely to be true. The calculation procedure goes as follows:

1. We divide the 100-ft long analysis window into 50 sampling intervals, each 2 ft long.
2. We calculate the average number of fractures, λ, expected in a 2 ft-interval as the total number of fractures in the analysis window divided by 50.
3. If the fractures follow a Poisson distribution, then the probability of observing k fractures in a 2-ft interval is:
   $$p_e(k) = e^{-\lambda}\frac{\lambda^k}{k!}$$
4. We compute the fracture occurrence probability $p_r(k)$ among the 50 sampling intervals based on the fracture data.
5. We provide $p_e(k)$ and $p_r(k)$ to Python function scipy.stats.chisquare() to compute the *p*-value for the analysis window.

***Table 4.1**: Poisson distribution test results*

Analysis Window (ft):		9290-9390	9390-9490	9480-9580	9550-9650	9620-9720
Hydraulic fractures only	Fracture density (count/ft):	0.46	0.84	1.15	0.69	0.71
	p-Value (%)	19.2	3.7	46.7	76.5	0.2
Hydraulic fractures + reactivated natural fractures	Fracture density (count/ft):	0.7	0.99	1.26	0.71	0.80
	p-Value	87.0	0.006	7.3	80.9	3.2

In either scenario (hydraulic fracture only and combining hydraulic and natural fractures), three out of the five analysis windows have *p*-values greater than the typical rejection threshold value 5%. In other words, fractures in these three analysis windows likely follow the Poisson distribution. The clustering pattern observed is perhaps a natural manifestation of a random distribution of fractures, instead of being an indication of "swarming" behavior.

4.4 The Investigation of the Mechanism of Fracture "Swarming"

Based on an informal survey of the literature and expert opinion, we consider the following four hypotheses regarding the mechanisms for closely spaced hydraulic fractures.

Branching:

The branching hypothesis states that a hydraulic fracture can branch into two (or more) advancing fronts when intersecting with natural fractures or other discontinuities in the rock. As the propagation speed of typical hydraulic fractures, usually in meters per second, is orders of magnitude slower than the Rayleigh wave speed, the condition for spontaneous branching is not met. Branching of hydraulic fractures is likely triggered by natural discontinuities, particularly natural fractures in the rock. In this section, we perform in-depth analyses of the process of a hydraulic fracture intersection a natural fracture as well as the resultant branching.

To schematically depict the process of hydraulic fractures intersecting natural fractures, we place several natural fractures (NF1 to NF5, as shown in **Figure 4.5**) trending in the northeast-southwest and northwest-southeast

directions intersecting the projected hydraulic fracture trajectories. We simultaneously stimulate three hydraulic fractures, 20 m apart from each other, under a total injection rate of 20 bbl/min. As the purpose of this study is to investigate physical mechanisms under generic scenarios, we adopt conditions and parameters favorable for fracture branching. Also, we only include a small number of natural fractures to enable clear visualization of fracture interactions. Consequently, completion design and fracture density do not necessarily follow the actual field values.

The fracture configuration, including the distribution of fracturing time (i.e., the time when fracturing took place in each location) and the distribution of fracture aperture, is illustrated in **Figure 4.5(a)** and **(b).** Note that these two plots magnified the model in the y-direction by three times to allow clear visualization. Three of the natural fractures, NF1, NF2 and NF4, generated new fracture area driven by fluid /pressure from their respective intersections with hydraulic fractures. The new fracture areas originating from natural fractures are labeled as NF1A, NF2A, and NF4A. Taking the intersection between HF2 and NF1 as an example, we see in **Figure 4.5(a)** that the lower portion of HF2 was temporarily "arrested" by NF1. The color gradient on NF1A indicates that its growth was very slow until it stopped eventually. The upper portion of HF2 continued to propagate in a fast pace after the arrest of the low portion. Eventually, the upper portion grew downwards to "bypass" (Fu et al., 2015) the arrest to fill "Area a" denoted in the figure.

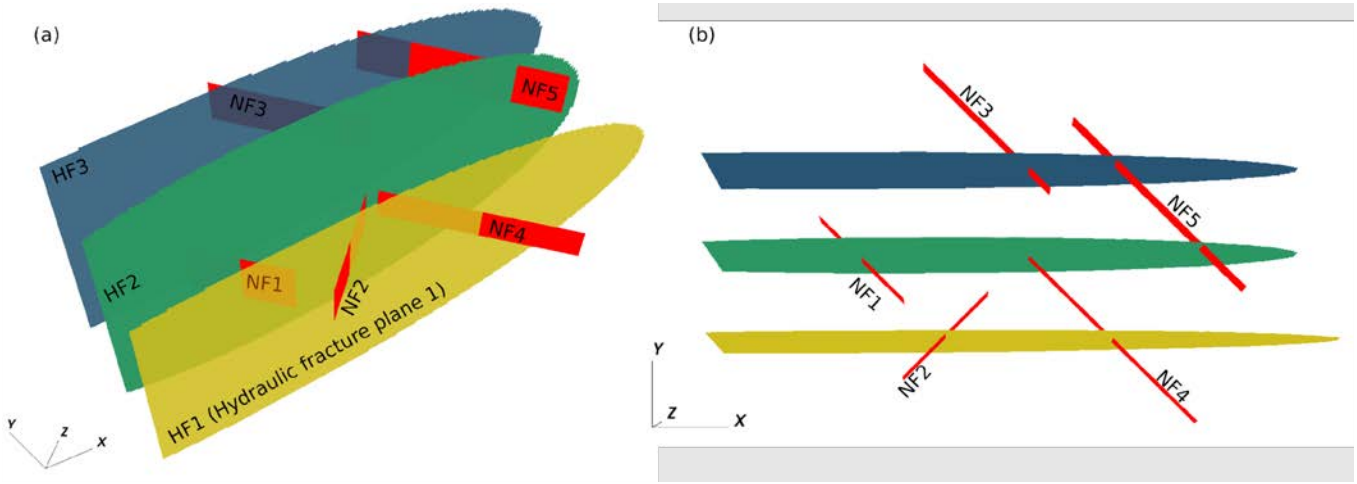

Figure 4.5: The initial configuration of natural fractures, labeled as NF1 to NF5, in relation to the three expected hydraulic fracture planes (HF1 to HF3). Note that the shapes of the hydraulic fracture planes are nominal only.

Although in effect this does form a "branching" configuration, the generated extra fracture area is much smaller than the area of the new hydraulic fractures. The reason can be demonstrated by the horizontal slice marked on **Figure 4.6(a)** and shown in **4.6(c)**. Deformation in the slides is exaggerated by 2000 times allow visualization of the deformation. It is clear that the original NF1, although hydraulically connecting NF1A to HF2, it is nevertheless a "bottleneck" limiting the flow rate and thereby the growth speed of NF1A. In other words, new fracture areas spinning off from natural fractures are likely suppressed by both the stress shadow from the main hydraulic fractures and the limited fluid supply though the natural fractures which are generally not in favorable orientations for opening against the in situ stress. The above simulation, although performed in artificially favorable conditions for branching, demonstrates that though "branching" is possible, it is unlikely responsible for massive surface area generation.

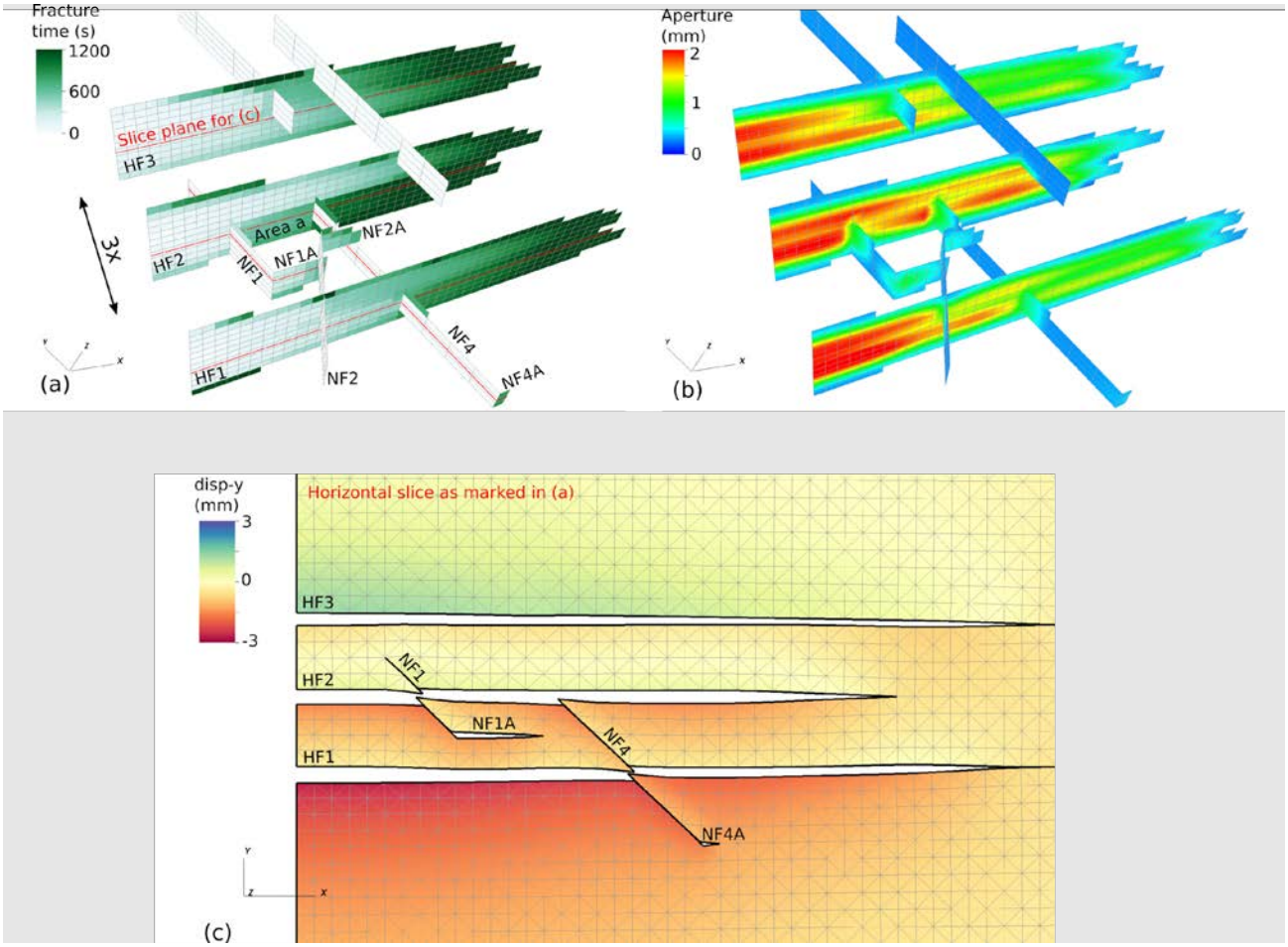

Figure 4.6: Fracture configuration after 1500 seconds of stimulation. In (a) and (b), the fractures are colored according to the fracturing time and aperture, respectively. The model's dimension in the y-direction is magnified by three times to allow clear visualization. Note that this has caused the orientations of the natural fractures to appear rotated. (c) A horizontal slice of the model with its vertical location annotated by the red line in (a). Deformation is exaggerated by 2000 times.

Poromechanical effects:

This is an extension to a hypothetical process proposed by Savitski (2020). In this scenario, the high fluid pressure in a main hydraulic fracture can be conducted to a distance beyond the stress shadow by a rock layer with high diffusivity. Tensile stress can be generated by the poromechanical effect, resulting in children fractures parallel to the main hydraulic fracture. Savitski (2020) has demonstrated the possibility of generating tensile effective stress and thus the nucleation of children fractures. In the current work, we will present a fracture-centric model to assess the propagation potential of these children fractures. Savitski (2020) suggested that a fully numerical approach is needed to study more realistic scenarios such as multiple fractures and stress interference. In this work, we did not intend to fully generalize Savitski's theory. Instead, we evaluated the potential of generating and propagating child fractures due to this poromechanical mechanism.

We only considered the "optimistic" extreme scenario. It entails a plane-strain static finite element model pre-conditioned to an in situ Shmin profile calculated for the HFTS site based on ISIP (instantaneous shut-in pressure), DFIT (diagnostic fracture injection test), and sonic well logs (Fu et al., 2021). A main fracture, extending 90 m in the vertical direction, is placed in the model, and subjected to a hydrostatic pressure that dilates the fracture to a stress intensity factor SIF = 2.0 MPa·$^{m0.5}$ at the top tip in the absence of any child

fractures. We then place three child fractures parallel to the main fracture: one at the height of the main fracture's upper tip, one near the bottom tip, and one in the middle height. Each of the three child fractures is 12 m in vertical extent and is subjected to the same fluid pressure at the corresponding height in the main fracture. Savitski (2020) hypothesized that child fractures could be hydraulically connected to the main hydraulic fracture via a high permeability layer or a permeable bedding plane. The boundary condition applied to the child fractures in these simulations implies that the hydraulic connection between the main fracture and the child fractures is extremely strong, which is unlikely in a real shale formation. That is why this is considered an extremely optimistic scenario for child fracture propagation. We also vary the horizontal distance between the child fractures and the main fracture from 5 m to 20 m. **Figure 4.7** visualizes the dilation patterns (deformation is exaggerated by 1000 times) of the fractures as well as SIF values at the fracture tips.

In all the scenarios considered, the top and middle child fractures are dilated, evidenced by the positive SIFs. The bottom child fracture is closed due to the surrounding stress environment. As the model did not enforce a no-penetration condition, the two walls of a closed fracture would virtually "penetrate" into each other, resulting in negative SIF values. This does not negate our conclusions regarding the potential for this mechanism. The following observations are useful for understanding the growth prospect of the child fractures.

1. All tips of the child fractures have lower SIFs than the main hydraulic fracture. This means if the fluid pressure in the hydraulic fracture is so that the main fracture can overcome the rock's toughness (but not higher), none of the child fractures can grow.
2. SIFs at both tips of the middle child fracture and the lower tip of the upper child fracture increase as the child fractures are farther away from the main fracture. This precludes the growth child fractures close to the main fracture. Therefore, the observed fracture spacing in the order of inches to feet cannot be attributed to this mechanism. Note that the smallest fracture distance of 5 m simulated was limited by mesh resolution; how fracture spacing affects the dilation of child fractures is clear in the simulation, nevertheless.
3. The SIF at the top tip of the upper child fracture increases as the child fracture is closer to the main fracture. This is because this tip can enter the tensile incremental stress zone around the tip of the main fracture. Consequently, this child fracture still cannot grow beyond the influence of the main fracture.

Recall that the pressure applied on the child fractures in these simulations is extremely optimistic. Under realistic field conditions, pressure in the child fractures is likely much lower. Although the simulation results do not preclude the possibility of generating fractures by the poromechanical mechanism proposed by Savitski (2020), the results do indicate that it is unlikely to generate an extensive set of fractures matching the field observations at the three sites.

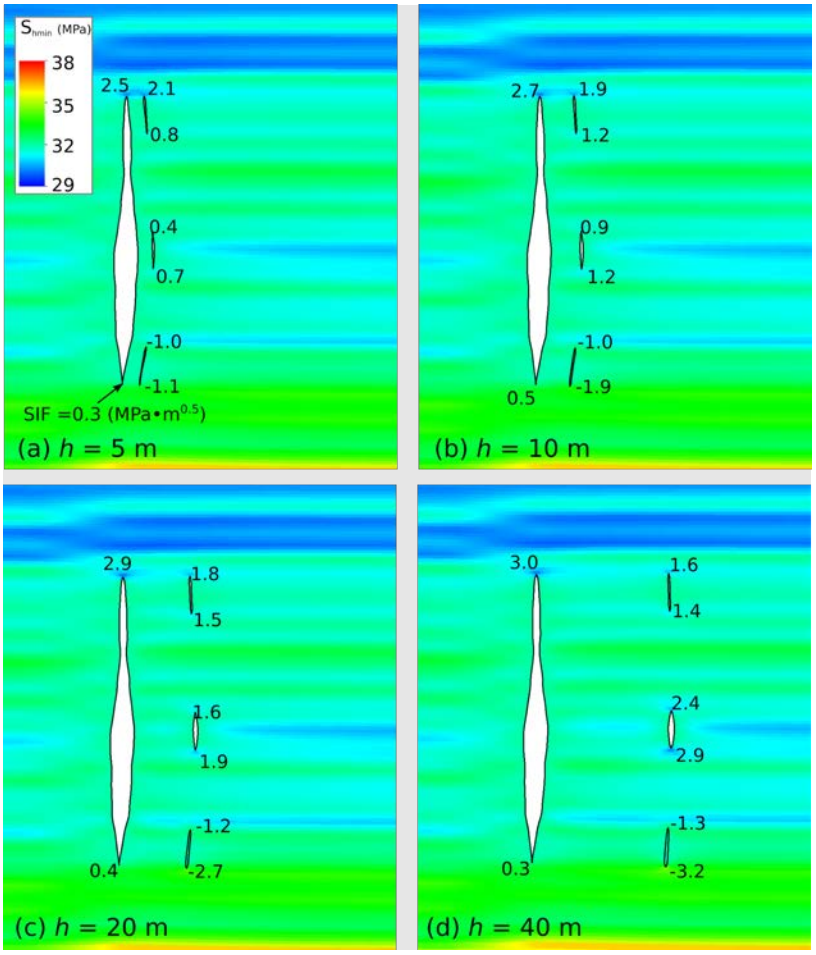

Figure 4.7: The interaction between a main hydraulic fracture and potential child fractures initiated near the main fracture. Each of the child fractures is 12 m "tall". The horizontal distance between the main fracture and the child fractures varies between 5 m and 40 m. The values in the figure are stress intensity factors (in MPa·m$^{0.5}$) at fracture tips. The deformation is exaggerated by 1000 times. A negative SIF value indicates the fracture should be closed near this tip.

Misaligned in situ stresses:

This mechanism relies on relatively complex 3D configurations of rock formations and fractures. In this example shown in **Figure 4.8**, a horizontal well is placed in rock Layer A. We assume Shmin in Layer A and that in the above Layer B misalign with each other. For instance, Shmin in Layer B is in the north-south direction while that in Layer A is in an oblique angle. Consequently, hydraulic fractures initiating from the well (only one illustrated in **Figure 4.8** as labeled "Fracture A") have an oblique strike angle. When this fracture intersects and propagates into Layer B, it is likely to reorient to strike in the east-west direction as dictated by the Shmin direction in Layer B. It is therefore possible for a single fracture in Layer A to spin off multiple parallel fractures in Layer B. Though geomechanically feasible, this mechanism requires a specific 3D configuration. Considering that densely spaced hydraulic fracturing is an "ubiquitous" behavior in all the three experiments available, this mechanism is unlikely the main reason for the observed densely spaced fractures and is therefore not explicitly simulated in the current work.

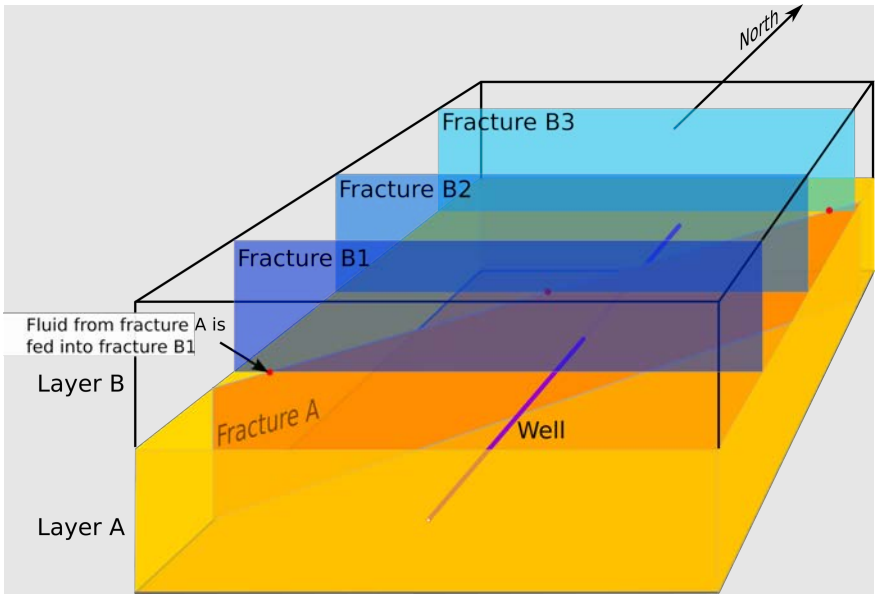

Figure 4.8: A conceptual illustration of hypothetical mechanism #3 for generating closely-spaced parallel hydraulic fractures. Rock Layer A and Layer B have misaligned S_{hmin} orientations. The three rod dots denote where Fracture A spins off three parallel fractures in Layer B.

Near-wellbore processes:

By process of elimination, this left us with the fourth mechanism, which suggests that fracture swarms develop in the near-wellbore region. Our last hypothesis states that most of the observed hydraulic fractures initiate from individual perforation holes. Traditionally, this scenario was thought to be inhibited by stress shadowing. In this work, we focus our simulations on the process of multiple perforation holes breaking down in succession as well as parallel fracture propagation in the near-wellbore region, both in the presence of stress shadowing. Leveraging our previous experience with modeling fracturing processes in the near-wellbore environment (Sherman et al., 2015), we constructed a set of models to test how swarms may develop. These models include an explicitly meshed wellbore, a set of initial perforations, and mesh designed to accommodate natural curving that expected in the environment. Fracturing fluid is injected into the wellbore, which can then flow outwards through the perforations following an empirical perforation friction model. This model causes a pressure drop to develop between the well and the fractures, which is proportional to flow rate and encourages equal fluid flow distribution between the fractures.

After calibrating this model, we conducted a sensitivity analysis to determine the model parameters that could lead to swarm development. We considered the following: perforation phasing, perforation spacing, perforation size, in-situ stress, and the amplitude/length-scale of near-wellbore curving. In each of the cases we tested, we found that a high percentage of the initial perforations broke down and generated fractures which proceeded to propagate outwards to a distance several times the radius of the wellbore. In addition, we found that these models naturally produced features such as wellbore pressure breakdown that are observed in the field.

Figure 4.9 shows an example of the simulation results for a model with eight initial perforations aligned 45° from the direction of σ_{hmin}. In this case, fractures initiate from pairs of perforations, beginning with the outer-most and moving to the inner-most perforations over time. Note that as the early fracture initiate, the pressure in the wellbore continues to increase, reflecting the limited ability of these fractures to take fluid compared to the pumping rate. This is due to a combination of perforation friction related pressure losses and the initial limited size of the fractures. Around 7-8 seconds, the pressure in the wellbore tapers off as the combined fractures become capable of accepting the fluid being injected into the wellbore. Any perforations that have not

developed at the point of maximum pressure (or 'breakdown'), will remain dormant as the pressure in the system continues to decline. The 3D snapshot of the fractures shows that the distribution of aperture in each fracture is complicated. This is a consequence of stress-shadowing between individual fractures, which tends to produce low values of aperture in regions where neighboring fractures have high aperture. In some cases, we found that the stress shadowing effect could produce fractures that are non-circular.

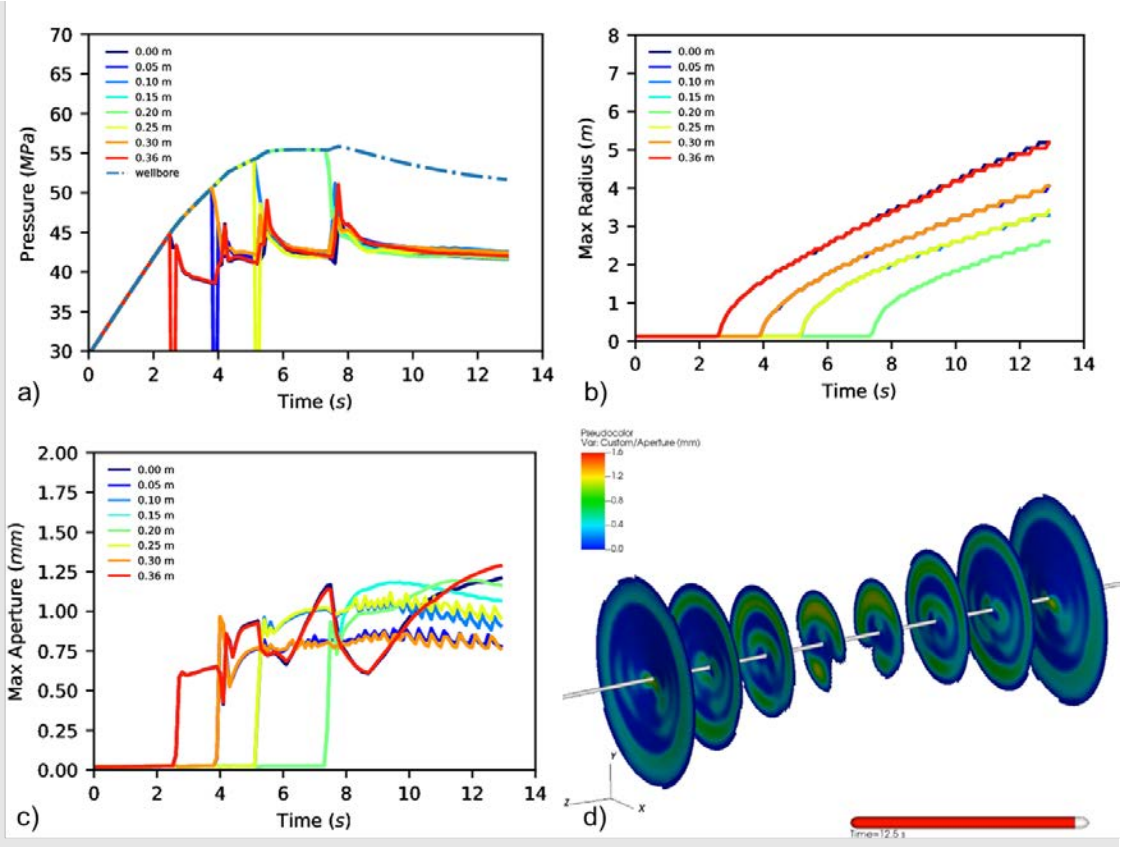

Figure 4.9: Example results from the near-wellbore fracture imitation sensitivity analysis for a model containing eight initial perforations aligned 45° from the direction of the far-field σ_{hmin}. For each fracture cluster, we show (a) the pressure at the perforation, (b) the maximum radius, (c) the maximum aperture over time, and (d) a 3D snapshot of the fractures after 12.5 seconds of pumping (showing aperture in color, with an exaggerated scale in the z-direction).

Another key piece of information arising from the sensitivity analysis includes the simulated wellbore pressures over time, as these are directly measurable quantities. **Figure 4.10** shows an example of how wellbore pressure can change with the orientation of the perforations. For the 0° case, the perforations initially experience the largest values of compressive stress in the near-wellbore region. This causes the fractures to break down later when the pressure in the wellbore is higher. As the angle increases, the perforations experience lower values of initial stress, which tends to reduce the value of breakdown pressure. The variations in this trend highlight that these processes are nonlinear, leading to very different end-results for similar initial conditions.

4.5 Conclusions

The reservoir-scale fracturing modeling task in this project achieved four major goals: (1) We developed a practical way to model the effects of fracture swarming without the need to explicitly representing closely fractures in the mesh grid; (2) we studied the role of stress distribution on fracture's growth and the practical

implications in terms of well trajectory design; (3) we explored and evaluated possible mechanisms behind the observed fracture patterns; and (4) the results provided fracture networks for reservoir-scale production simulations as detailed in subsequent chapters. The first two aspects of work can be directly implemented in practice. The third is perhaps the most scientifically significant aspect, although the scarcity of direct observation data makes it impossible to draw definitive conclusions. Nevertheless, the following insights can still be useful.

The statistical analysis found that the observed fracture spacing pattern could be the natural consequence of a Poisson process. As a Poisson distribution only has one parameter, which in this case is the mean fracture spacing, the essence of the fracture spacing distribution is therefore the overall fracture density, instead of the very small spacing in certain segments. Simulations indicate that branching (after intersecting natural fractures) and the poromechanical effect could both generate additional fracture areas. However, in both cases, the newly generated fracture area is much smaller than the hydraulic fracture area. They are, therefore, unlikely the primary mechanism for generating the observed fracture density. A major issue for both mechanisms is that they are "circumstantial", or in other words, rely on conditions that do not ubiquitously exist. For instance, the branching mechanism requires particular conditions for the natural fracture system. However, the Eagle Ford formation is known to have much lower natural fracture density than the Permian Basin that hosted HFTS and HFTS-2 experiments. The natural fracture characteristics also differ significantly between the HFTS and HFTS-2 sites. The fact that these three sites have remarkably similar fracture spacing patterns appears to invalidate the branching hypothesis. Finally, we established the physical feasibility of generating sustained hydraulic fractures from most of the individual perforation holes. The results proved that the breakdown of a perforation hole does not preclude the breakdown of neighboring perforation holes. Also, fractures in the near-wellbore region can propagate in parallel even in the presence of strong stress shadowing. In both scenarios, perforation friction plays a key role. A remaining discrepancy is that this mechanism still cannot explain the observed fracture density. The average perforation density for HFTS wells was between 0.18~0.3 perf per ft (Salahshoor et al., 2020). HFTS-2 wells' average perforation density was 0.12 perf per ft (Zakhour et al., 2021). Both are significantly lower than the observed mean density. This suggests that there could be other mechanisms also generating fractures. The main practical implication of these findings is that the focus of well completion optimization should be near-wellbore processes, including perforation clustering and phasing control, instead of the interactions with natural fractures.

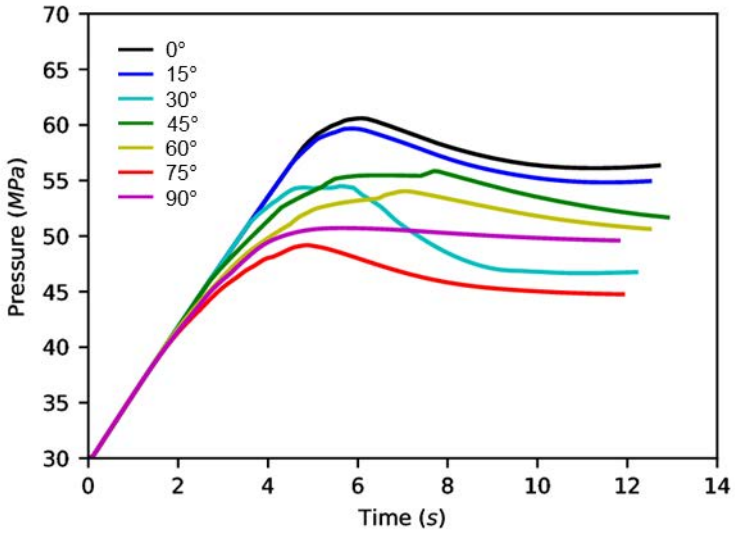

Figure 4.10: Results from near wellbore fracture initiation models each with eight perforations aligned at different angles with respect to the far-field σ_{hmin}.

5. Reservoir-scale Production Simulations

Shale reservoir production simulation requires knowledge on media properties (e.g., matrix permeability, matrix pressure, initial saturation), fracture properties (e.g., fracture geometry, fracture permeability) and fluid properties (e.g., bubble point pressure, relative permeability function), and detailed information on these properties is often unavailable for field-scale reservoir simulations. For hydraulically fractured shale reservoirs, an important uncertainty comes from the characterization of the multi-scale fracture network, and a challenge in shale reservoir production history-matching involves selection of the important fracture parameters. This requires improved understanding on the underlying physical configuration of the fracture network. With a combination of field observation, sampling and numerical simulation at the Eagle Ford shale, Raterman et al. (2019) summarized the key elements that are necessary to characterize the fracture network for shale reservoir simulations, which are (1) non-uniform principal hydraulic fractures, (2) dense but short secondary fractures, (3) a conductive zone near the well, and (4) stress-dependent fracture properties.

The reservoir-scale production simulations described here are performed by MMP's LBNL team. We deploy a multi-scale fracture network model following Raterman et al. (2019), aiming at matching the production history of shale oil and gas in the HFTS site. Section 2.1 describes use of the GEOS simulator to create non-uniform hydraulic fractures based on measured stress distribution and recorded pumping schedule (Item 1 of Raterman et al, 2019). The initial condition of the reservoir (initial pressure, temperature, saturation) is available through well log observations. The matrix permeability is obtained from core samples. Thus, the major uncertainty for our production simulation is on building the fracture network for the secondary fractures (Items 2 and 3 of Raterman et al., 2019). Our proposed secondary fracture model includes four uncertain parameters representing the geometry and permeability of the secondary fractures. By manually tuning these parameters, reasonable history matching results can be achieved. The sensitivity of production rates to these parameters and to the fracture closure mechanism (Item 4 of Raterman et al., 2019) is also examined. The goal of this study is to advance knowledge in configuring the multi-scale fracture network, understanding the role of secondary fractures in multi-phase production, as well as providing insights on selecting uncertain parameters for history-matching purposes. Insights from geomechanical hydraulic fracturing analysis have been used to fine-tune representation of primary fractures in flow simulations (Sections 3 and 4), while micromechanical studies were used to evaluate the importance of fracture closure (Sections 6.1 and 6.2) and microchemical studies were used to understand property alterations as a result of chemical reactions, both with regards to near-fracture matrix properties (Sections 7.1 and 7.2) and fracture properties (Section 7.3).

5.1 Preliminary Production Simulations and Sensitivity Studies

The TOUGH+ reservoir-scale production model takes GEOS predictions of fracture geometry (number, location/shape, aperture) and remaps them into the TOUGH+ meshing framework. Specifically, we maintain both the detailed geometry of the stimulated zone (hydraulic fractures, stimulated natural fractures) and its internal state (spatial distribution of proppant, stress shadowing, etc.) in the transfer from GEOS to TOUGH+. As discussed in Section 2.3, to reduce computational costs, the domain of each simulation contains only one primary hydraulic fracture. This is similar to the concept of a *stencil* used in recent simulation studies of fractured reservoirs, and represents the smallest repeatable unit that can be defined within a reservoir with parallel horizontal wells. This is the smallest unit that can be used to characterize production behavior in such a system, and is often the largest unit that is practical for full-physics reservoirs production simulation. This allows us to use very fine discretization to capture steep gradients and non-linear effects common in unconventional reservoirs that may be lost when coarser discretization is used. It can be scaled up to estimate production from a multi-fractured horizontal well by adding production from individual stencils, or by multiplying by the number of stages (Olorode et al., 2013).

To demonstrate the application of the new coupled workflow, we simulated a complete stage from the HFTS Well 4SM (Middle Wolfcamp formation), which includes five perforation clusters with a 16 m cluster spacing. Fracture swarms are accounted for in the developed upscaling approach, and we assume that each cluster is associated with eight closely spaced hydraulic fractures that are represented by a single fracture in the simulation with effective properties determined from the upscaling law. Numerical experiments, based on the five-cluster system described in Section 4.1, have been conducted to examine the effect of (1) uncertainties in initial shale permeability, (2) uncertainties in initial water and oil saturations, (3) degree and treatment of heterogeneity in the representation of the stimulated fractures, (4) changes in fracture permeability due to proppant rearrangement, embedment or breakage, (5) changes in fracture permeability due to chemical reactions from exposure to stimulation fluids, and (6) development (and properties) of an altered (lower permeability) layer ("skin") at the fracture-shale interface due to chemical alteration leak-off layer thickness. Analysis of these simulations has revealed:

1) Initial water saturation in the leak-off layer affects early-time production behavior (post-shut-in)
2) Gas exsolution in the fracture, and early-time gas production, is sensitive to mean fracture aperture
3) Oil and gas production rates, derived from stage-by-stage simulation, are overpredicted at longer timescales compared to HFTS field data.

Many of these potential effects were further examined by the laboratory experiments discussed in the subsequent sections. Characterization of core samples from the HFTS site also provided us with more detailed knowledge of the state of the reservoir post-fracturing. These results from other MMP tasks provided key clues about the workings of the reservoir. In particular, we realized that (1) natural/background fractures provide the bulk of usable permeability within the matrix, (2) secondary fractures (parallel to the primary fracture swarms) are likely to contribute significantly to production, and (3) changes in the reservoir during production (interference and fracture closure) are required to capture long-term production behavior. The reservoir simulation task thus focused on attempts to history-match production data as a means of both validating the new simulation framework and extracting new insights about hydraulically fractured reservoirs like HFTS.

5.2 History-Matching of Reservoir Production with a Multi-scale, Non-Uniform Fracture Network

While the HFTS dataset is extensive, the characterization of the fractured zones surrounding the various well stages is still limited. Thus, we used a combination of GEOS-derived fracture geometries, analysis of geophysical data discussed in Section 3, and the results of the preliminary reservoir simulations (parametric sensitivity studies) to develop stage-by-stage reservoir models which can then be fine-tuned via history matching to production data. The reservoir production model included three key components:

1) Heterogeneous primary fractures, upscaled from GEOS fracture simulations
2) Inclusion of secondary fractures in the zone surrounding the primary fractures
3) Incorporating the ability to close primary and secondary fractures in response to inflections in production rates as seen in the dataset

Item 1 was addressed in Section 2.3, and the methodology used to implement the fractures in TOUGH+ remains the same for the history matching simulations. For Item 2, rather than explicitly representing secondary fractures (unrealistic to the heterogeneous distribution of such fractures and the lack of detailed data describing the fracture network at specific stages), we used a multi-continuum representation of matrix-fracture interactions (MINC). The secondary fracture zone, or Stimulated Reservoir Volume (SRV), was represented by a dual-porosity, dual-permeability (DPDP) model applied to all matrix cells. The secondary fractures were represented as the "fracture" (i.e., higher permeability, higher porosity) continuum of the DPDP model. The

permeabilities of the secondary fractures were set element-wise and anisotropically following the upscale methods described in Section 2.3. This approach also results in a decreasing permeability along the secondary fractures as the distance to the well increases. When the distance to the well exceeds a certain value such that $b(x,z) < b_{min}$, the fracture continuum is converted back to the matrix continuum. Since the maximum aperture is obtained near the wellbore, permeability parallel to the primary fractures is relatively large near the wellbore as well. This corresponds to the "conductive zone" near the well as mentioned in Raterman et al. (2019). An illustration of the proposed secondary fracture model can be found in **Figure 5.1**.

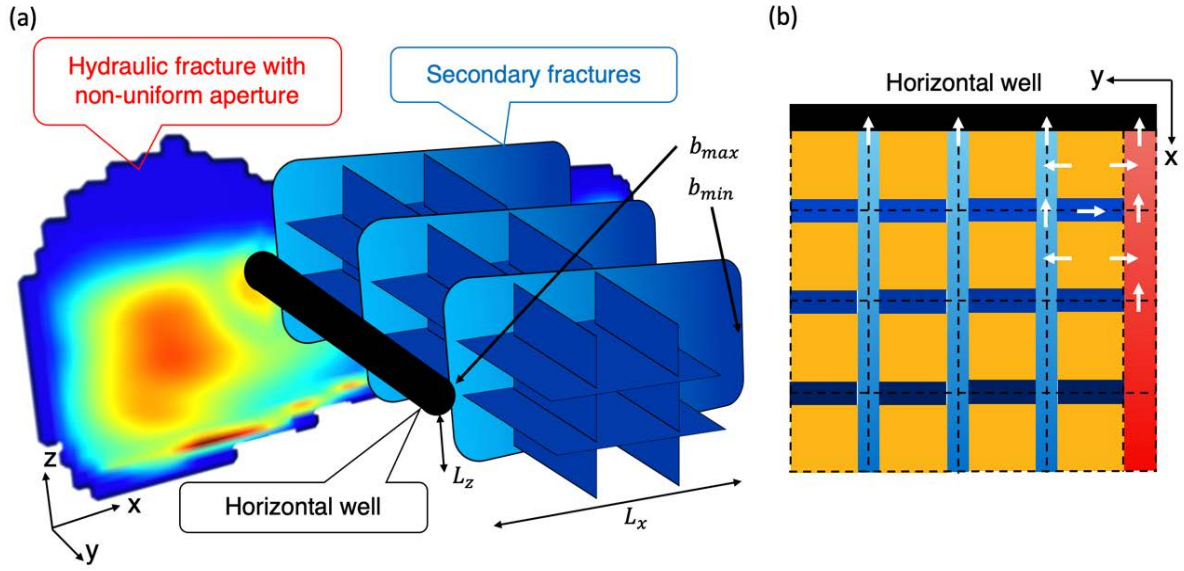

Figure 5.1: Illustration of the proposed secondary fracture model, with (a) a concept figure shows the spatial relation between the primary hydraulic fracture, the secondary fracture network and the horizontal well, and (b) the multi-scale fracture network represented on MINC mesh, where the dashed boxes represent computational grids, red color represents the hydraulic fracture, blue color represents the fracture of the MINC grids and orange color represents the matrix of the MINC grids. White arrows indicate flow direction. Color gradients indicate non-uniform permeability, with cooler colors implying smaller permeability.

Stress-dependent permeability is an important factor that should be accounted for in production simulations (Cui et al. 2020; Jimenez & Aguilera, 2019; Wan et al. 2020), and while development of a multi-continuum geomechanical modeling system is beyond the scope of this project, we addressed Item 3 by modifying fracture properties (for both primary and secondary fractures) in response to inflections in the production rate as seen in the dataset (thereby representing a decreased fracture aperture or eve fracture closure. This is certainly a primitive treatment as the change in permeability becomes non-continuous in time, and the amount of reduction is to be treated as an additional adjustable parameter. However, we aim to show the importance of fracture closure and reserve more complete flow-geomechanics modeling to future studies.

Production data from the HFTS demonstrated that flow rates from different hydraulic fractures within the same stimulation stage can have similar trends and magnitudes. To account for inter-well variability, two hydraulic fractures from well 4SM and 4SU respectively were selected for modeling. The former well is located in the middle Wolfcamp formation and the latter is in the upper Wolfcamp. **Figure 5.2** shows the geometry and the aperture of the two representative primary hydraulic fractures used in this study. Due to the transport and deposition of proppants, as well as the stress shadowing effect, the propped aperture for well 4SM (**Figure 5.2a**) contains two local maximum on the far ends of the wings. The modified aperture (**Figure 5.2b**) is calculated as described in Section 2.3, which reduces the extreme aperture values to improve model convergence.

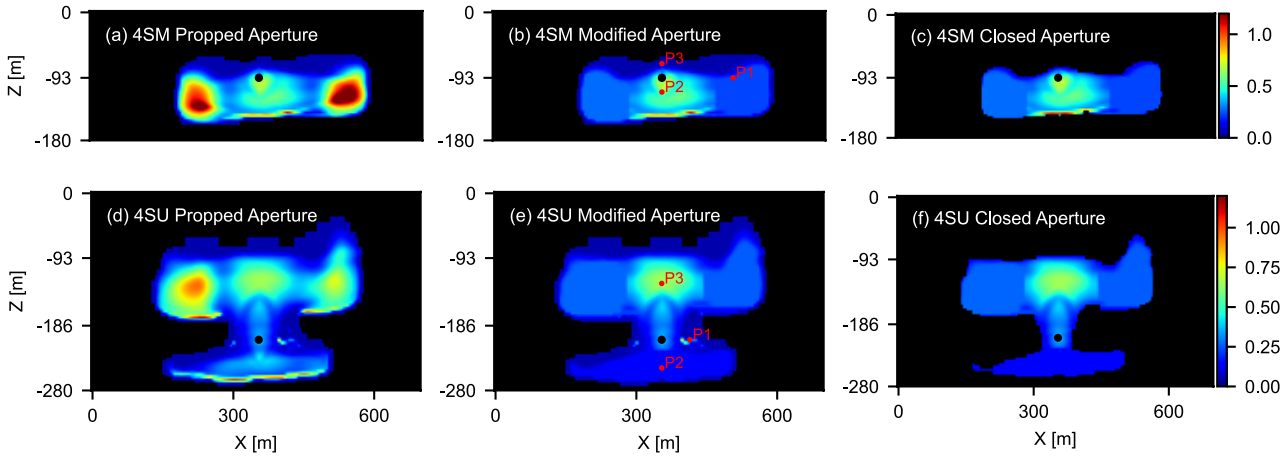

Figure 5.2: Geometry of the two hydraulic fractures used in this study. The colormap indicates the magnitude of aperture (mm). The first column (a, d) shows the propped aperture modeled with GEOS. The second column (b, e) shows the corresponding modified aperture. The third column (c, f) shows the closed aperture, where the unpropped region is removed. The black dots represent the wellbore. The red dots are pressure monitoring locations.

In hydraulic fractures, the permeability of the propped aperture is orders of magnitudes greater than that of the unpropped aperture (Wu et al., 2021). Thus, the closed aperture is obtained by simply removing the unpropped regions (proppant volume fractions less than 0.002) from the hydraulic fracture (**Figure 5.2c**). **Figures 5.2d-f** show the propped, modified and closed aperture for the hydraulic fracture in well 4SU. Compared with well 4SM, the 4SU fracture has a larger surface area and a unique I-shaped geometry caused by the heterogeneous stress field.

The vertical distance between the two wells is about 100 m. The horizontal offset is also about 100 m. The width of the computational domain is 16 m, which equals the distance between adjacent perforation clusters at HFTS. The reservoir properties and simulation parameters are described in Li et al. (2022).

In addition to reference cases run using the base 4SM and 4SU fracture models, four test scenarios were designed to assist early-time calibration of the modeled production to HFTS data. The 4SM A- scenario (**Table 5.1**) investigates the effect of reducing fracture height. The 4SM b+ scenario investigates the effect of increasing the maximum aperture of the secondary fractures. The 4SM r+ scenario examines the effect of increasing the anisotropy ratio, which results in lower permeability perpendicular to the fractures compared to the base case. The 4SM s+ scenario increases the initial oil saturation by 0.01, which leads to a complementary reduction in initial water saturation (note that the initial state of the reservoir only contains water and oil). After production begins, gas is gradually released from oil through depressurization (Clarkson et al. 2020). The change in the initial saturation is relatively negligible compared with typical resolution of the field data and the spatial heterogeneity of the reservoir properties. However, we see that such a tiny increase in oil saturation has strong influence on the history match.

Table 5.1: Simulation scenarios performed in the present study and the corresponding parameters for the secondary fractures. For each scenario, one can optionally close the primary hydraulic fracture, the secondary fractures or both types of fractures at any time after the simulation starts.

Case ID	$L_x\ [m]$	$L_z\ [m]$	r	b_{max} [m]	b_{close} [m]	s_o
4SM Base	100	100	1000	1.5×10^{-7}	1.2×10^{-7}	0.56
4SM A-	100	50	1000	1.5×10^{-7}	N.A.	0.56
4SM b+	100	100	1000	2.0×10^{-7}	N.A.	0.56
4SM r+	100	100	5000	1.5×10^{-7}	N.A.	0.56
4SM s+	100	100	1000	1.5×10^{-7}	N.A.	0.57
4SU Base	100	150	1000	2.4×10^{-7}	1.5×10^{-7}	0.57

Sensitivity to the Secondary Fractures:

Figure 5.3 presents the cumulative water, gas and oil production from well 4SM as modeled by TOUGH+. It can be seen that with the baseline scenario (4SM Base), all three phases can be matched to the production data (dotted line) at early times. After 100-200 days, the model predictions begin to diverge from the data. By 1500 days, the baseline scenario overestimates the cumulative production by 27%, 47%, 20% for water, gas and oil respectively. We hypothesize that this could be evidence of fracture closure that is neglected in the static reservoir model.

Scenario 4SM A- reduces the height of the secondary fractures, resulting in decreased production of all three phases. Although a better model-data agreement is achieved at late stages of production, the modeled water production is significantly underestimated. Gas production is also underestimated after 1,200 days. For 4SM s+, the initial oil saturation in the reservoir is increased by 0.01, and the total water produced decreases by 17% while the total oil produced increases by 59%. The initial water saturation used in this study is close to the residual saturation (Li et al., 2022). This could explain the reason why production is strongly sensitive to the initial saturation.

The 4SM b+ scenario increases the maximum aperture of the secondary fractures, and as a result overestimates production of all three phases. However, compared with the baseline scenario, the cumulative water production is lower. A larger aperture enhances pressure drop within the SRV, releasing additional gas and improving the effective permeability for the gas and oil phase, which also restrains the production of water. This argument can be used to explain the 4SM r+ curve as well. As the anisotropy ratio increases, the permeability perpendicular to the fracture decreases. This should lead to reduced production of all three phases because the SRV is less conductive in general, and the decrease in permeability also hinders matrix depressurization such that less gas is exsolved from oil. As a result, the cumulative oil production is slightly higher than that of the baseline scenario. These results indicate that the complexity of the production behavior thanks to multi-component, multi-phase interactions that are also regulated by fracture properties and fracture network geometry.

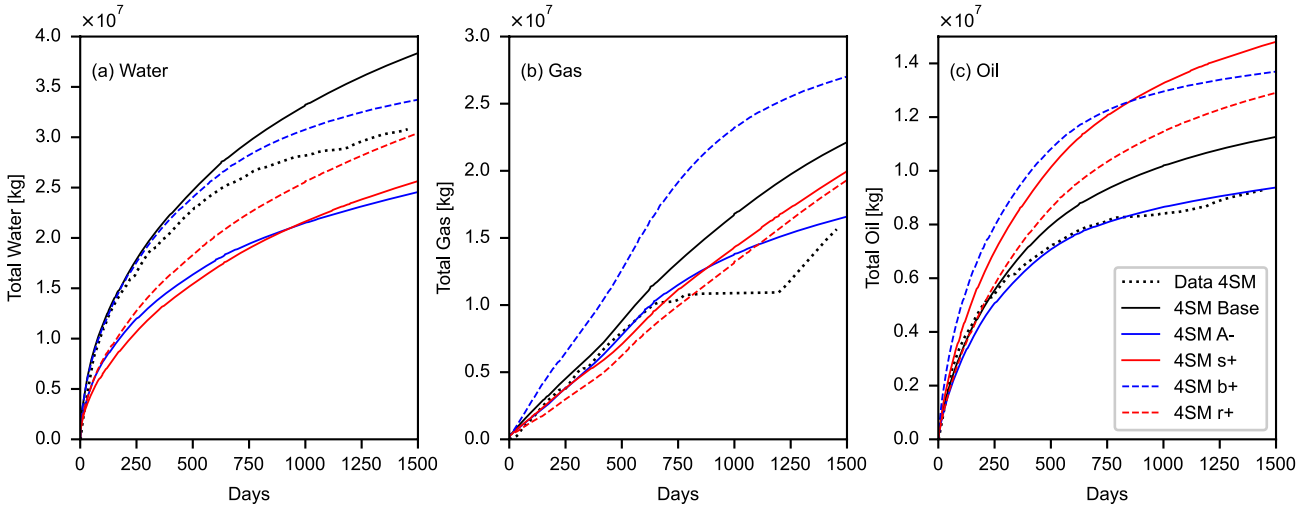

Figure 5.3: Cumulative production of (a) water, (b) gas and (c) oil from well 4SM. The parameters for the secondary fractures and the oil saturation are adjusted to investigate their effects on history matching.

Sensitivity to Fracture Closure (4SM and 4SU):

Figure 5.4 shows the cumulative production of the 4SM base case if fracture closure is included. Fracture closure is assumed to begin at 150 days, based on inflection points in the HFTS production data. We test scenarios that close the main hydraulic fracture alone (i.e., removing the unpropped regions), the secondary fractures alone (i.e., reduced the fracture aperture to b_{close}), and all the fractures together. When both the primary and secondary fractures close, the modeled water and oil production shows good agreement with the field data. If we close only the primary hydraulic fracture, the oil flow rate (i.e., the slope of the cumulative production curve) is slightly underestimated at 1,500 days. If we only close the secondary fractures, the water flow rate is overestimated at 1,500 days. In all test scenarios, the gas flow rate at 1,500 days is underestimated, but this reflects anomaly in gas production data (a temporary cessation of gas production unique to the 4SM well)—i.e., fracture closure is clearly needed to match gas production data before the anomaly at 750 days.

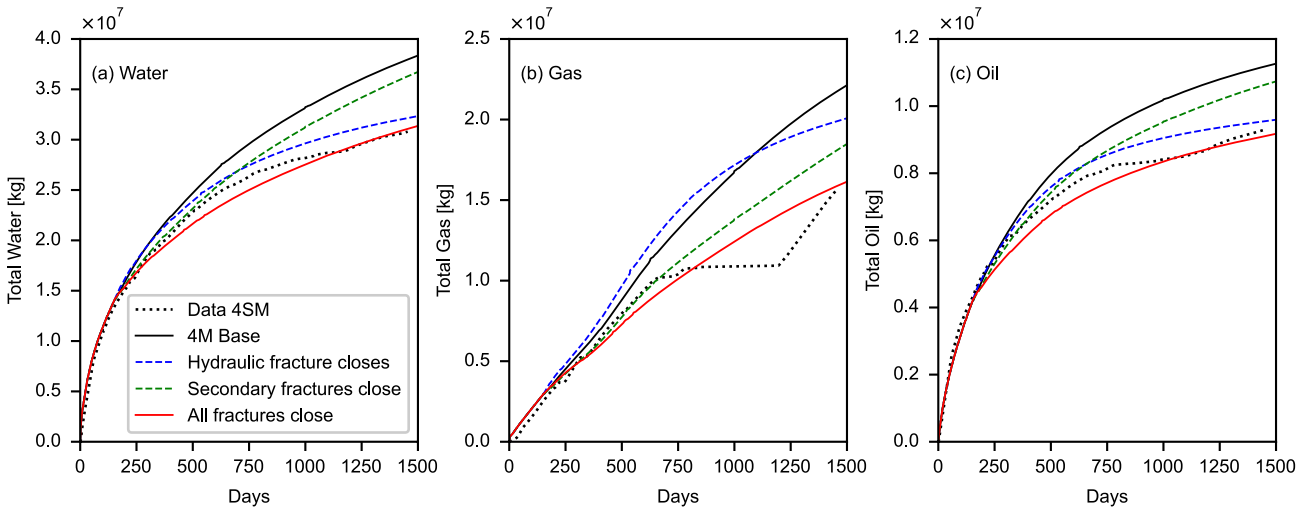

Figure 5.4: Cumulative production of (a) water, (b) gas and (c) oil from well 4SM. At 150 days, the fracture properties are changed from the 4M Base scenario to represent fracture closure.

Moving to the 4SU well, **Figure 5.5** shows cumulative production at well 4SU with and without fracture closure. As with 4SM, production is significantly overestimated if fracture closure is not considered. When all fractures are closed, a good history-match is achieved for the first 800 days of gas production. Water production is overestimated and oil production is underestimated, but the overall model-data agreement is improved compared to the baseline scenario. Closing only the primary fracture increases gas flow rates slightly, until 400-500 days of production. The opposite is observed when closing the secondary fractures, as all production rates show early reductions in rates below the base case, and that are maintained throughout production. Closure of both primary and secondary fractures provide the best overall match to field production behavior.

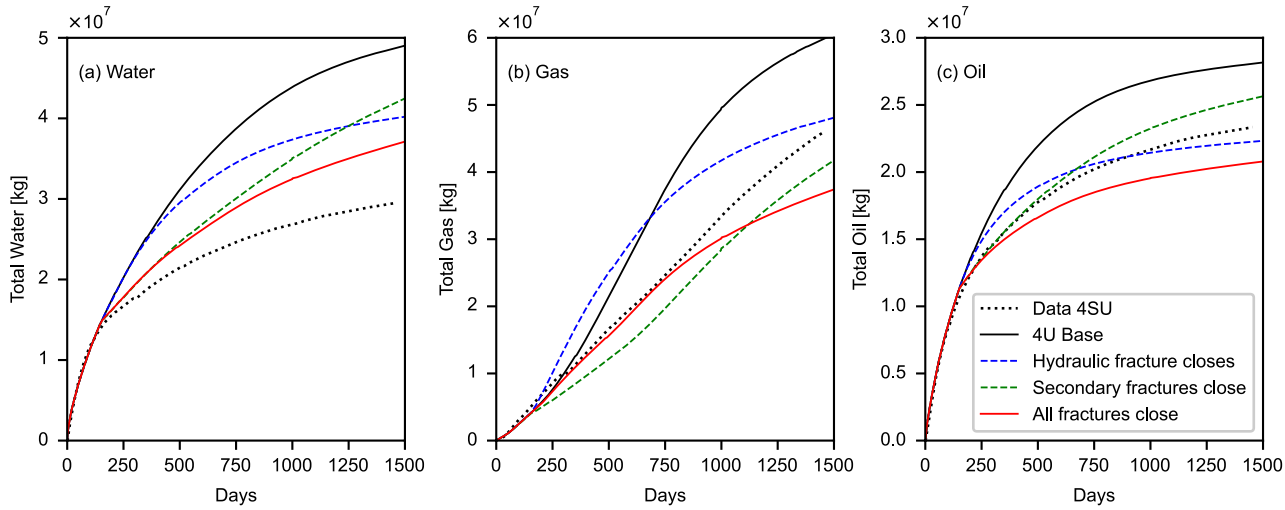

Figure 5.5: Cumulative production of (a) water, (b) gas and (c) oil from well 4SU. At 150 days, the fracture properties are changed from the 4U Base scenario to represent fracture closure.

The Critical Role of Non-Uniform Secondary Fractures:

Figure 5.6 shows a comparison between the proposed secondary fracture model and a uniform DPDP (MINC) model. The uniform model uses a spatially uniform permeability (k_{srv}) for the fractured continuum. This approximation is often adopted to represent a stimulated reservoir volume (SRV) that contains extensive secondary or natural fractures (e.g., Chang & Zhang, 2018; Farah et al. 2019). If SRV permeability is set uniformly to 10 nD (10X the matrix permeability), production of all three phases is significantly underestimated. If the SRV permeability is set to 1000 nD, the water and oil rates are greatly overestimated, but the gas rate remains underestimated. This result emphasizes the importance of applying non-uniform representations of the secondary fractures, such that secondary fracture permeability can promotes depressurization of a larger volume of the near-well matrix, which can increase exsolution of gas. This result supports the existence of the highly conductive zone near the well proposed by Raterman et al. (2019). This result implies that properly characterized, complex, non-uniform multi-scale fracture networks should be considered when modeling fractured shale reservoirs.

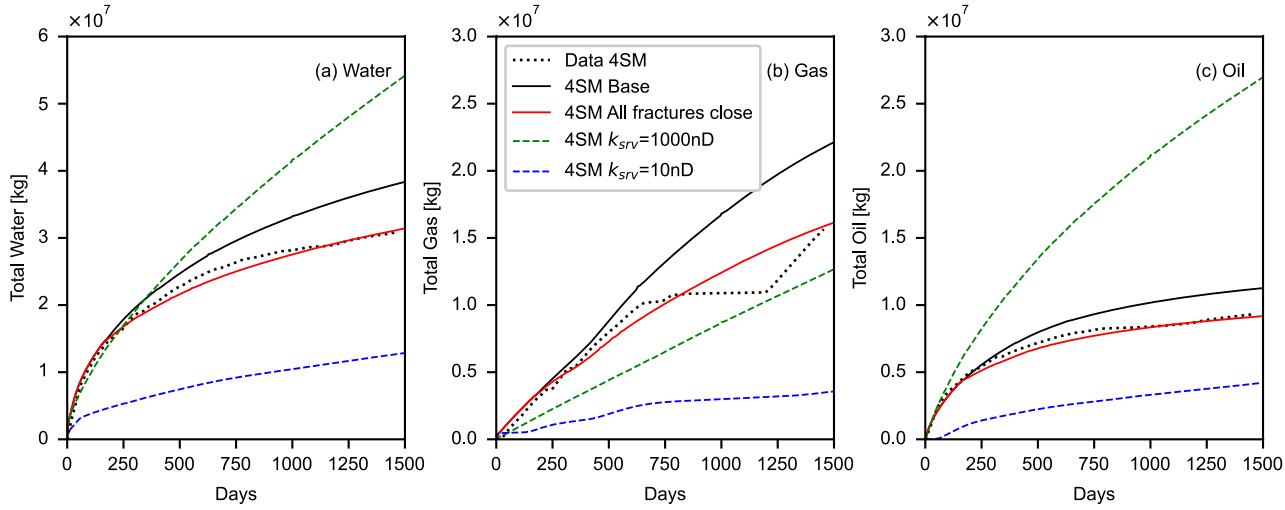

Figure 5.6: Cumulative production of (a) water, (b) gas and (c) oil from well 4SM. Two additional scenarios are plotted, where the secondary fractures are replaced with uniform permeability in the "fracture" of the MINC model.

5.3 Conclusions

History-matching the shale reservoir production data at the Hydraulic Fracturing Test Site (HFTS) is performed with the multi-phase flow simulator, TOUGH+, using reservoir models generated through a coupled workflow with the geomechanical code GEOS. We leveraged the results from geomechanical analysis to develop a new and more detailed representation of hydraulic fractures in production simulations (Sections 2.1 and 4.1). Insights from micromechanical studies (Sections 6.1 and 6.2) drove our investigation of fracture closure as part of the history-matching process. Micro-scale reaction experiments were used to evaluate impacts for geochemical alterations on near-fracture (Section 7.1 and 7.2) and in-fracture (Section 7.3).

We developed procedures to couple GEOS-modeled hydraulic fractures into TOUGH+, which has enabled the simulation of multi-phase flow in fractured reservoirs with irregular fracture geometry and non-uniform aperture fields. We developed a non-uniform secondary fracture model that completes the description of the complex multi-scale fracture network. The proposed fracture network consists of dense and short secondary fractures parallel to the main hydraulic fracture, with permeability decreasing with length, and with a conductive zone that enhances communication between the main and the secondary fractures. The dimension and the permeability of the secondary fractures are used as uncertain parameters during history-matching, and fracture closure is represented by modifying fracture properties.

The proposed reservoir model was tested on two wells at the HFTS site. Inclusion of fracture closure is shown to be critical in history-matching, without which the flow rates of all three phases (water, gas, and oil) are overestimated. Inclusions of non-uniform secondary fractures are also critical in the history-match, as more than 50% of hydrocarbons are produced directly from the secondary fractures. The large near-well permeability of the secondary fractures accelerates pressure drop in the adjacent matrix, which enhances gas production. The short fracture length and the use of a fracture closure mechanism leads to rapid decline of flow rates, which matches the trend of the production data. Even if multi-porosity, multi-permeability models are used to represent SRVs, but with uniform fracture permeability, the gas rate will be strongly underestimated.

6. Micro- and Mesoscale Experiments on Fracture and Proppant Mechanics

The goal of this task is to understand the mechanical behavior of propped fractures and the subsequent effect on fracture permeability. Observations and measurements were made over scales from the single grain interfacing with shale, to sub-monolayers of proppant. Tests were performed under appropriate stresses and conditions for both short and long timeframes. Several test methods were used to gain this understanding of mechanical behavior, and each method had quantitative and observational components (**Table 6.1**). The fundamental emphasis was understanding Wolfcamp shale fracture permeability evolution in both acid-treated (as an analog for an acid spear) and non-treated conditions. Different shales including Eagle Ford, Green River, and Wolfcamp were used in several tests, as delays in receiving and machining Wolfcamp samples occurred due to organizational issues and the COVID-19 pandemic. Often, a technique was refined with non-Wolfcamp shales before Wolfcamp samples were available and prepared. Tests and results are described in subsequent sections below. As described in Section 5, results from these experiments were used in the reservoir-scale production simulations to account for fracture closure and permeability changes.

Table 6.1: Methods for micro-and meso-scale propped fracture tests.

Test	Method	Observation	Permeability	Aperture
Indentation (Section 6.1.1)	1. Increasing/ decreasing force	MicroCT	Inferred	By microCT
Monolayer proppant (Section 6.1.2)	1. Increasing effective stress a. Temperature effect b. Acid spear/ pristine	MicroCT	Computed	By microCT
Sub-monolayer proppant (Section 6.2)	1. Ramp effective stress, long duration constant effective stress 2. Acid spear/pristine	Optical	Measured/ inferred	Measured deformation

6.1 Micro-scale Proppant Mechanics

The mechanical behavior of propped shale was investigated at the micro-scale using indentation tests and fracture closure tests. These tests were performed on confined samples under approximate reservoir conditions with concurrent X-ray micro radiography (single 2-D view) and computed tomography (3-D view). Our methods allowed observation and quantification of proppant crushing and embedment, computation of fracture permeability, and an understanding of the mechanical changes in the shale upon embedment.

6.1.1 Indentation Experiments

Indentation tests examine the deformation of the shale when subjected to a hard spherical indenter, similar to a large grain of sand. Indentation was performed with concurrent radiography and microCT imaging, providing quantification and an understanding of the compaction of shale beneath the indenter by digital volume correlation (DVC). The method can provide the Young's modulus of the shale from the loading/unloading curves. This has several advantages when compared to the conventional Brinell-type of indentation tests run in labs (Voltolini et al., 2021). The new method:

1) works under confined conditions (e.g., the confining pressure of the sample can be chosen). Because the test is run in a triaxial-type of cell, the lateral confinement pressure can be chosen by the operator to match requirements.
2) works in specific environments. This is extremely important when evaluating weathering and/or clay-rich materials, which change mechanical properties depending on the degree of hydration. In our experiments, working in fully hydrated conditions with the sample in water is relatively straightforward.
3) offers 3D-observation of the sample at specific time/loading steps, enabling better evaluation of the mechanical response of the sample (e.g., via DVC).
4) offers a new level of in-situ capabilities, e.g., monitoring creep at constant load, at specific temperatures, as a function of temperature, or coupled with reactive transport to study the effect of weathering (aqueous CO_2 injection, etc.).

In each test, a large number of loading curve data points are collected by interleaving computed tomography providing 3-D images (for the most important events during indentation) and radiography (2-D images). In some cases, *both* the loading and unloading curves were successfully measured (**Figure 6.1**).

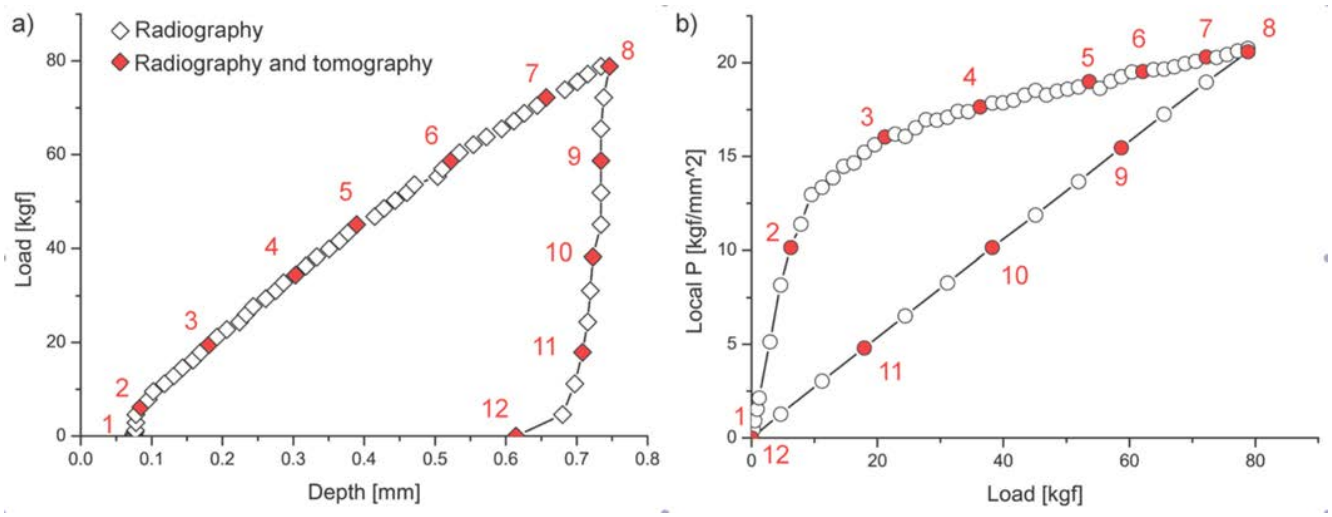

Figure 6.1: a) the compliance curve of an indentation experiment (Green River shale) with white point representing radiographs and red points representing tomographic scans. b) the pressure on the indenter imprint (equivalent to the Meyer's hardness) as a function of the applied load.

From the curves (**Figure 6.1**), we can calculate a reduced Young's modulus E^* = 7.92 GPa. Applying literature values for the Poisson's ratio from a similar shale (Green River with a similar grade obtained via Fischer assay) resulted in a calculated Young's modulus is E = 5.95 GPa, a value well in accordance with bulk values measured on a very similar sample. **Figure 6.2** shows views of the shale from X-ray microtomography before and after loading.

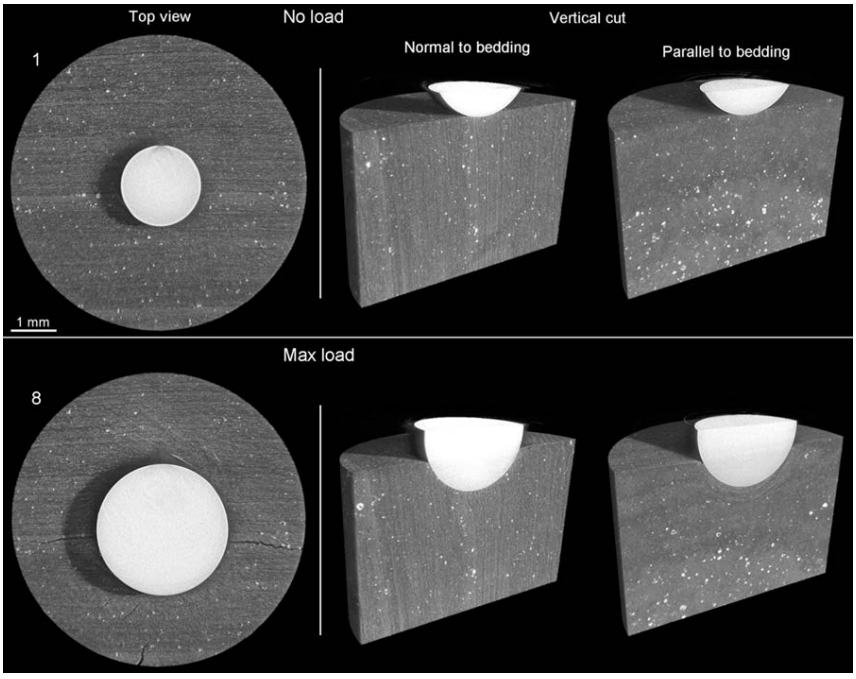

Figure 6.2: Series of volume renderings (Green River shale) showing the sample at zero loading (top row), and maximum load (bottom). From left to right, the volume renderings display the sample as: viewed from the top, virtually cut normal with respect to the bedding, under the indenter tip, and cut parallel to the bedding.

The Green River shale, given the abundance of organics, exhibits a mixed brittle + ductile behavior. DVC was used to characterize the local behavior and the impact of microfabric and composition. Different layers display different behaviors under the indenter tip (**Figure 6.3**). Cracking, generation of shear planes, compaction, and ductile deformation was observed and quantified. Ductile behavior and the role of microfabric/composition are better studied via DVC. Given the geometry of the experiment, it was possible to reduce the system to cylindrical coordinates and use the DVC raw data to calculate two different datasets displaying local strain along the vertical axis (Z), and local radial strain in the XY plane using the indenter tip as the reference axis.

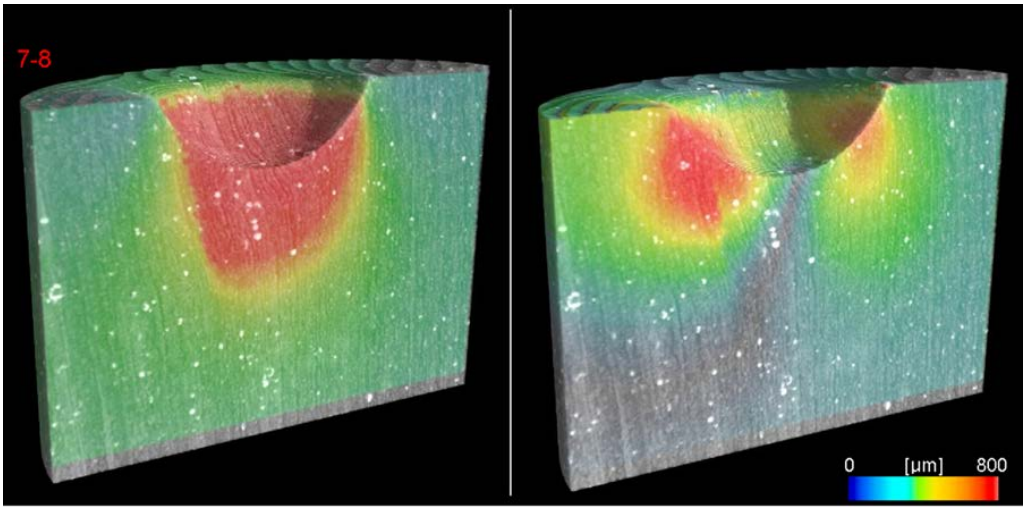

Figure 6.3: Volume renderings of the sample at the end of the loading cycle. The vertical section (normal to the bedding) volume rendering of the sample (in grays) has been overlaid with the cumulative local strain along Z (left) and radial (right), in color scale.

6.1.2 Monolayer Proppant Experiments

The indentation experiments quantify the applied stress in a given probe-shale surface, idealizing the proppant-shale contact. To generalize the observations to a more field-relevant scenario, we carried out forced fracture closure experiments of propped shales examining the effect of temperature, and of acid spear weathering. This adds substantial complications: in these experiments, the "probe" is not a single perfect rigid sphere anymore, but a series of quartz grains. The quartz grains can shatter, and the extent and the geometry of the contacts is not quantified.

In order to calculate how the applied stress is distributed we need to first understand which proppant grains are actually active in propping the fracture (i.e., the grains *mechanically connected to both sides* of the fracture) at any given time and calculate the position and extent to these contacts. Conventional segmentation approaches are not applicable; therefore we developed a first prototype of software tool able to extract this information (among other additional parameters).

Coupling these experiments with meso-scale experiments (Section 6.2) provides a unique series of datasets from the single contact (indentation + microCT imaging), to the few contacts at the microscale (in-situ microCT imaging), to the large number of contacts at the cm scale. This provides a description of the deformation mechanisms at an unprecedented variety of scales, providing fundamental experimental datasets to develop and validate upscaling tools.

Our tests used a custom radiolucent micro-computed tomography coreholder, which allows the application of radial stress *and* axial stress (**Figure 6.4**). The complete experimental matrix to gain a full understanding is quite large (stresses, chemistry, shale type, proppant type, proppant size, temperature, …). Here we consider a limited matrix including shale hardness, bedding orientation, and temperature (plastic embedment in organic-rich shales) for monolayer quartz sand proppant. The experiments are coupled with analysis and modeling techniques to extract morphometric parameters describing the system in a quantitative fashion, data processing techniques such as DVC to describe the local displacements, and Stokes flow modeling to study the impact on fracture permeability and flow patterns.

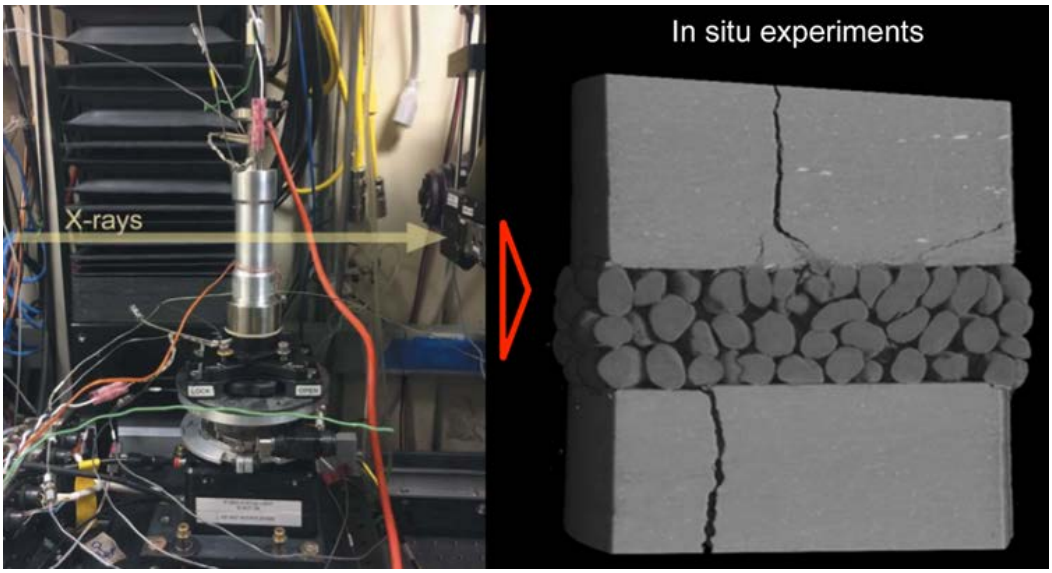

Figure 6.4: Custom radiolucent triaxial holder for µCT. Confining stress is applied to the outer cylindrical surface of the ~0.6 cm diameter sample contained in the holder, and axial stress is imposed using the axial loading piston. This setup enables in situ imaging experiments (right).

The example in **Figure 6.5** shows an Eagle Ford shale sample with two main regions: a calcite-rich (hard and brittle) and a clay-rich (softer and more ductile). The Wolfcamp samples also exhibited this characteristic (see Section 6.2). In **Figure 6.5a**, a cutout of the sample with the initial proppant arrangement is shown, along with the calculated Stokes velocities field (in color). **Figure 6.5b** shows the same sample at the end of the loading sequence. The plot showing the computed evolution of the permeability during the fracture closure cycle with the relevant processes involved at the different stages is presented in **Figure 6.5c**. Similar curves for Wolfcamp shale samples are presented in **Figure 6.12**. During the first stage of loading, proppant rearrangement has a large impact on permeability reduction. As the effective stress increases, proppant breakage occurs, and finally the fracture collapses. The presence of the two shale compositions with different mechanical properties (highlighted in **Figure 6.5**) shows different behaviors. The calcite-rich shale is mechanically stronger than the proppant, causing shattering. In the clay-rich region, the proppant tends to embed in a brittle fashion in the shale (**Figure 6.13).** This is also observed at the cm scale (Section 6.2).

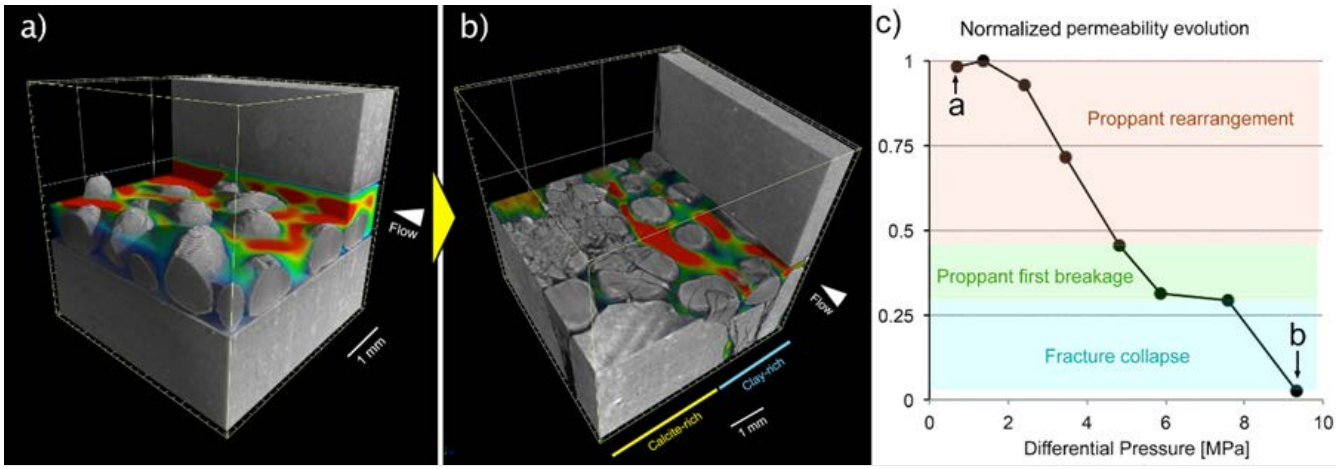

Figure 6.5: µCT images of the initial (a) and final (b) states of the application of increasing axial stress on a confined Eagle Ford sample. Warmer colors indicate more rapid computed flow. The calculated normalized permeability is shown in (c).

Role of temperature:

The presence of large amounts of clays or organic material may induce a more plastic mechanical response in shales that may lead to self-sealing behavior. Plastic behavior depends on *both* temperature and stress. This double dependence makes experiments challenging. In the context of X-ray imaging, heating of oil shales has been studied by a few groups, but always under *unconfined* conditions. These experiments generally highlight a brittle fracturing behavior upon heating. We developed a special in-situ cell for synchrotron X-ray microCT observation with unique capabilities for working at both high pressure *and* temperature (Voltolini et al., 2019).

This test used a 3/8" diameter core of Green River Shale, with a fracture filled with quartz sand proppant **(Figure 6.6**). After applying confining pressure to raise the effective stress, we increased the axial load to induce the closure of the fracture until the first brittle crack in the shale was generated. At that stage, we increased the temperature in steps, and observed a plastic embedment of proppant as a function of temperature. For this specific sample, at temperatures as low as 75 °C a very slow creep occurs, but at 110 °C the creep becomes significantly faster (~10 µm/h). This is very significant since at room temperature (where most laboratory measurements are made) the shale at the same stress conditions was markedly brittle. Mesoscale experiments on Wolfcamp shale were run at about 120 °C (Section 6.2). Results of the experiment with Green River shale are presented in **Figure 6.6**.

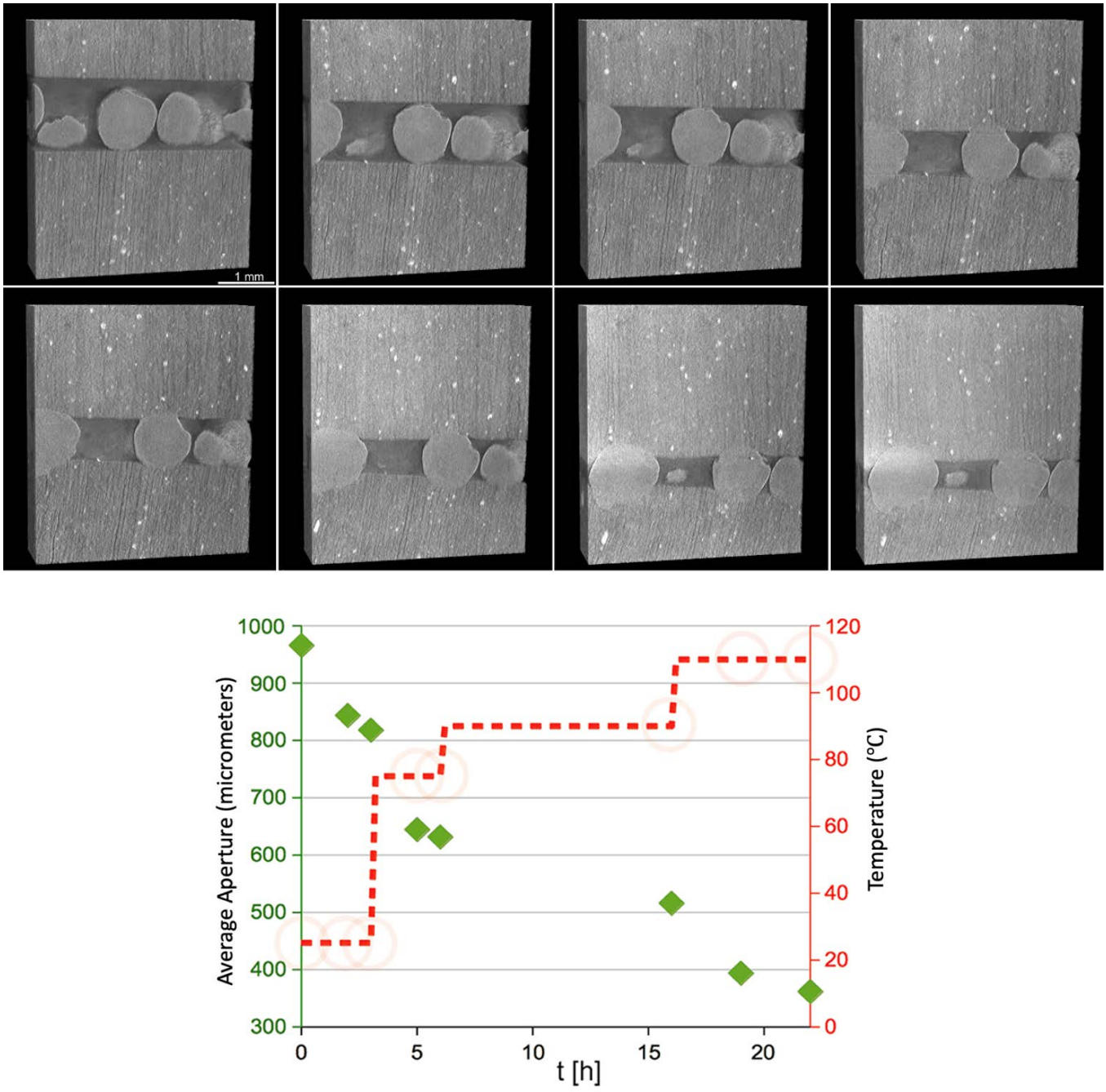

Figure 6.6: Top – tomographic data sets showing fracture closure as temperature increases. Bottom - Applied temperature (red) and aperture (green) of the sample over time. Circles represents tomographic datasets shown above.

Acid treated/pristine shale:

To gain an understanding of the effect of fracture closure at increasing effective stress and the effect of an acid spear on propped fracture behavior in Wolfcamp shale, we performed fracture closure tests on acid-treated and nonacid-treated samples. First, we examined the effect of the acid spear by itself on Wolfcamp shale. The simulated acid spear reaction was carried out on the outer surface of a mini core section used for XRD texture measurement. This was performed to understand the general thickness of the weathered layer and whether the weathered layer thickness is different with respect to the bedding direction. This information is important since

the weathered layer is expected to behave as a weaker layer, therefore the thicker it is, the more a proppant grain could embed in it or develop cracks at the contact.

The acid treatment showed the development of a thin (40-50 µm) layer depleted in carbonates. Despite the anisotropy of the microstructure measured via XRD, the weathered layer thickness was approximately the same thickness in all directions. In this sample, an important textural feature is that most of the carbonates are present as small grains, and the amount of cementing carbonates is smaller, compared to the grains. This would impact the mechanical properties of the weathered layer, as small voids would develop where the carbonate grains are dissolved (**Figure 6.7**). The carbonate grains are not in contact with each other however and do not provide a rigid framework within the material, therefore their dissolution is not expected to significantly decrease the mechanical properties of the material to the extent that weakening a connected framework would do.

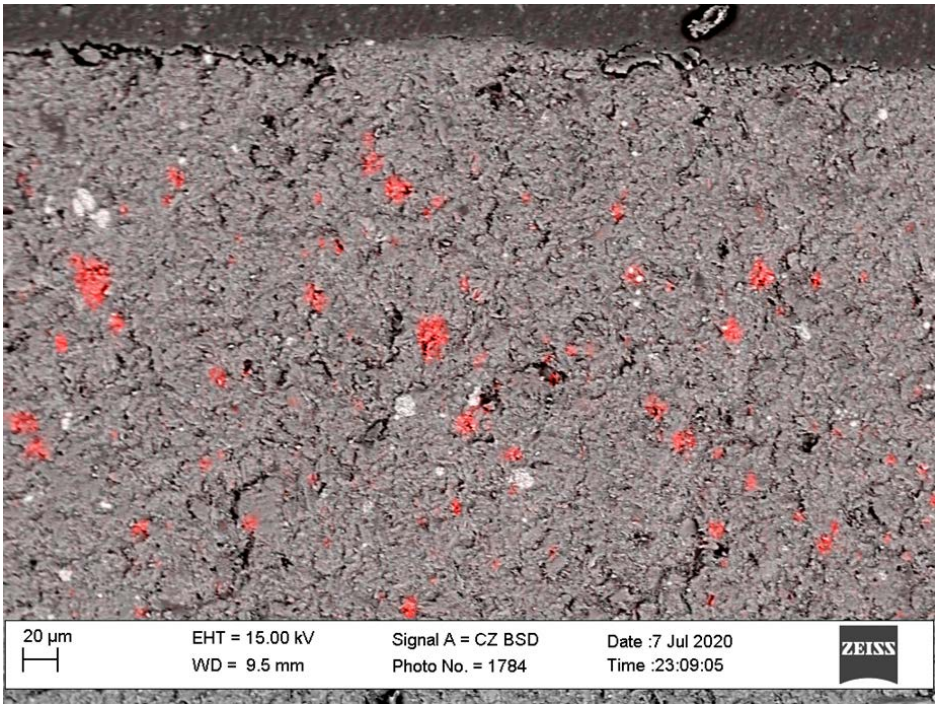

Figure 6.7: Scanning electron micrograph (back-scattered electrons/energy dispersive X-ray spectroscopy -SEM BSE/EDS) image with overlaid map of carbonates (red) in the sample. Orientation of bedding is vertical. Notice the absence of carbonates in proximity with the surface as a result of the acid.

Figure 6.8 shows the proppant layer between untreated (pristine) Wolfcamp shale walls in two different stress states. The color of the grains identifies the stress-bearing grains (red means that a grain is bearing load, either directly or in a chain of contacts), while yellow shows the contact areas of the grains with the shale. The images display how the number of active (i.e., stress-bearing) grains increases with increasing effective stress, as well as the increase in the number and extent of contact areas (embedment).

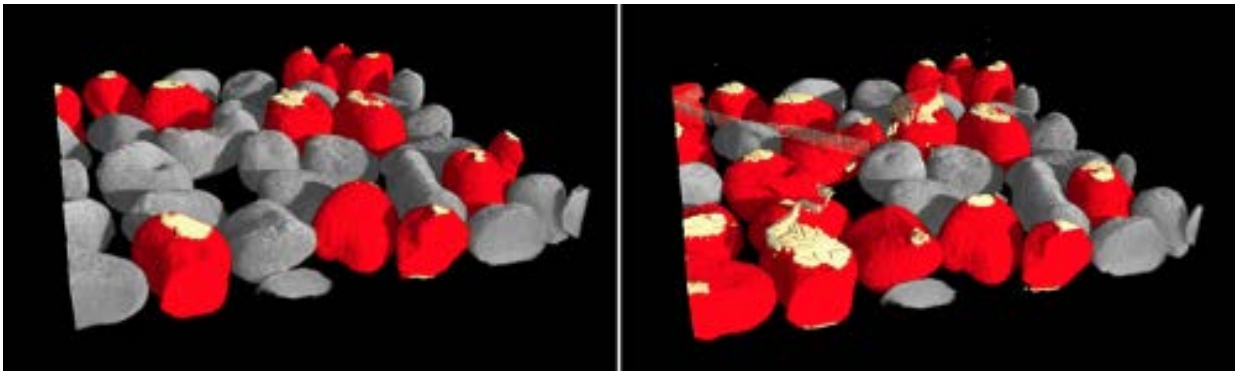

Figure 6.8: Example showing the evolution of the active proppant grains (red) and proppant-shale contact areas (yellow) in the proppant layer between two different stages of the fracture forced closure.

From the known applied forces to the system and the areas of the contacts, we can evaluate how the average stress on the contacts evolves during the fracture closure. The results of this analysis are shown in **Figure 6.9**. In the figure, we plotted the results in terms of normalized stresses, for each sample (pristine vs. acid treated) and by fracture surface (upper vs. lower). The latter separation is important due to the geometry of the experiment: gravity (the fracture is horizontal when setting up) will in part control how the proppant grains are dispersed, and a slightly different behavior is expected due to this. From a practical point of view two main characteristics develop because of this geometry: (1) All grains will be touching the lower surface of the fracture (not important from a micromechanical point of view). (2) Proppant grains will tend to lay their flattest surface to the lower surface of the propped fracture (this would imply an increased ability to spread the applied force). This second characteristic is beautifully identified by the analysis. Blue columns, i.e., contacts with the upper surface, are always higher in stress than the lower section in all the stages of the forced closure. The important result is that in both samples the stress keeps increasing during the closure of the propped fracture, until it reaches a threshold (similar in both samples). Once the threshold is reached, the stress tends to level out. This explains the evolution of the contacts: during the first stage the force applied to the contacts keeps growing, while only limited embedment of the proppant occurs. This is also highlighted by the negligible loss in fracture conductivity at this stage. Once the stress threshold is reached, the embedment of the proppant becomes significant and more active grains appear, further increasing the proppant-shale contact areas, thus distributing the applied force more uniformly. Once this steady-state is reached, any increase in force applied to close the fracture will result in a concomitant specific increase in contact areas (due to embedment, either ductile or brittle) able to keep the average stress on the surfaces constant. In the last two stages of the pristine sample series there's a decrease in the calculated stress due to pervasive fracturing and significant brittle embedment of the grains (very high increase in contact areas).

The acid treatment seems to have very little effect on the stress evolution in the contacts. From a theoretical point of view, with a "softer" surface layer available, the weathered sample should provide a better stress distribution at the early stages of the proppant embedment process. In this test, the thickness of this weathered layer is so small that its role cannot be seen in this specific analysis, since other variables such as proppant geometry, distribution, etc. are much more important.

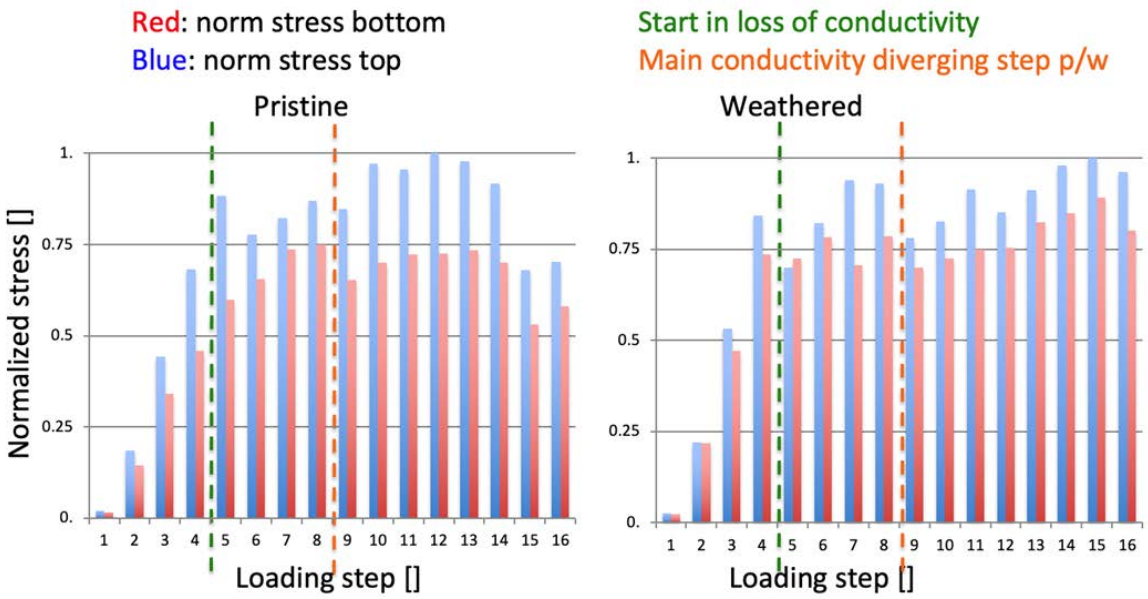

Figure 6.9: The results of the analysis of the stress evolution in the two propped fracture closure sequences (pristine and acid-treated weathered).

To provide additional information for the larger scale experiments using similar Wolfcamp shale samples (with slightly different microstructure and mineral composition), 3D X-ray microCT imaging of the acid-treated Wolfcamp samples was carried out. Two examples are shown in **Figure 6.10 and 6.11**.

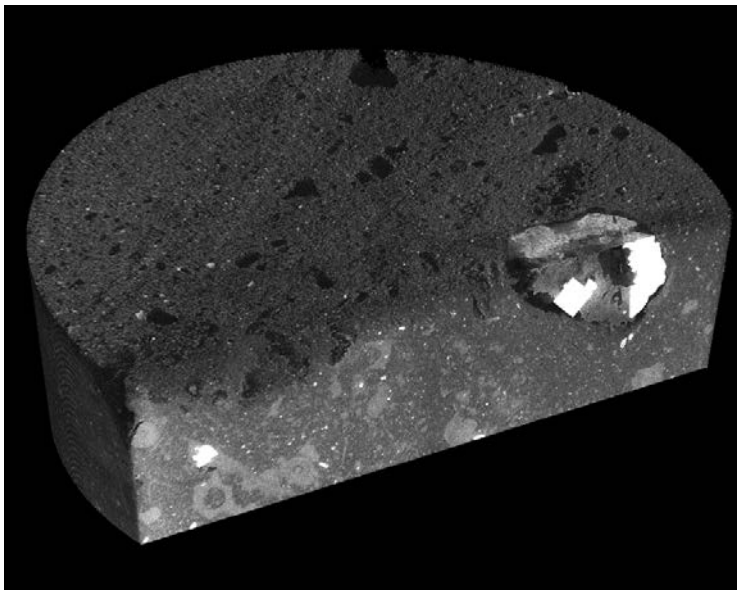

Figure 6.10: MicroCT image of acid-treated calcite-rich sample (field of view ~ 4 mm)

The calcite-rich sample shown in **Figure 6.10** was not considered for microscale experiments because of the scale of the observed heterogeneity - the large bioclasts. In indentation experiments, the probed area would be smaller than those heterogeneities, therefore the measurements would not be meaningful. Still, the sample is meaningful in larger scale experiments, and because of its mineralogical composition and its microstructure, it is

the most prone to develop significant weathering due to the acid treatment. In the acid treatment, large pockets were left by the dissolution of the calcite bioclasts. The large holes were made by calcite and pyrite dissolution. This is especially visible in the largest bioclast in figure, where a large amount of calcite (light gray) was dissolved, but cubes of pyrite (lighter shade in figure) remain in the cavity because of the slower dissolution rate at these conditions.

Figure 6.10 is in strong contrast with the microstructure in more clay-rich shales generated by acid treatment (**Figure 6.11**). We note that the mineral composition is only a part of the equation in developing this weathered layer. The composition is as important as the shale microstructure. A microstructure where calcite grains are large and/or in contact with each other will generate a much thicker weathered layer, since the acid will easily find the reactive material. Once the grains in contact with the fracture surface have been dissolved in a microstructure where small *and* isolated grains of reactive grains are found (**Figure 6.7**), the acid has to be transported through the clayey matrix, making the dissolution process much slower.

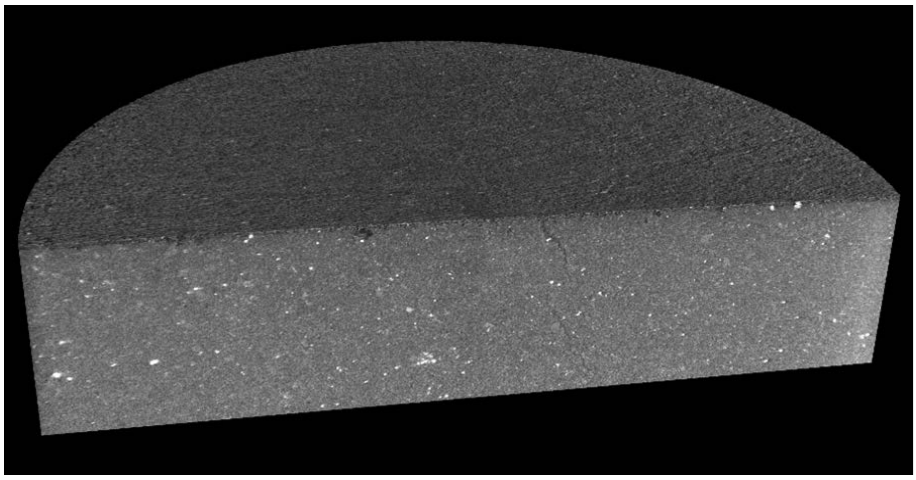

Figure 6.11: MicroCT image of acid-treated clay-rich sample. Note: the weathered layer (darker grey) is on the top of the sample.

In the clay-rich Wolfcamp sample (**Figure 6.11**), the depth of the weathered layer is fairly uniform and much smaller, as well as the size of the cavities left on the surface because the calcite distributed mostly in very small grains embedded in the less reactive matrix.

Figure 6.12 shows microCT images of acid-treated and unreacted shales at the start of the fracture closure experiments. The acid-treatment results in a thin altered layer, visible as a darker grey in **Figure 6.12**. Conductivities of the fracture relative to the initial condition were computed using a Stokes flow code (lower right).

From a practical point of view, we observed that the acid treatment - as investigated - has limited impact in controlling the mechanisms of closure of the fracture (and consequently its hydraulic properties evolution). The mineralogy is very important as shown in **Figure 6.13**, where shattering is more prevalent in the more brittle portions of the sample. There are some differences in behavior between the acid treated and untreated samples, but the effect is small for practical purposes. These tests did not show that the weathered sample distributed the stress significantly better, not affecting the proppant rearrangement significantly (proppant geometry is much more important, for example), proppant shattering is almost identical, and the compliance curve measured with the indentation with X-ray imaging setup only shows a tiny change in curvature at the very beginning of the loading due to the weathered layer.

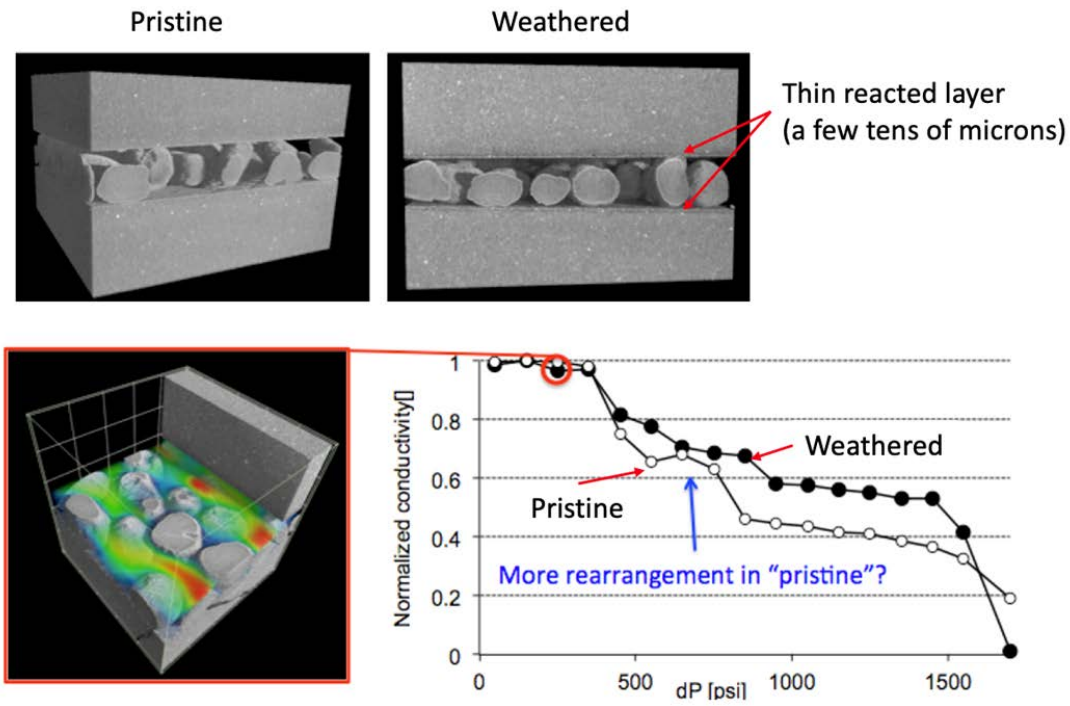

Figure 6.12: Top left, right - images of fracture closure experiments for pristine, and acid-treated shale samples. bottom left. Computed flow through the propped fracture with warmer colors indicating greater flow. bottom right. Normalized fracture conductivity comparison of for the acid treated and pristine samples.

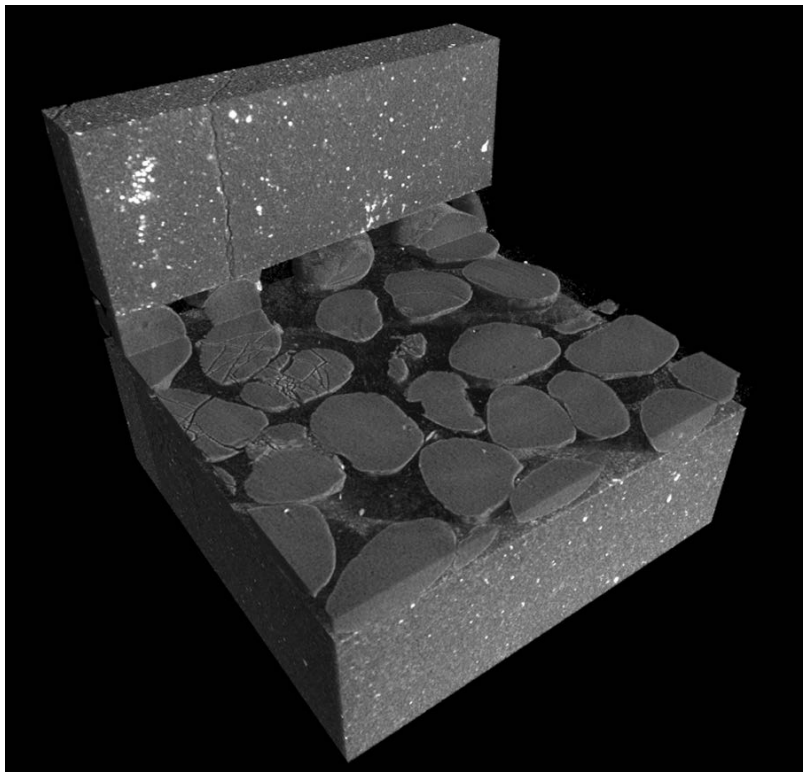

Figure 6.13: Proppant (quartz sand) shattering and fracture development in the shale during loading.

6.2 Mesoscale Studies on the Impact of Acid Treatment on Proppant Crushing and Embedment within a Fracture in Wolfcamp Shale Samples from the HFTS

Section 6.1 examined fracture closure at the micro-scale over a relatively short time scale (hours), investigating the effects of shale mineralogy, temperature, and acid treatment on proppant embedment and crushing. Knowledge of how the shale/proppant systems behave over longer times and larger spatial scales is also needed. The effects of heterogeneity are shown at the micro-scale; these effects are better observed at the meso scale where multiple heterogeneities resulting from shale morphology. Additionally, because oil and gas production occurs over much larger time and spatial scales, investigations moving towards these larger scales are important for extending and interpreting microscale observations. Section 6.2 examines the effect of mineralogy and acid treatment on proppant embedment, crushing, and fracture behavior over a several week time scale and a significantly larger spatial scale than investigated in Section 6.1. The observations from both these sections provide data and useful relationships for interpreting reservoir behavior resulting from fracture closure.

When a hydraulic fracture is poorly supported by sub-monolayer proppant, acid treatment of a brittle, carbonate-rich shale fracture may be able to reduce proppant crushing and fracture closure by making the rock matrix more ductile. To test this hypothesis, a series of mesoscale laboratory fracture closure experiments were conducted on clay-rich and carbonate-rich Wolfcamp shale samples obtained from HFTS reservoir, under elevated stress (effective stress ~27 MPa) and temperature (~122˚C). A specially designed oedometric compaction cell was used, which allowed optical in-situ visualization of the interaction between the sample surface and a sub-monolayer (~50% surface coverage) of quartz proppant grains. Two-week-long loading tests showed some reductions in the fracture compaction and proppant crushing in acid-treated carbonate-rich samples, compared to their untreated counterparts and clay-rich samples. However, for the rather small differences in the mineralogical composition of the samples, the impact of dissolution on the overall proppant and fracture compaction behavior was rather small. However, locally, we observed strong indications that the proppant-shale matrix interaction was altered by the mineral-type-dependent changes of the shale texture.

6.2.1. Introduction

In an unconventional, low-permeability oil and gas reservoir in shale, the use of proppant for preserving the aperture of induced hydraulic fractures is critical for efficient and economical resource extraction. However, particularly in a poorly supported fracture containing a sub-monolayer (less than 100% surface coverage) of proppant in brittle shale, crushing of proppant grains can lead to excessive reductions in the permeability, due to fracture aperture reductions and debris-induced clogging. Such behavior may potentially be manipulated by chemically increasing the ductility of the shale matrix by dissolving hard carbonate grains near the fracture surface. Conversely, increasing the ductility of the shale matrix may also lead to enhanced proppant embedment which can contribute to fracture closure and permeability reduction. In order to investigate the relative importance of proppant crushing and embedment in shale fracture closure, we conducted a series of laboratory experiments investigating time-dependent proppant-shale interaction under effective stress up to 27 MPa and temperature of ~122 °C. The key objectives of the experiments are (1) to determine the time-dependent compaction behavior of propped fractures for shale samples with different mineral compositions, and (2) to examine the effect of acid treatment on the ductility of the shale matrix and proppant crushing. These experiments were conducted using a custom-built oedometric cell with a high-pressure viewing window which allowed real-time visualization of fracture closure and proppant deformation and embedment. The visualization was facilitated by the UV fluorescence of injected pore fluid (Nakagawa and Borglin, 2019). The samples used in the experiments were clay-rich and carbonate-rich Wolfcamp shale samples from the HFTS. Below, we first present sample properties and experimental setups, followed by experimental results including fracture images and the concurrently obtained mechanical (fracture closure) and hydrological (flow resistance) data. We also examine the correlation between the shale mineralogy and the local crushing of proppant grains.

6.2.2. Experimental Setup

Shale Samples:

We selected three core sections of Wolfcamp shale from the HFTS reservoir which had very different mineralogical compositions (**Figure 6.14**). X-ray diffraction analysis using powered samples was performed. Core section 11P (HFTS-11P) consisted of visually homogeneous shale, containing ~37% clay. In contrast, Section 3P (HFTS-3P) contained ~25% carbonates and about 50% less clay than 11P. Also, this sample was highly heterogeneous, with clearly visible clay-rich, carbonate-rich (where some micro fossils are visible), and mixed pyrite and carbonate-rich layers. The lithics content of the sections were nearly identical (55–56%). In contrast, Section 16P had a similar abundance of carbonates as Section 11P, while with more clays and less lithics (by ~10%). Also note that 3P is rich in calcite, but dolomites dominate in 16P. The ratio between the swelling (illite-smectite) vs. non-swelling (illite) clay contents was similar for all three sections.

From each of the three core sections, two thin disc-shaped samples (diameter=44.4 mm, thickness=6.4 mm) were produced, with less than a ~3 mm of separation from each other. This was to minimize the differences in the sample properties due to the core-scale heterogeneity. The discs were cut so that the flat surfaces were perpendicular to the bedding plane. They were stabilized in stainless steel rings with epoxy (**Figure 6.15**).

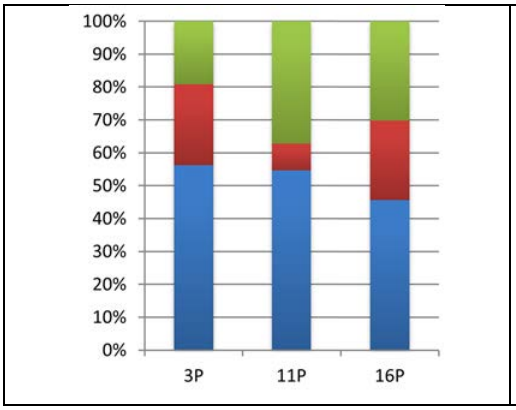

	3P	11P	16P
Quartz	47.6	42.8	37.4
Plagioclase (Albitic)	7.1	9.5	6.8
Pyrite	1.6	2.4	1.5
Calcite	16.5	0.6	6.2
Dolomite	3.3	2.2	6.9
Ankerite/Ferroan Dolomite	4.7	5.3	11
Illite	11.6	24.4	19.6
Illite/Smectite	7.6	12.8	10.6

Figure 6.14: Mineralogical compositions of two types of Wolfcamp shale used in the experiment. Samples 3P (HFTS-3P) and 16P (HFTS-16P) have similar, relatively high carbonate contents (~25%). In contrast, sample 11P (HFTS-11P) contains a large percentage of clay (~37%) with little carbonate. Samples 3P and 11P have roughly the same abundance of lithics (55–56%).

a. Clay-rich sample (11Pa)	b. Heterogeneous carbonate-rich sample (3Pb)	c. Homogeneous carbonate-rich sample (16Pb)

Figure 6.15: Wolfcamp shale discs (diameter=44.4 mm, thickness=6.4 mm) used in the experiment. Clay-rich HFTS-11Pa and 11Pb samples and carbonate-rich HFTS16a and 16b samples had a visibly smooth and homogenous texture. In contrast, carbonate-rich HFTS-3Pa and 3Pb samples exhibited heterogeneous layers.

Fluid Chemistry and Acid Treatment:

The experiment used synthetic brine with a chemical composition based upon that of diluted, produced fluid from the reservoir. The most prominent ions were Na^{+}, followed by Ca^{2+} and Mg^{2+}. The actual recipe for the fluid used in the experiment is shown in **Table 6.2**.

Table 6.2. Chemical composition of the fluid used in the experiment.

Chemicals	g/L	Chemicals	g/L
$CaCl_2 \cdot 2H_2O$	3.48	H_3BO_3	0.0125
LiCl	0.0489	NaBr	0.322
$2MgCl_2 \cdot 3H_2O$	1.67	NaCl	46.2
KCl	0.572	NaI	0.0473
$2SrCl_2 \cdot 3H_2O$	0.548	Na_2SO_4	0.592
$NaHCO_3$	0.689	H_2O	balance

Although the HFTS field experiment did not necessarily use acid during stimulation, we were interested in its impact on fracture closure. The surfaces of the samples HFTS-3Pb, 11Pb, and 16Pb were exposed to HCl to dissolve carbonate minerals so that the fracture closure for these samples could be compared to untreated counterparts (**Figure 6.16**). The acid treatment was conducted using the following steps:

- Prepare 15% HCl solution at room temperature
- Pool a thin layer of the acid in a Petri dish. Place small plastic stands to support the sample
- Emplace the sample face down over 2 minutes and remove the CO_2 bubbles
- Repeat the leaching 4 times. Then rinse and remove excess water

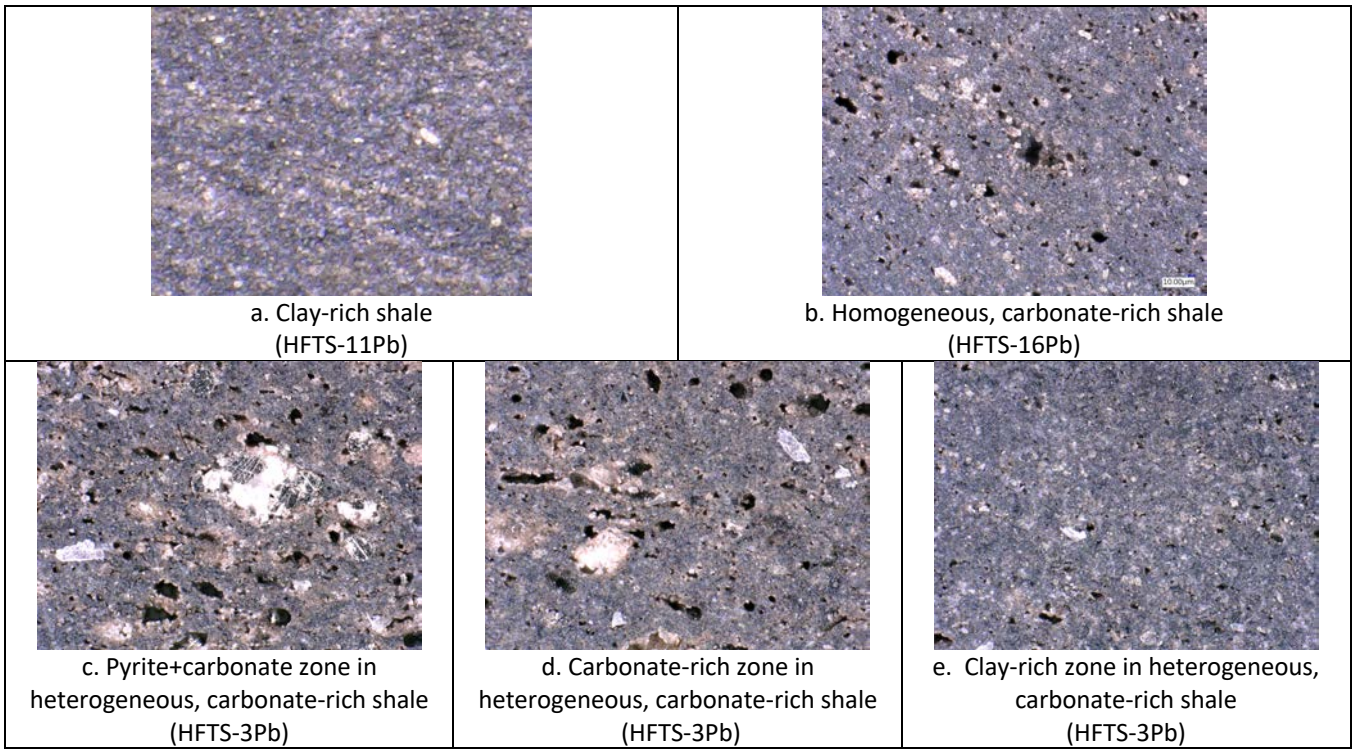

a. Clay-rich shale (HFTS-11Pb)

b. Homogeneous, carbonate-rich shale (HFTS-16Pb)

c. Pyrite+carbonate zone in heterogeneous, carbonate-rich shale (HFTS-3Pb)

d. Carbonate-rich zone in heterogeneous, carbonate-rich shale (HFTS-3Pb)

e. Clay-rich zone in heterogeneous, carbonate-rich shale (HFTS-3Pb)

Figure 6.16: Images of microscopic regions of the acid-treated sample surfaces. The height of the images is 500 µm. Compared to the clay-rich 11Pb (a) and the clay-rich zone in 3Pb (e), pyrite and carbonate-rich zones of 3Pb (c and d, respectively) exhibit a strong impact of dissolution by acid. Note that the pyrite-rich layer also contains a large amount of carbonate mineral grains. Pyrite itself showed little dissolution. Sample 16Pb shows less dissolution than 3Pb.

Experimental System:

We used a specially designed oedometric cell which allows real-time, in-situ visualization of the changes occurring to a shale surface and proppant grains under elevated stress (and pressure) and temperature. Similar proppant compaction experiments by others have used standard "conductivity cell" (Zhang et al., 2014) and modified triaxial test cells (Alramahi & Sundberg, 2012). For these experiments, however, real-time observation of the fracture and proppant is difficult. Improving our previous experiments involving an aluminum test cell (Nakagawa & Borglin, 2019), the new test cell was built of Hastelloy C276, so that it can be used for experiments involving corrosive brine, higher temperature (up to 150 ˚C) and compaction stress (up to 41 MPa).

During an experiment, the shale disc with a retaining ring (**Figure 6.15**) was pressed against a sapphire window, mediated by a layer of proppant (**Figure 6.17**). The gap between the shale core and the window is envisioned as a "(half-) fracture" allowing mechanical deformation and fluid flow. The proppant used in the experiment was round, quartz sand. The grain size (approximate diameter from the sieve mesh size) was in the range of 1.0–1.5 mm. Although this is rather large compared to the grain sizes used in the field, we selected this size to facilitate visualization. All the experiments reported here used a randomly deposited sub-monolayer of the proppant which covered approximately 50% of the sample surface. To avoid premature fracturing of the proppant grains from the contact between the grains and a hard, sapphire disc surface, a semi-rigid FEP film with a thickness of 125 µm was placed to reduce the stress concentration. Also, a specially designed o-ring was used at the edge of the shale discs, which allowed approximately one-dimensional fracture-parallel fluid flow.

For fracture imaging, we employed a fluorescence imaging technique which we used previously (Nakagawa & Borglin, 2019). With external illumination, it is difficult to view through the window into the dark interior of the cell. The fluorescence imaging solves this problem by illuminating the cell from within, and also by reducing reflection of the light at the exterior window surface. We used 0.1 wt% green, liquid UV-fluorescent dye (WATER-GLO® 802-P, Spectroline) mixed with the brine. Using a ring-shaped UV lamp, UV light is first introduced in the test cell through the sapphire window (**Figure 6.18**). The dye-bearing brine in the fracture responds to the UV and emits green fluorescent light, with intensity approximately proportional to the thickness of the fluid layer. The exiting light then was captured using a CCD camera positioned above the pressure vessel. A long guide tube (stand-off tube) was used to keep the camera away from the hot window surface so that the optical parts and the electronic components were not damaged during long-duration experiments. The overall test system diagram including the pressure, flow, temperature control, and image capture systems are shown in **Figure 6.19**.

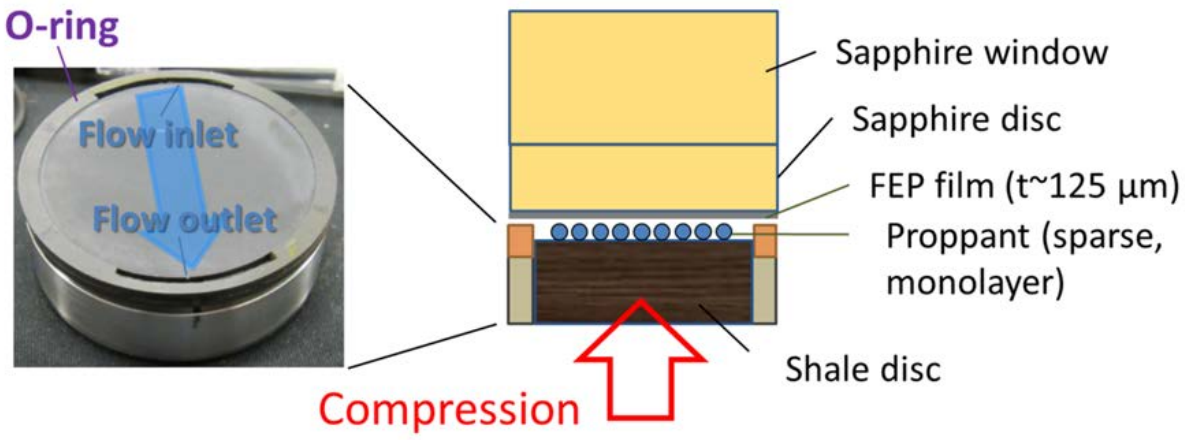

Figure 6.17: A schematic view of a propped shale fracture under compression. The top half of the fracture is replaced by transparent sapphire blocks for in-situ visualization.

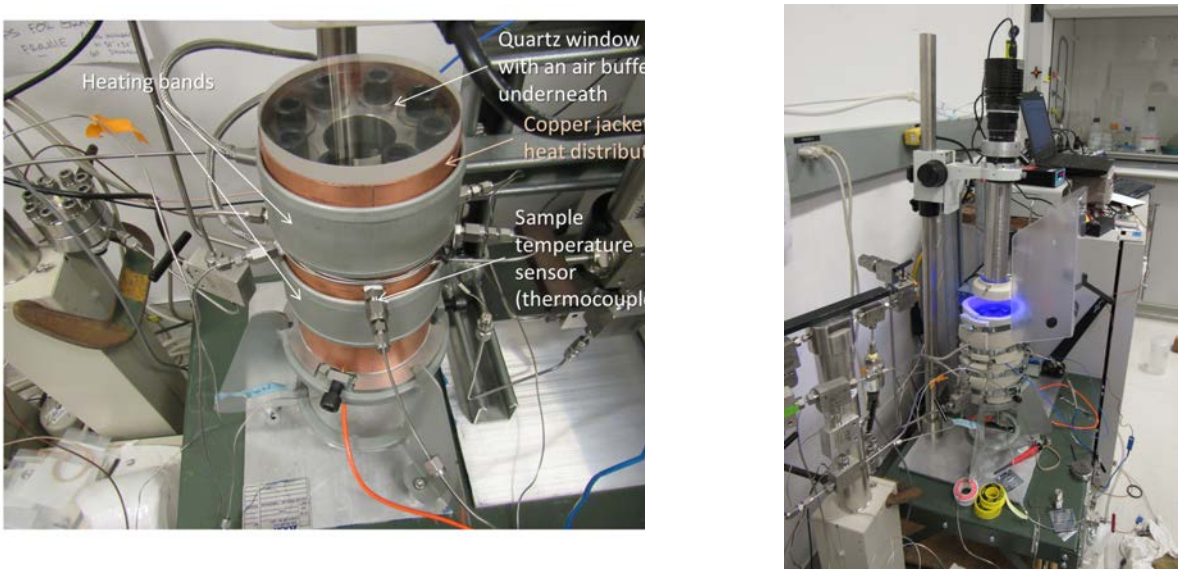

Figure 6.18: UV fluorescence assisted, in-situ optical visualization of a shale(-glass) fracture within a pressure vessel under elevated temperature and stress/pressure. Left: Test cell with thermal jackets and plumbing (thermal insulation is removed in the image). Right: b. Experiment in progress with UV illumination for fluorescence imaging.

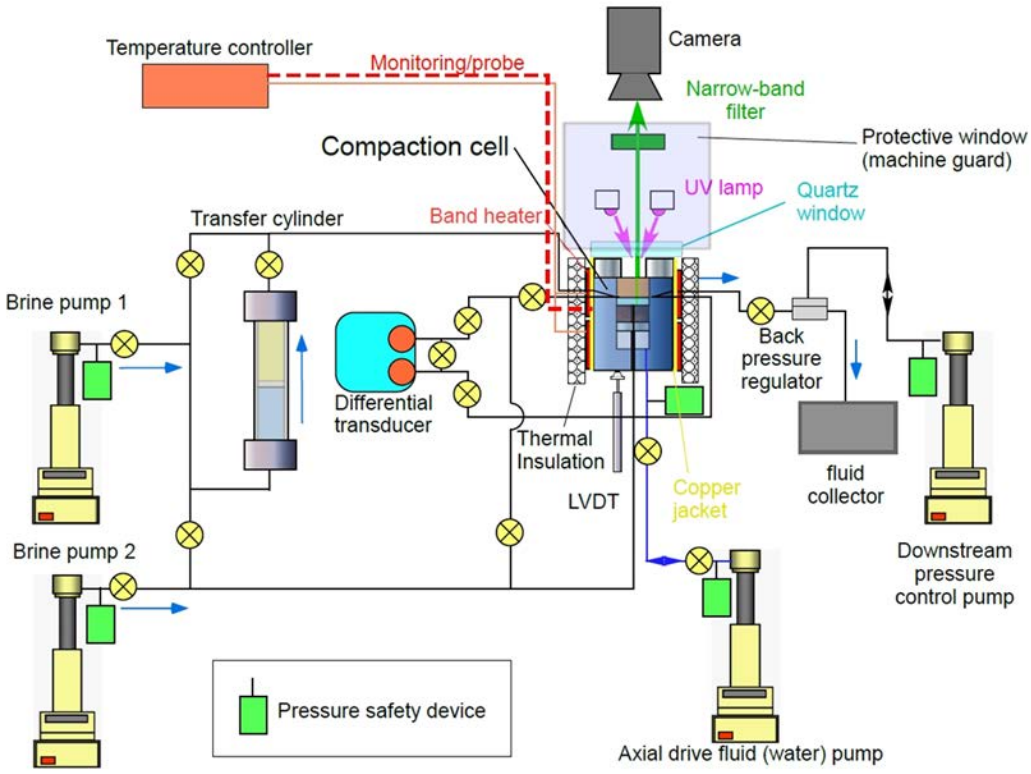

Figure 6.19: Overall test system diagram.

Experimental Procedure:

We conducted the experiment based upon the following general protocols. During the initial preparation state, the shale sample was introduced into the test cell, and a layer of proppant was deposited. At this stage, a small

Viton disc (or multiple discs) was embedded among the proppant grains. This was later used to determine the true aperture of the fracture from obtained images. Next, the system was flooded with the synthetic brine containing fluorescent dye, then the pore pressure was raised to 10.3 MPa and held constant over 72 hours. Once this step was completed, the system temperature was raised to 120 °C (the actual cell temperature was ~122 ± 1°C) overnight, then the loading test was started. The loading was conducted by increasing the effective stress on the fracture by steps up to the maximum target stress of 27 MPa in 1 hour. At each step, the displacement of the internal piston, pressure drop across the surface of the fracture for a constant flow rate of 1 mL/minute, and the image of the fracture and proppant via UV-induced fluorescence were recorded (Note that the displacement and pressures were recorded continuously). Once the target stress was reached, the stress was held constant, and the displacement, flow resistance, and the fracture/proppant images were recorded at discrete intervals over 2 weeks. At the end of the 2 weeks, the effective stress was reduced by reversing the steps taken during loading. After the loading test, the sample was taken out of the test cell, photographed, and the debris on the surface was rinsed off for detailed examination under a microscope. The above test procedures were repeated on the six samples to examine the differences in their behavior during both initial short-term loading test and the 2-week-long creep test (**Table 6.3**).

Table 6.3: Test runs.

Test	Sample	Minerals	Texture	Acid treatment
1	HFTS-3Pa	Carbonate rich	Heterogeneous	No
2	HFTS-3Pb	Carbonate rich	Heterogeneous	Yes
3	HFTS-11Pa	Clay rich	Homogeneous	No
4	HFTS-11Pb	Clay rich	Homogeneous	Yes
5	HFTS-16Pa	Carbonate rich	Homogeneous	No
6	HFTS-16Pb	Carbonate rich	Homogeneous	Yes

6.2.3. Results and Discussion

Fracture Deformation and Flow Resistance Changes:

Time-lapse fluorescence images for each sample are shown in Figure 6.20 for the initial unloaded state at the beginning of the long-term test at the maximum effective stress, and at the end of the 2-week-long tests. The brightness of the images qualitatively shows the relative aperture of the fracture (brighter areas have wider apertures). Note that the initial image of the 3Pb sample is darker compared to the rest, because the sample was loaded prematurely during the setting up stage up to about 3 MPa.

Surprisingly, even for samples with relatively high clay content, proppant grains exhibited severe crushing under the applied stress. This may indicate that the clay content of these samples (up to 37%) was still not sufficient for making the clay particles load bearing (instead, they may be filling the space between harder carbonate and lithic mineral grains). Although small cracks are difficult to see in these small images, generally, darker grains are uncrushed and still load bearing. In contrast, lighter grains are fragmented and contain fluid in the cracks. Most of the proppant crushing occurred during the initial loading, but close examination of the images during the long-term loading revealed that the grain crushing continued throughout the duration of the experiment.
In principle the fracture aperture changes can be determined quantitatively from the intensity changes of the fluorescence images. However, we have learned that the reflections and shadows, clouding of the fluid, and time-dependent thermal degradation of the fluorescence dye make calibration of the relationships between the light intensity and the fluid thickness difficult (Although, the fluid was replaced immediately before each imaging to reduce the effect of fluid clouding and thermal degradation). Unfortunately, measurements using a displacement sensor (LVDT) are also affected by the compliance of the system particularly during loading and unloading stages. In order to obtain “true” fracture aperture measurements during the loading stage, we used fluorescence images of the aforementioned Viton rubber discs.

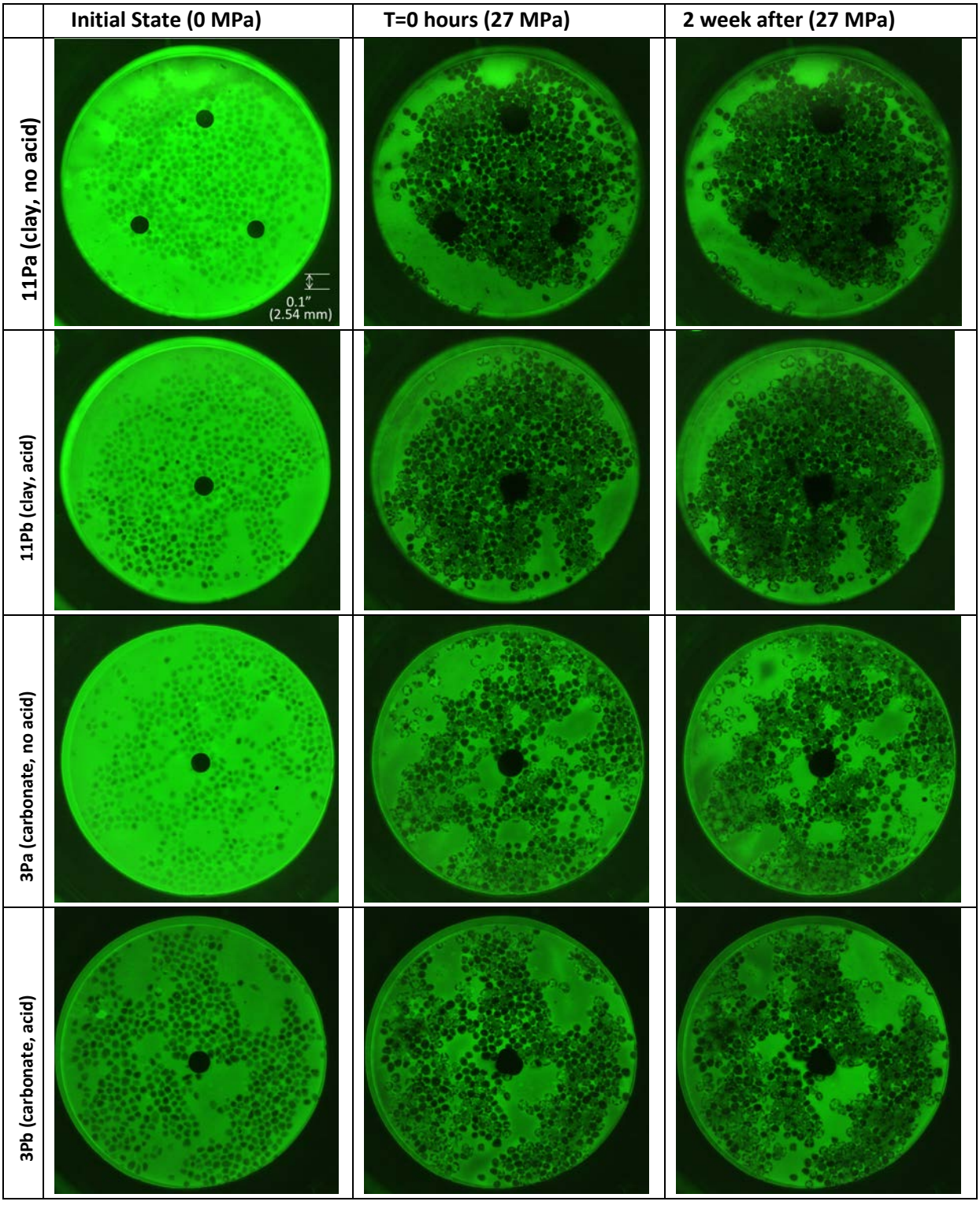

Figure 6.20: Fluorescence optical images of fracture closure/proppant changes. From the initial state (left column) to the beginning of the time-lapse compaction at the highest effective stress (middle column) to the 2-week point of the experiment under sustained effective stress on the proppant and the fracture (right column). Circular black dots in the images are Viton discs which are used to determine the fracture aperture. Note that the initial image for 3Pb sample is darker—indicating a smaller fracture aperture—because the sample was accidentally loaded prematurely before the experiment was started.

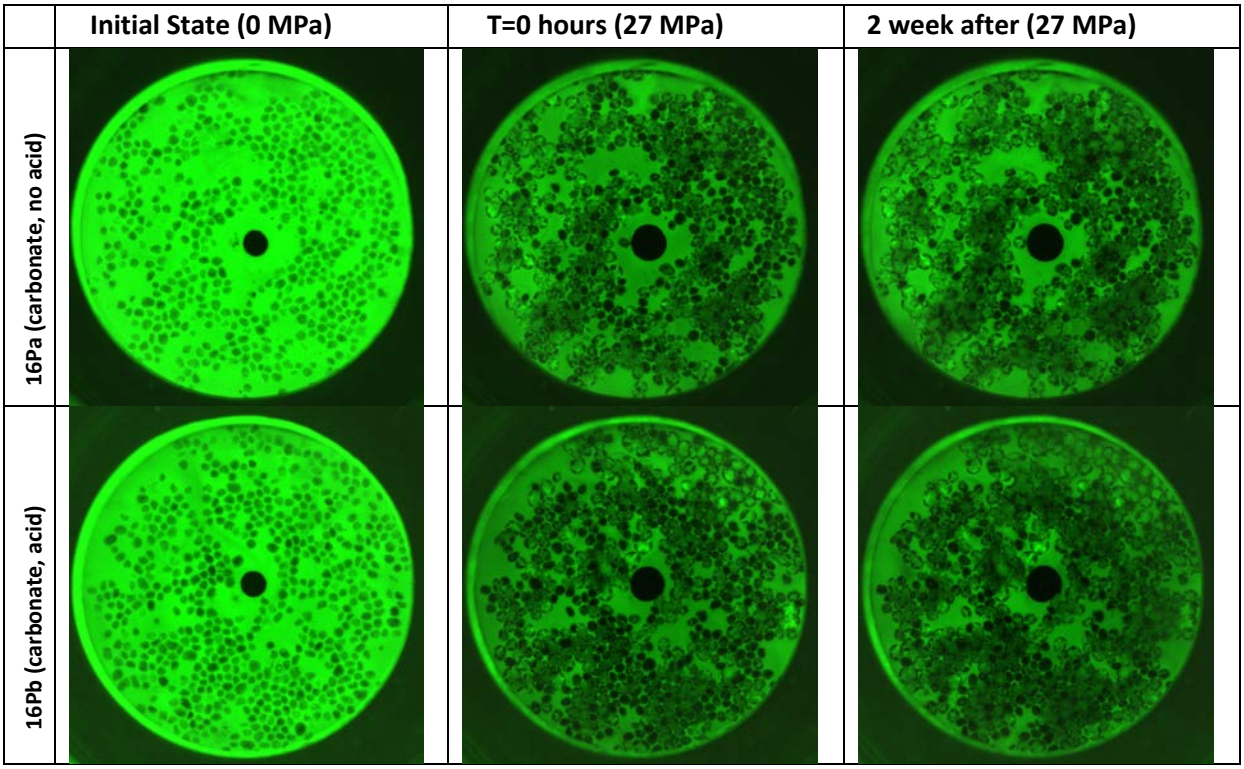

Figure 6.20: (Continued)

The aperture changes of the samples during the initial loading are shown in **Figure 6.21**, which were measured using both an LVDT and Viton dot images. Note that the LVDT data are referenced to the direct, image-based measurements at the highest effective stress. As the plots indicate, LVDT-based measurements (open symbols with broken lines) generally overestimate the deformation, compared to the image-based measurements (closed symbols with solid lines). For all the samples, a large part of the deformation is attributed to proppant crushing. However, the clay-rich 11Pa and 11Pb samples clearly exhibit larger aperture reductions compared to carbonate-rich samples, which can be attributed to both higher elastic compliance and plastic deformation of the clay minerals. As seen in Section 6.1, the short-term results presented in **Figure 6.21** do not show a clear indication of the impact of acid treatment, which was anticipated especially for the carbonate-rich samples because of the acid-induced dissolution and increased matrix porosity. However, in **Figure 6.22a**, although subtle, the long-term test shows some differences. Note that the symbols and legends used in this plot is the same as **Figure 6.21**. Carbonate-rich and acid-treated 3Pb samples exhibited markedly reduced compaction compared to the untreated 3Pa sample. Interestingly, the clay-rich 11Pa and 11Pb samples also show differences in the compaction behavior. However, considering the little impact of the acid treatment in changing the surface texture of the sample, we think this was due to other causes such as heterogeneity of the sample. Homogenous, carbonate-(dolomite) rich samples showed nearly identical behavior. The difference between the 3Pa and 3Pb samples appears to have occurred during the early period (first ~10 hours) of the long-term test. In **Figure 6.22b**, measured changes in the flow resistance for the fractures are also presented, but, because of the large overall apertures propped by the large proppant grain size, the resistance was too small to be accurately determined.

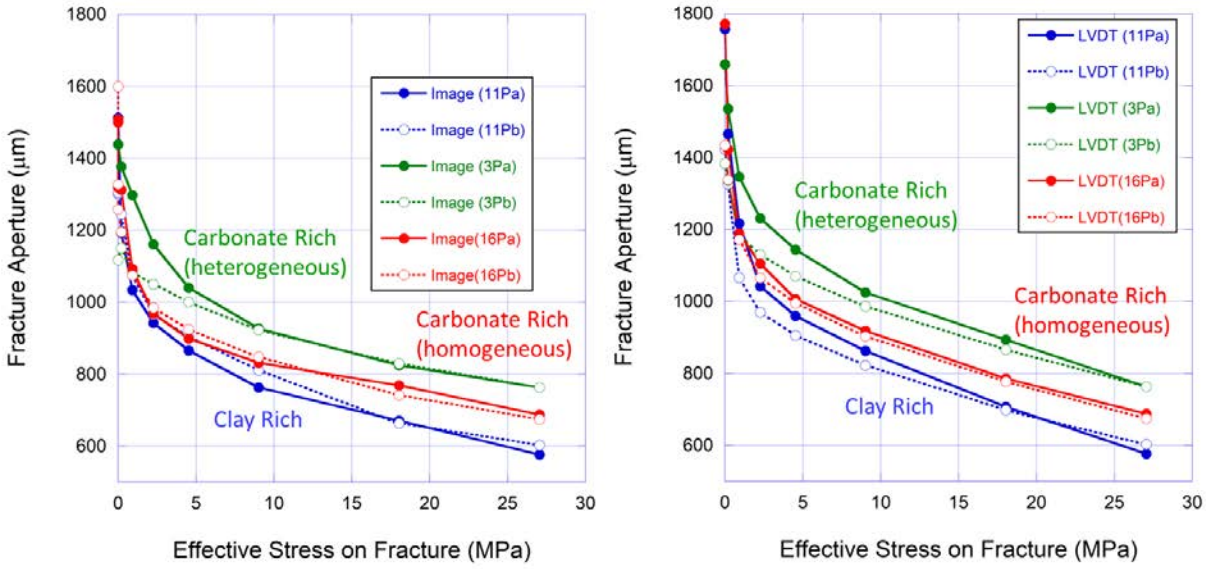

a. Image-based measurements b. LVDT-based measurements

Figure 6.21: Direct fracture aperture measurement using the deformation of a Viton dot on the fracture, determined from the optical images as shown in **Figure 6.20**. For comparison, measurements using LVDT (referenced at the maximum effective stress at 27 MPa) are also shown in broken lines. Because LVDT measurements include deformation of the entire test system (test cell wall, view window, sample-vessel interfaces), they overestimate the aperture changes. Clay-rich samples show more deformation than carbonate-rich samples. Acid treatment seemed to have little impact on this short-term deformation behavior (duration ~1 hour).

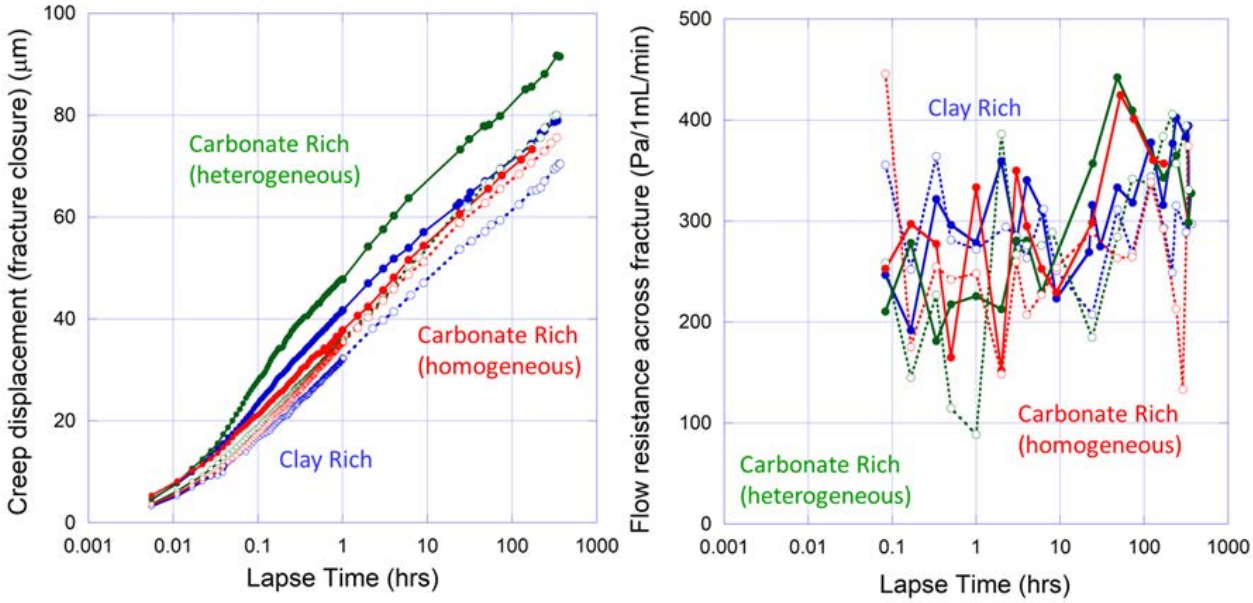

a. Creep compaction of a fracture b. Fracture-parallel flow resistance

Figure 6.22: Long-term measurements of (additional) fracture closure (a) and flow resistance (b) from the start of the creep test (0 hour). The solid circles indicate untreated samples, and the open circles are acid-treated samples. Although the flow measurement is quite noisy, there is a general trend indicating gradual decreases in the fracture permeability. For heterogeneous, carbonate-rich samples, the untreated 3Pa sample shows higher compaction than the acid-treated 3Pb during the first ~10 hours of the test. Interestingly, carbonate-rich samples exhibited faster rates of compaction compared to clay-rich samples.

Similar to what we observed in our previous experiments (Nakagawa and Borglin, 2019), the compaction generally increased semi-logarithmically with time, which is frequently observed for a variety of healing and time-dependent behavior of geological materials (Snieder et al., 2016). The relationships in **Figure 6.2.9a** show that the rate of fracture closure was, counterintuitively, faster for heterogeneous and carbonate-rich, therefore more brittle samples, compared to more ductile, clay-rich samples.

Correlation Between Proppant Behavior and Shale Mineralogy:

In order to understand the proppant-shale interactions and the resulting fracture compaction in the experiment better using the time-lapse images of the proppant grains, we examined the statistics of proppant grain crushing (or survival) correlated with the shale mineralogy. **Figure 6.23** shows photographs of the proppant craters (casts) on the sample surfaces. From these images and the images in **Figure 6.20**, it can be seen that the proppant grains on the fracture were more or less evenly distributed during the tests. Using these images, we identify and count the total number of proppant grains and the number of intact grains which are free of clearly visible cracks and are not pulverized. Using these numbers, we define the following quantitative parameter (Proppant Survivability Index, PSI) which can be related to the ductility (or brittleness) of the shale:

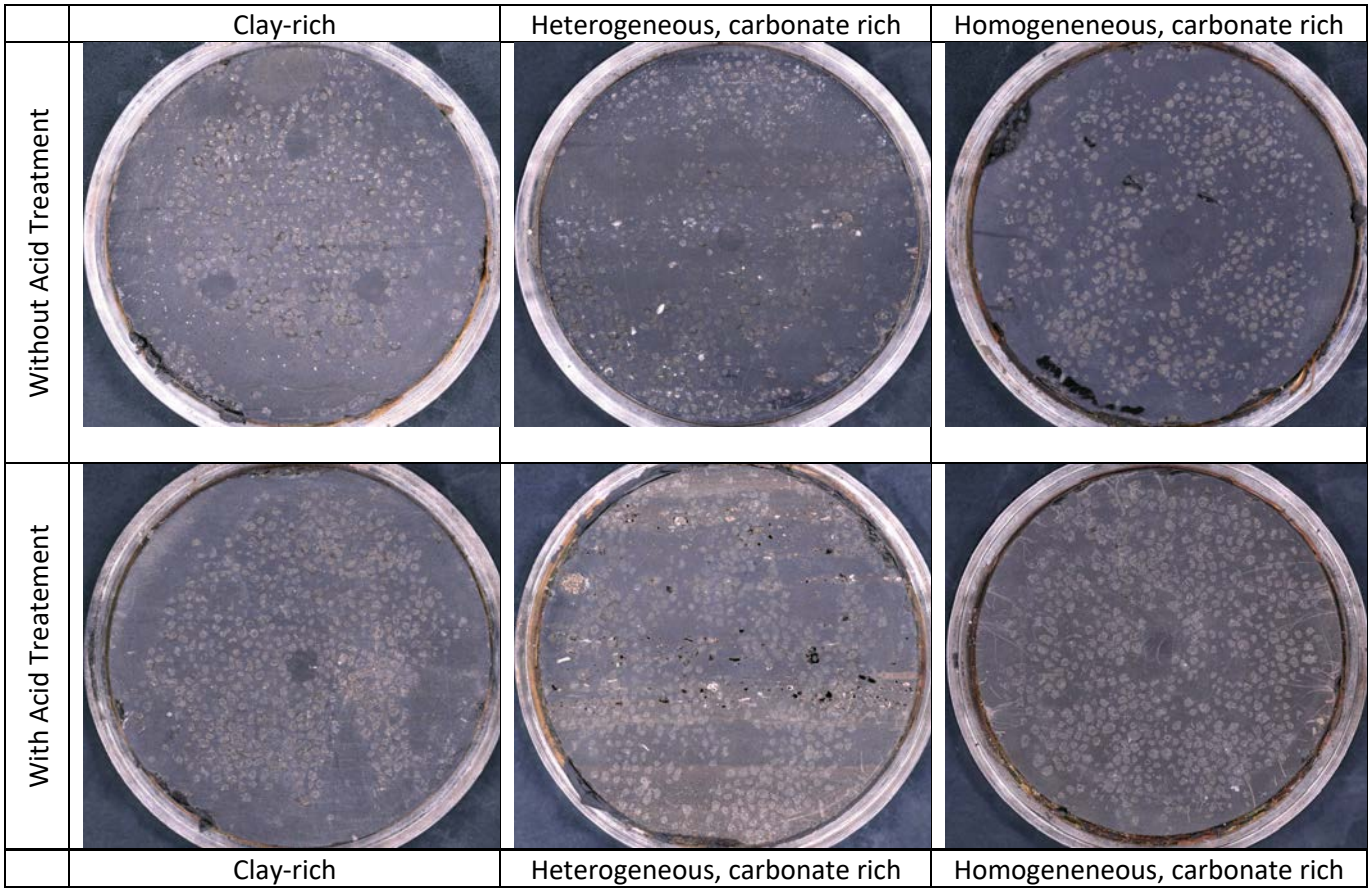

Figure 6.23: Photographs of the sample surfaces after the 2-week compaction experiment. The loose proppant and debris have been removed.

The results of this analysis are summarized in **Figure 6.24** and **Table 6.4**. Overall, the numbers are similar for all six samples, indicating PSI=15−20%. However, notably, both carbonate-rich samples showed about 5% reductions in proppant crushing by the acid-treatment. Particularly, the heterogeneous carbonate-rich 3Pb

sample exhibited the highest survival rate (22.7%), exceeding those of the clay-rich samples 11Pa and 11Pb (21.0% and 18.2%, respectively). These results seem to indicate that the acid treatment did contribute to the reduction of proppant crushing, even the impact is not dramatic for the samples used in this experiment, which had relatively similar mineral compositions.

Table 6.4. Proppant survivability for each sample.

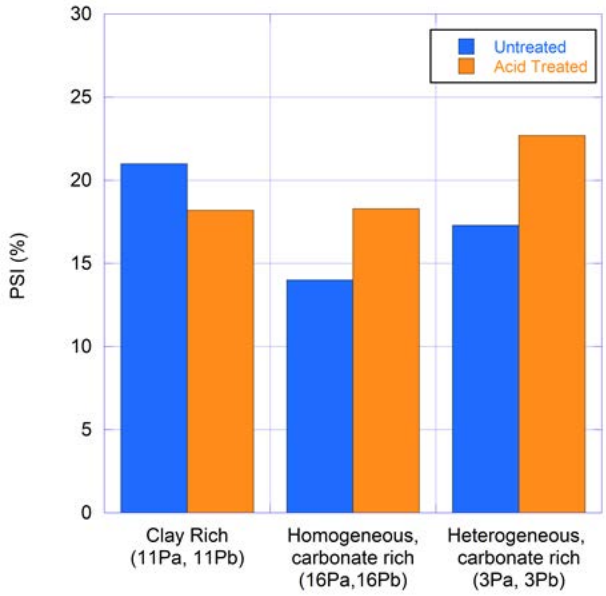

Figure 6.24: Comparison of Proppant Survivability Index (PSI) for all the samples. Although the overall values are similar (PSI=15-20%), notably, both carbonate-rich shales exhibited ~5% improvement in proppant crushing as a result of the acid treatment.

Table 6.4. Proppant survivability for each sample

Test	Sample	Total number of grains in image	Number of intact grains	Ratio (proppant survivability)
1	HFTS-3Pa	550	95	17.3%
2	HFTS-3Pb	577	131	22.7%
3	HFTS-11Pa	552	116	21.0%
4	HFTS-11Pb	560	102	18.2%
5	HFTS-16Pa	529	74	14.0%
6	HFTS-16Pb	563	103	18.3%

To investigate the impact of mineral types for acid-treated shale in more detail, we examined the proppant-shale interaction for the heterogeneous and carbonate-rich samples 3Pa and 3Pb. In **Figure 6.25**, clay-rich (blue shade), carbonate-rich (green shade), and pyrite (and also carbonate)-rich (yellow shade) zones in each sample which were identified via microscope are shown. The PSI values of the two samples which were determined for each mineralogical zone are then compared in **Figure 6.26**.

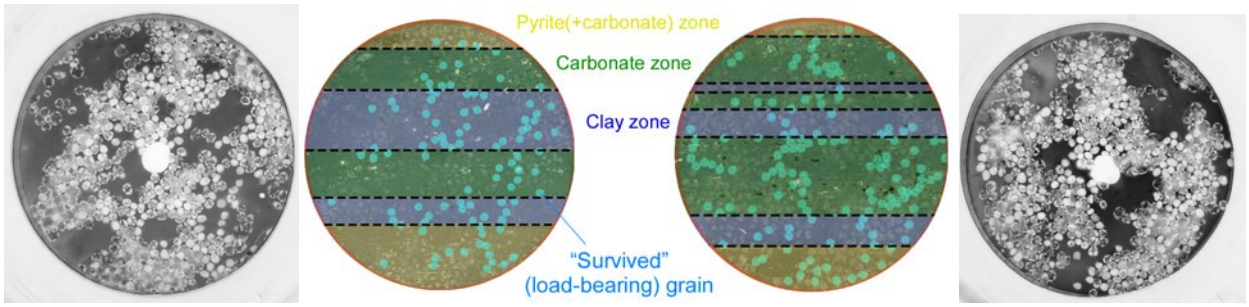

a. Sample 3Pa b. Sample 3Pb

Figure 6.25: For the HFTS 3Pa and 3Pb samples, microscope images are used to identify three-types of mineral zones [blue shade=clay-rich zones, green shade=carbonate-rich zones, and yellow shade= pyrite (and carbonate)-rich zones].

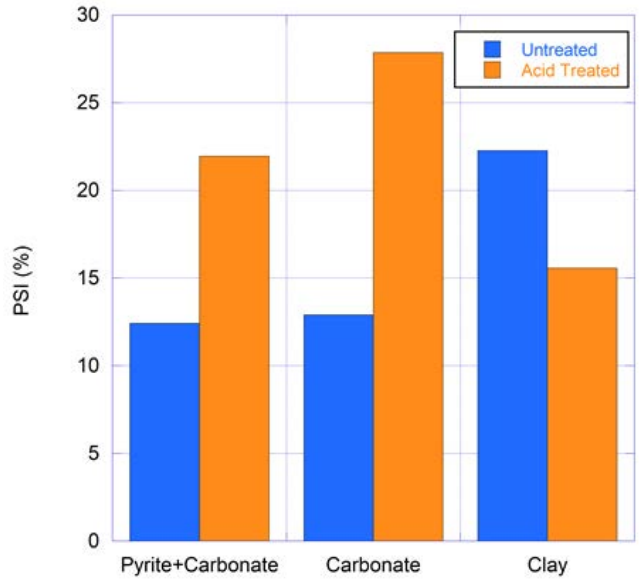

Figure 6.26: Comparison of PSI (the ratio of proppant grains which survived crushing) in each zone of dominant mineral type, between untreated and acid-treated HFTS-3P samples. For the untreated sample, higher ductility of clay resulted in higher survival rate. In contrast, for the acid-treated sample, increase in the ductility due to porosity increases may have resulted in the survival rate, while the transfer of the force to the clay-rich zone caused more proppant crushing there.

Compared to the results presented in **Figure 6.24**, the acid-induced changes in the proppant crushing behavior are more dramatic. Proppant grains and the shale matrix interacted differently for each mineralogical zone, as seen in the microscope images shown in **Figure 6.27**. Specifically, the increased near-surface porosity from dissolved carbonate grains caused enhanced proppant indentation, which indicates higher shale matrix ductility and less proppant crushing. The results of the analysis clearly show that:

- Carbonate-rich zones (pyrite + carbonate zones) show very low proppant survival rates (12-13%) in the untreated sample
- Carbonate-rich zones, especially the carbonate zone, show high survival rates (22-28%) in acid-treated sample
- Clay-rich zones exhibit a high survival rate (22%) in the untreated sample
- Clay-rich zone exhibits a reduced survival rate (16%) in the acid-treated sample, which is lower than in the untreated sample

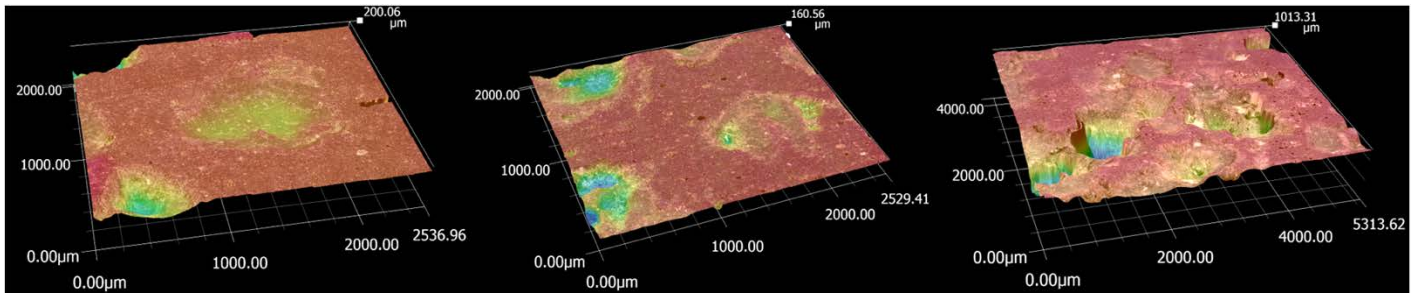

a. Clay-rich zone b. Pyrite + carbonate rich zone c. Carbonate rich zone

Figure 6.27: False-colored microscope images of HFTS 3Pb sample after the experiment, for locations with different shale-matrix mineralogy. Compared to the pyrite and carbonate-rich zones where acid treatment increased the matrix porosity, clay-rich areas showed smaller indentation depths. In the carbonate-rich section with large grains of carbonate minerals, acid treatment resulted in highly porous matrix which collapsed by indentation from proppant grains.

For the untreated sample, the relatively high grain survival rate in clay-rich zones can be explained by the higher compliance and ductility of the clay, compared to the more rigid and brittle carbonate-rich zones. In contrast, for the acid-treated sample, dissolution increases the porosity and ductility of the matrix and results in less grain crushing in the carbonate-rich zones as proppant is embedded into the matrix rather than crushed. This explains why the clay-rich zone has a survival rate even lower than the untreated sample. The grains in the clay-rich zone may have experienced an increased crushing force transferred from the acid-dissolved carbonate-rich zones.

6.2.4. Conclusions

In this task, we conducted a series of laboratory experiments on stress-dependent and time-dependent compaction of fractured Wolfcamp shale samples from the HFTS field laboratory. These tests examined propped fracture closure including the effects of shale minerology, heterogeneity, temperature, and acid treatment. Observations were made at the micro-scale using 4D X-ray microCT, and visually at the mesoscale. Acid treatment of carbonate-rich shales did not lead to dramatic differences in the fracture closure at either scale, although some minor effects were noted, including softening of the acid-treated layer, and a difference in rearrangement of proppant when stress was increased.

Detailed examination of the number of uncrushed proppant grains revealed that the acid treatment did indeed reduce proppant crushing where the carbonate in the shale matrix was dissolved. The reason for the reduced impact on fracture closure may be that a heterogeneous, acid-treated sample can experience increases in both embedment of proppant grains in the carbonate-rich zones and proppant crushing in clay-rich zones, which can increase the overall fracture closure. It is likely that such trade-off between proppant-embedment-induced and proppant-crushing-induced fracture closure displacements in acid-treated shale depends upon many parameters, including the distribution of minerals, degree of mineral dissolution and matrix heterogeneity which has been demonstrated by our experiment.

The results and observations of micro- and meso-scale examinations of the behavior of sub-monolayer propped shale fractures are useful for understanding proppant embedment under increasing effective stress (analogous to lowering fluid pressure after hydraulic fracturing), as well as the proppant survivability as a function of mineralogy and acid treatment. In addition to the unique and detailed physical descriptions of relevant processes, a key observation is that closure of fractures with sub-monolayer proppant distributions tends to follow a log-linear relationship. This means that initially fracture closure is most significant, yet continues over time, albeit at lower rates. Measurements upon which mathematical relationships of fracture closure for pristine and acid-treated carbonate-rich and clay-rich shale samples under sub-monolayer propped conditions can be extended into reservoir models. Although the exact conditions for these measurements may not be universally present, the log-linear nature of the relationship was consistently observed in the tests.

7. Micro-scale Reactions within Fractures and at Fracture-Matrix Interfaces

Chemical alteration at the fracture-matrix interface may alter the shale pore space and fracture permeability, thereby impacting long-term production of hydrocarbons from fractured shale reservoirs. Mineral dissolution and new mineral precipitation that occur during the shut-in period, as observed with prior laboratory-based experimentation (Li et al., 2020; Xiong et al., 2020), can result in alteration of flow paths in microfractures and along flow pathways in the primary fracture network (**Figure 7.1**). Knowledge of chemically-induced changes can be obtained through laboratory-based experimentation, as changes observed in the fractured reservoir are challenging to observe in field data generated during the production period.

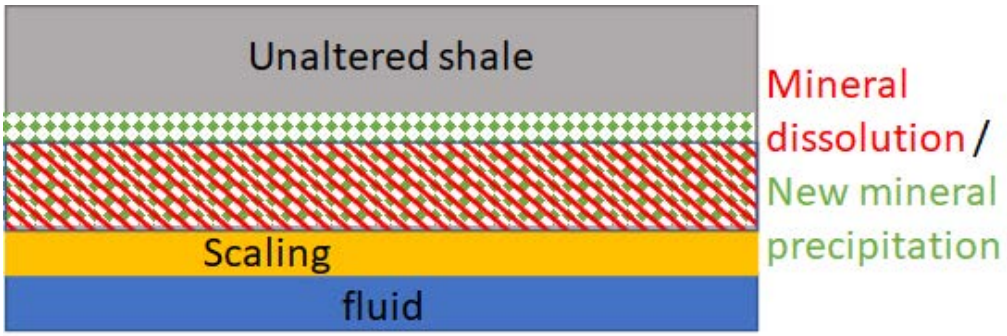

Figure 7.1: Schematic showing where mineral reactions may occur at the fracture-matrix interface in hydraulically-fractured shale reservoirs.

In a hydraulically-fractured reservoir, three major impacts to production may result from fluid-shale chemical interactions: (1) precipitation and scale development can disconnect micro-cracks, (2) precipitation and scale development can reduce mass transfer between fractures and shale matrix through development of a "skin" zone, and (3) the alteration can affect how fractures respond to mechanical changes, including proppant embedment and breaking, and thus fracture apertures during production (**Figure 7.2**). Below, we describe micro-scale experiments and modeling to evaluate mineral alteration impacts within the shale matrix and skin formation at the fracture-matrix interface (Sections 7.1 and 7.2) and then examine mineral alteration within fractures and impacts on fracture permeability.

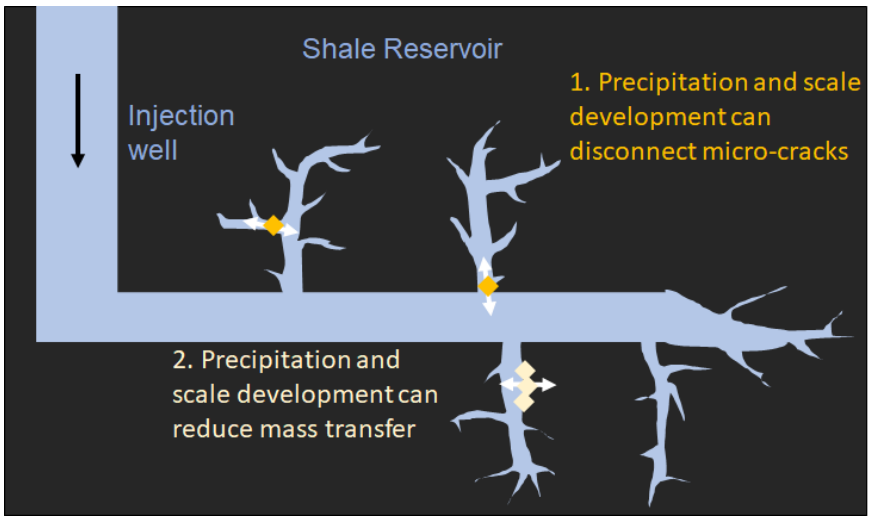

Figure 7.2: Schematic showing where fluid-shale chemical alteration is expected to affect flow in the reservoir.

7.1 Matrix Mineral Alteration and Skin Formation

This section describes experimental work done on Wolfcamp Shale to investigate reactions at the matrix surface and skin formation due to exposure with hydraulic fracturing fluids. The major observation are as follows:

- Hydraulic fracturing additives significantly alter shale mineralogy through the dissolution of carbonates, caused by the use of an acid spearhead, and new mineral precipitation.
- Experiments indicate that dolomite ($MgCa(CO_3)_2$) is more prone to dissolution via the acid spearhead than previously thought.
- New mineral precipitation when ultra clean water is used, isolation of additive impacts, is limited to Fe(III)-(hydr)oxide caused by the oxidation of Fe(II) from pyrite and other Fe(II) bearing phases such as clays and carbonates.
- Oxidized Fe precipitates dominate shale matrix precipitation.
- Fracturing chemicals result in a net reduction in permeability, both N_2 and decane, unless fracturing of the rock occurs.
- Rapid precipitation of skin can occur in both clay- and carbonate-rich rocks that effectively eliminates additional fluid penetration into the shale matrix.

Changes to Wolfcamp Shale (Ground Material) During Static Experiments:

Two Wolfcamp cores were selected for reaction with hydraulic fracturing fluid (clay-rich 25H and carbonate-rich 29H). For the purposes of this report, clay- and carbonate-rich is determined as having > 20 wt.% of their respective phases of clay or carbonate minerals. Two major types of samples were used, whole cores and shale material ground to 150-250 μm particle size and reacted with hydraulic fracturing fluid consistent with Midland Basin formulations (**Table 7.1**). These experiments were designed to identify the mineralogical changes that occur solely due to fracturing fluid additives and not the impact of base fluid (solution that additives and proppant are mixed) during a shut-in period of 3-weeks in which static fluid movement is assumed. Solutions were sequentially added to mimic field injection schedules and were incubated at 80 °C for 3-weeks at either 1 bar or 85 bar pressure depending on whether timed sampling of experiments were going to occur.

Table 7.1: Hydraulic fracturing recipe used for Wolfcamp experiments.

Ingredient	*Concentration (% mass)*
base fluid*	99.51
Kerosene	0.203
Methanol	0.064
2-Butoxyethanol	0.031
Potassium metaborate	0.019
Ammonium Persulfate	0.080
Gluteraldehyde	0.010
Guar Gum	0.007
Isopropanol	0.007
Propargyl Alcohol	0.007
2-ethyl-1-hexanol	0.007
Xylene	0.007
Polyphosphonic acids	0.007

Bulk mineralogical changes to the ground shale material showed significant reductions in clay material for the clay-rich shale, while the carbonates (both calcite and dolomite) were the primary mineral phases being

dissolved due to the acid spearhead (**Figure 7.3).** The dissolution of clay material in the clay-rich samples is also confirmed by the reduction of silicon and aluminum in the bulk XRF measurements of the unreacted/reacted samples while these values are fairly consistent for the carbonate-rich samples (**Figure 7.4(a)**). Both samples showed a reduction in Mg in the solids upon reaction indicating dolomite dissolution occurred in both sets of materials. Additionally, both sample types had detectable reductions in pyrite, particularly the carbonate-rich samples, suggesting a significant release Fe(II) into the system that can subsequently be oxidized and precipitated as Fe(III)-bearing phases in the shale matrix.

Solution data confirms rapid dissolution of both calcite and dolomite from the rock with the majority of Ca and Mg being released within the first 24 hours of experimentation (**Figure 7.4(b)**). Comparing the Ca/Mg solution results on a per mole concentration basis, it is seen that nearly all of the carbonate dissolved in the clay-rich samples is from dolomite while the carbonate-rich samples are a mixture of calcite and dolomite. These results show that dolomite is more reactive to the acid spearhead than previously thought.

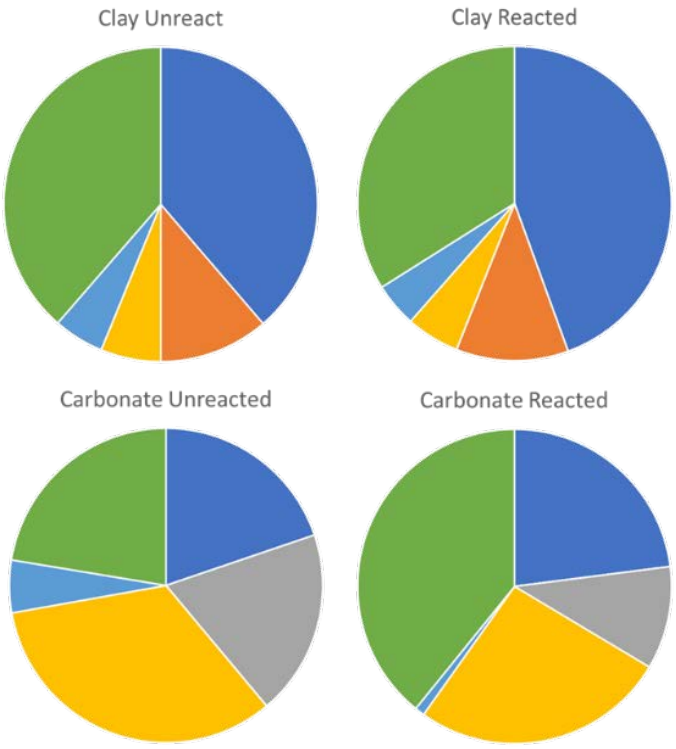

Figure 7.3: Semi-quantitative XRD analysis of unreacted and reacted Wolfcamp shale from clay-rich and carbonate-rich horizons. All clays are listed as illite and all feldspars are listed as albite.

New Matrix and Fracture Surface Precipitation:

As noted previously, detectable reductions in the amount of pyrite were detected in both sample types. Bulk mineralogy shows more pyrite dissolution in the carbonate-rich samples suggesting more Fe(III) precipitation in the shale matrix. Synchrotron-based X-ray Fluorescence (XRF) mapping shows that carbonate-rich samples did have significant Fe(III)-precipitation upon reaction with HFF (**Figure 7.5**). Bulk X-ray absorption spectroscopy (XAS) analysis of the ground material indicates that the primary Fe(III)-bearing phase for the carbonate-rich samples is hematite. The conversion of Fe(II)-bearing phases to Fe(III)-bearing phases is important since on a per atom basis, the oxidized Fe phases have a volume increase between 20 and 30% which can significantly impact whole rock permeability.

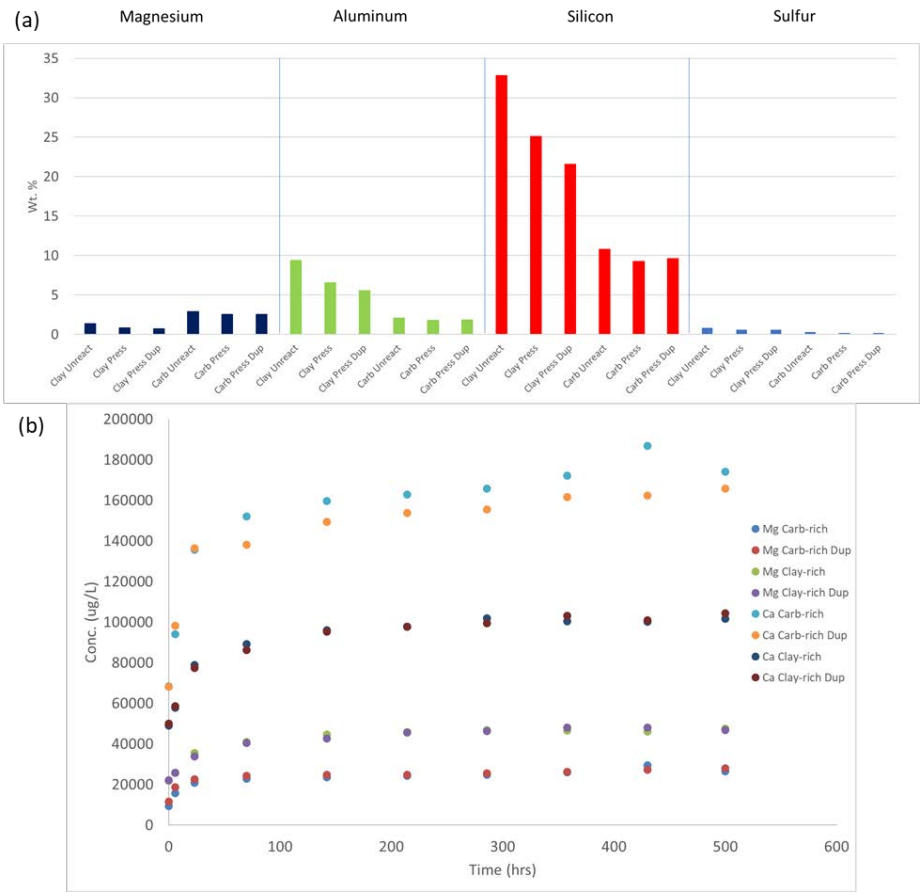

Figure 7.4: (a) Bulk XRF data for select elements for unreacted and reacted clay-rich and carbonate-rich samples; and (b) Calcium and Mg solution values for Timed reactors.

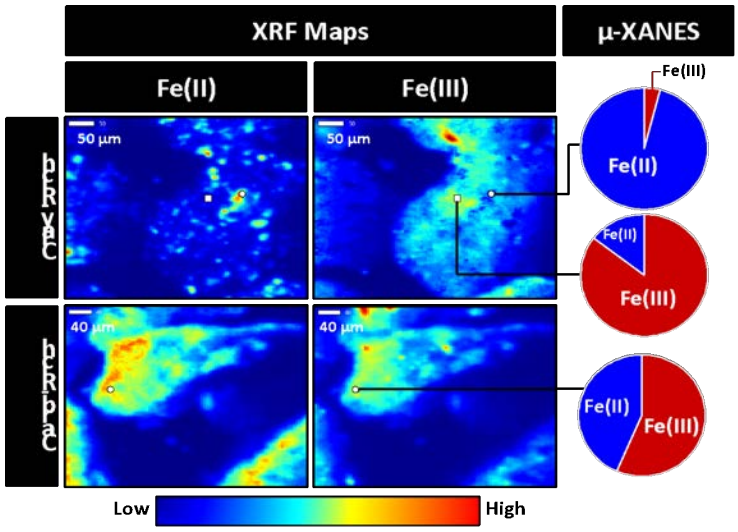

Figure 7.5: XRF mapping of Fe(II) and Fe(III) for reacted Wolfcamp shale. Significant Fe oxidation was seen in both sample types. Carbonate-rich samples had no detectable Fe in solution throughout the experimental time while clay-rich had measurable Fe in solution. Fe(III) bearing phases are primarily hematite, goethite, and magnetite, while clay-rich consisted of lower crystalline ferrihydrite, goethite, and magnetite.

Whole Rock Permeability Alterations:

Unreacted and reacted cores were measured for both N_2 and decane (crude oil analog) permeability. Unsurprisingly, core samples had lower permeability to decane versus nitrogen gas measurements. Unless cracks developed in the cores during experimentation, there was a net reduction in permeability for both measurement types (see this project's Apr.-June 2021 quarterly report). Due to the reduction in permeability, Br tracer studies on new cores from the same depth of the HFTS core were conducted to monitor fluid transport into the shale.

Bromide Tracer Studies on HFF Reacted Cores:

Two sets of whole core bromide tracer studies were conducted: 1) Wolfcamp core with simplified HFF recipe from the Marcellus shale play, and 2) Wolfcamp core using the fluid recipe previously described. Besides the HFF additives, solutions were spiked with 1M NaBr so that Br could be imaged either by XRF mapping or electron microprobe. Different cores were tested with various exposure times with fluid. XRF imaging of Wolfcamp cores reacted with a simplified HFF recipe (Marcellus shale) show significant Br penetration with time and dissolution of the matrix near the core surface. This indicates rapid imbibition of fluids in a scenario in which little to no precipitation is occurring (**Figure 7.6**). Conversely, in the clay-rich Wolfcamp cores in which new fractures did not develop, a new skin (20-50 μm developed rapidly, < 3 hours, that completely impeded flow of Br tracer into the shale core (Figure 7.7(a)). Note: Color mapping scales between **Figures 7.6 and 7.7** are different due to the different techniques being used for imaging, XRF imaging (**Figure 7.6**) and electron microprobe (**Figure 7.7(a)**). As seen from Figure 7.7(b), this rim is not seen in the Al map which clearly delineates the edge of the original core body and suggests that in this case the skin is a surface precipitation and not matrix infilling. Though, as previously mentioned, cracks in the core can increase overall whole core permeability, the presence of this new skin created through mineralogical reactions with HFF additives can have a significant deleterious impact on overall production through the restriction or complete cessation of flow through the altered layer. Additionally, the new skin can also form within newly formed cracks to inhibit access to the matrix. It is unlikely that this skin is prevalent enough to impact production within the first few months when the source of hydrocarbons is primarily the large fracture space and not derived from the matrix. This skin may play a major role in later production when hydrocarbon sources shift the major fracture space to production occurring from the secondary/tertiary fractures and matrix diffusion.

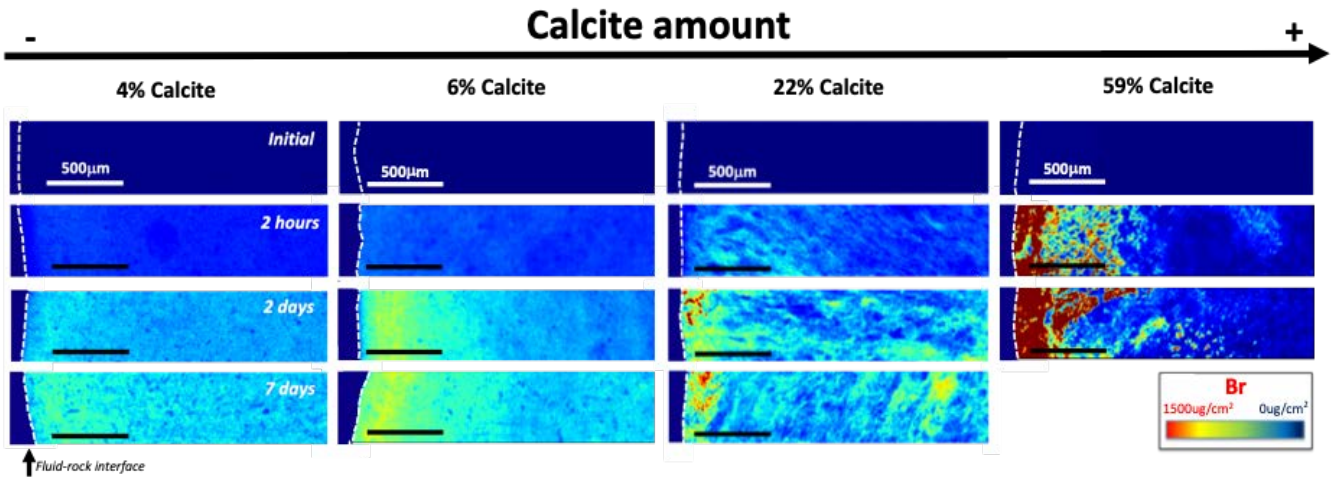

Figure 7.6: Synchrotron XRF mapping of bromide tracer in Wolfcamp shale reacted with a simpler HFF formulation used in the Marcellus shale play. Little to no new skin precipitated in these samples.

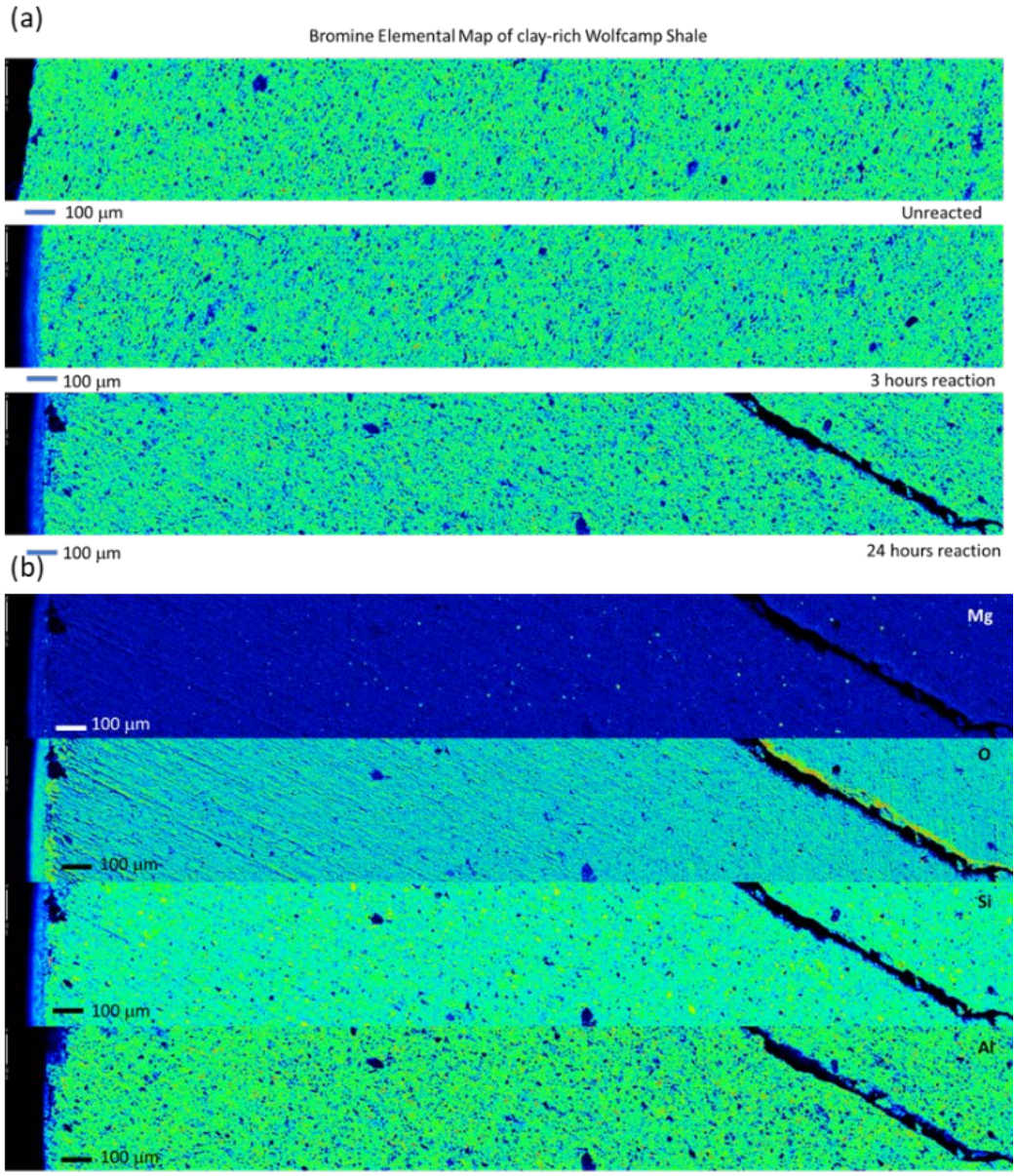

Figure 7.7: (a) Electron microprobe images of Bromine for unreacted (Top), 3 hours reaction (middle), and 24 hours reaction (bottom) for clay-rich Wolfcamp shale. No additional Br was detected in the interior of the shale when a 1 M NaBr tracer was included in the HFF solution. The low Br skin on the left side of the core is thought to prevent the penetration of solution into the core and thus no additional Br would be detected. (b) Electron microprobe imaging of Mg, O, Si, and Al for 24-hour reacted clay-rich Wolfcamp clay. Imaged region is similar to that for Br in bottom panel of (a). Of particular note is that in edge of the core is clearly defined in all 4 images with Al not being present in the skin. This provides evidence that this new skin is a precipitation of new material on the surface and not infilling of the original shale matrix.

7.2 Diffusive Transport in Unfractured and Fractured Shale

Fractures develop much of their geochemical characteristics by interaction with the shale rock matrix. Although flow into the rock matrix can occur due to strong pressure gradients and/or imbibition, much of the interaction involves molecular diffusion. To understand fracture sealing by mineral precipitation, it is essential to understand the rates at which molecular diffusion into the shale matrix occurs, since this determines both the kind of reaction products, but also their spatial distribution. For example, the common fracture filling barite may depend for its formation on the availability of sulfate in the shale matrix as well as barium present in the fracture fluids—interdiffusion then determines where the barite forms and how much there is. Or in other cases, the fracture fluids are close to equilibrium with respect to various secondary phases and may only require an increase in pH to precipitate phases that can plug the fracture and/or form a low permeability skin.

In order to understand the rates of secondary mineral formation affecting fracture permeability and fracture skin, it is important to carry out basic experiments to determine diffusion rates for different ions and neutral species in the Wolfcamp Shale, and to interpret these with a rigorous modeling approach. In this study, we carried out tracer experiments that included an anion (bromide), a cation (rubidium), and an uncharged tracer D_2O. As discussed extensively now in the literature, the presence of abundant clay in shales causes them to behave anomalously as compared to other subsurface materials. This is because of the negative surface charge of the clays and the nanoporosity separating these clay grains, which acts to partially exclude negatively charged anions while favoring the accumulation of the positively charged cations. The negative charge of the clay surface results in the formation of an electrical double layer, or diffuse layer, which is not electrically neutral as would be the case for bulk water or brine flowing through the fractures.

Anions are not only partially excluded in the electric double layer (EDL), which reduces the concentration that is available for transport though the nanopores of the shale, but also contributes to an increased tortuosity for anions because of the local blocking of all anion transport through pore throats where the EDL is overlapping. The combined effect of lower concentrations in the EDL and the increase in tortuosity results in significantly lower transport rates for the anions, and in some cases, complete blocking if mineral precipitation occurs (Chagneau et al., 2015).

Experimental Approach:

A diffusion cell approach similar to that used in Tinnacher et al. (2016) was used to study the rates of diffusion for multiple tracers through a 2 cm length of Wolfcamp Shale (**Figure 7.8**). The intact cylinder of Wolfcamp Shale was sealed with a rubber gasket pressurized to prevent leakage and flow along the exterior of the column. To prepare the D2O tracer, we used 0.500 mL D2O is equilibrated with 2L of ddi : H2O + D2O = 2HDO. Samples with deuterium concentrations ranging from ~0.014 mL/L (natural concentration) to ~0.039 (maximum concentration in the diffusion reservoir—concentrations are expected to vary linearly between this maximum value and the minimum value of natural composition).

Initial experiments were with DI water, later experiments with 0.5 M NaBr or 0.5 M RbCl at pH 5.5-6.0 (pH due to either the NaBr or RbCl) to provide an ion tracer. Concentrations of NaBr or RbCl will vary linearly between non-detectable and 0.5 M. To measure the D2O, we utilized a commercially available, off-axis integrated cavity output spectroscopy (OA-ICOS) laser absorption spectrometer (Los Gatos Research (LGR) Liquid Water Isotope Analyzer (LWIA- 24d)) for analysis of the 2H/1H and 18O/16O stable isotopes in liquid water.

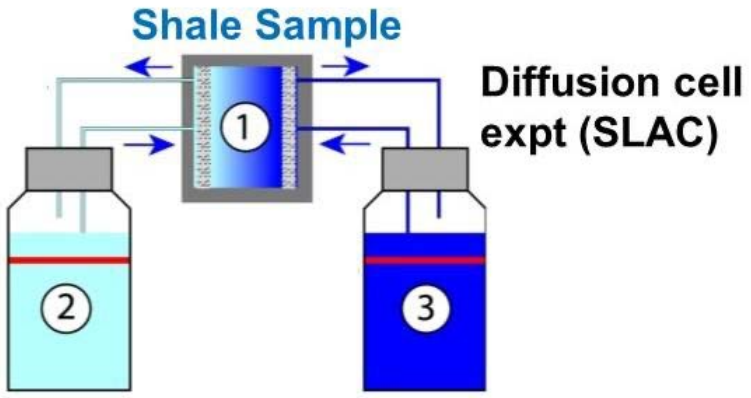

Figure 7.8: Schematic of diffusion cell experiment. A high concentration containing 0.5 M bromide (2) is located on the left, while a low concentration reservoir is maintained on the right. The shale sample is located in (1).

Modeling Approach:

CrunchClay was used for the simulation of the diffusion experiment, representing an evolving branch of the code CrunchTope/CrunchFlow (Steefel et al., 2015) that considers electrostatic effects associated on transport (Tournassat & Steefel, 2019a; Tournassat & Steefel, 2019b; Tournassat et al., 2020; Steefel & Tournassat, 2021). The electrostatic effects on transport include those associated with the development of a diffusion potential as captured by the Nernst-Planck equation, and the formation of a diffuse layer bordering negatively charged clay particles within which partial anion exclusion occurs. The model is based on a dual continuum formulation that accounts for diffuse layer and bulk water pore space, providing a more flexible framework than is found in the classical mean electrostatic potential models. The diffuse layer model is obtained by volume averaging ion concentrations in the Poisson-Boltzmann equation, but includes the treatment of longitudinal transport within this continuum. The calculation of transport within the bulk and diffuse layer porosity is based on a new formulation for the Nernst-Planck equation that considers averaging of diffusion coefficients and accumulation factors at grid cell interfaces (Tournassat et al, 2020).

A flexible representation of the pore space can be provided using a dual continuum approach (Tournassat & Steefel, 2019a). In this model, the pore space is divided into two compartments or continua, one corresponding to bulk water that is electrically neutral, and a second that is not electrically neutral and that is subject to the mean electrostatic potential required to balance the surface charge in the pores.

We define the fraction of the pore space subject to the mean electrostatic potential, f_{DL} as:

$$f_{DL} = \frac{V_{DL}}{V} \qquad \text{(Equation: 7.1)}$$

Where the volume of the diffuse layer, V_{DL}, can be defined as a multiple of the Debye length and the surface area of the clays

$$V_{DL} = \alpha_{DL} \lambda_D S \qquad \text{(Equation: 7.2)}$$

and where α_{DL} is an empirical multiplying factor.

Making use of the Nernst-Planck equation, we have developed a general form that is applicable to both compartments in the dual continuum (bulk water and diffuse layer) model described above and that accounts for ion mobility in porous media:

$$J_i = -u_i^{pm} C_{i,0} A_i \nabla \mu_i - u_{EP,i}^{pm} C_{i,0} A_i \nabla \psi_e \qquad \text{(Equation: 7.3)}$$

where ψ_e is the electrical potential in the fluid and as a result of a diffusion potential or external electric field, and not the mean electrostatic potential (Tournassat & Steefel, 2019a). A_j is an accumulation factor defined by:

$$C_j = C_{j,0} A_j \qquad \text{(Equation: 7.4)}$$

The value of accumulation factor, A_i, is defined for both the diffuse layer and bulk water as, respectively:

$$\begin{aligned} A_i &= \exp\left[-z_i \frac{F\psi_m}{RT} \right] \ : \ \text{Diffuse Layer} \\ A_i &= 1 \qquad\qquad\qquad\quad : \ \text{Bulk} \end{aligned} \qquad \text{(Equation: 7.5)}$$

where ψ_m is the mean electrostatic potential in the EDL porosity, z_i is the charge of the ion, F is the Faraday constant, R is the gas constant, and T is the absolute temperature

With the definition of the accumulation factor, the charge balance equation for the entire porosity (bulk and EDL) is given by:

$$\sum_i z_i \mathrm{F} \overline{c_{i,pore}} = \mathrm{F}\left(1 - f_{DL}\right) \sum_i z_i C_{i,0} + \mathrm{F} f_{DL} \sum_i z_i C_{i,0} A_{i,DL} = \mathrm{F} f_{DL} \sum_i z_i C_{i,0} A_{i,DL} = -Q_{DL} \qquad \text{(Equation: 7.6)}$$

Results:

Using a sample of unfractured Wolfcamp Shale, **Figure 7.9(a)** shows the typical anion exclusion behavior observed in many diffusion cell experiments (Soler et al., 2019). The anion diffuses from left to right through the Wolfcamp Shale sample at a rate that is about 2.5 to 3 times slower than the uncharged D_2O. This is due to the partial exclusion of the anion bromide in the clay-rich shale. As expected, the breakthrough of the D_2O in the low concentration reservoir on the right (3) occurs earlier than it does for bromide.

In contrast, an earlier experiment showed anomalous behavior that we attribute to the presence of microfractures in the shale. In this experiment, the bromide breaks through first (**Figure 7.9(b)).** And the total elapsed time to breakthrough (e.g, the time required for the concentration in the right reservoir to reach 0.00025, for example) is less than for the unfractured case shown in **Figure 7.9(a).** This suggests that in the experiment shown in **Figure 7.9(b),** a fast pathway is present where both tracers can diffuse more rapidly. But more interesting is the explanation for the early arrival of bromide, which was predicted theoretically in Steefel & Tournassat (2021), although that study involved flow. The fluid within the fracture represents electrically neutral bulk water where anion exclusion does not occur. The juxtaposition of this water with the shale matrix where anion exclusion occurs means that there is less diffusive loss of the anion relative to the D2O, thus there is less retardation. Again, this effect was predicted in Steefel & Tournassat (2021).

The presence of microfractures in this sample of shale is visible in a number of photographs, including that shown in **Figure 7.9(c**).

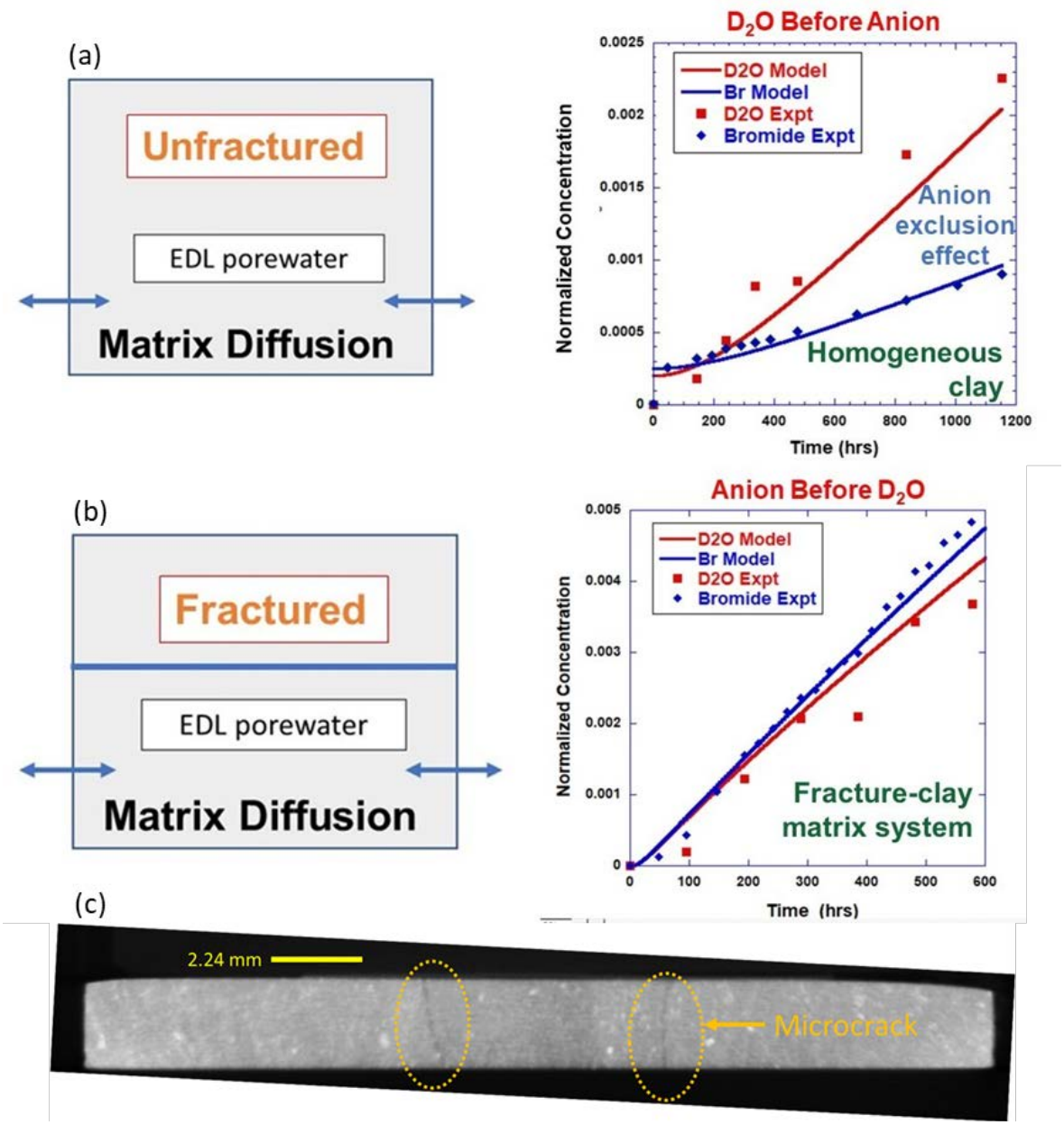

Figure 7.9: (a) Diffusion-only experiment using Wolfcamp Shale. Note the late and lower breakthrough of bromide compared to D_2O, a result attributable to anion exclusion in homogeneous clay-rich media. (b) Diffusion-only experiment using microfractured Wolfcamp Shale. Note the earlier breakthrough of bromide relative to D_2O, which can be attributed to the combination of the transport of bromide down the fracture as well as its exclusion from the clay-rich shale matrix. (c) Microfractures in a sample of Wolfcamp Shale used in diffusion experiment shown in (b).

7.3 Mineral Alteration in Fractures and Permeability Change

Experiments were designed to evaluate the location of mineral reactions that could impact primary fracture flow pathways through laboratory-based core flood experiments (**Figure 7.10**). These experiments were performed at 150 °F (66 °C), 1800 psi core pressure, 2000 psi confining pressure, 0.02 ml/min flow rate, and 12 days of reaction to simulate the shut-in period. Influent and effluent were sampled intermittently, and hydraulic fracturing fluid for the experiments was designed according to the HFTS fracturing fluid recipe. Experiments were performed with HFTS cores selected as part of the MMP core set, with high-clay and high-carbonate end members tested.

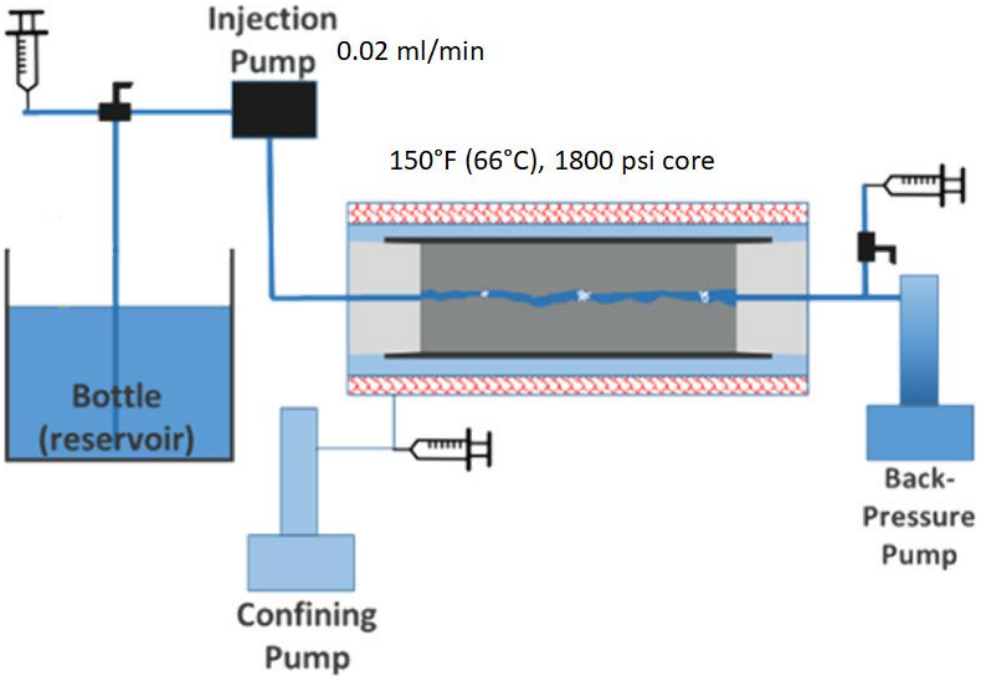

Figure 7.10: Schematic of core flood experimental apparatus used to evaluate mineral alteration along primary fracture flow pathways.

Factors that are expected to impact mineral reactions along flow pathways include: fracture surface geometry, flow rate and residence time of fluids, and mineral heterogeneity along flow pathways. Fractured pathways for fluid flow were generated using a modified Brazilian technique to generate rough fracture pathways (Hakala et al., 2017), and flow channels were milled into smooth fracture surfaces using a milling machine (**Figure 7.11**). The rough fracture experiments are expected to provide a greater representation of the reservoir fracture surface, however present challenges when trying to model reactive transport processes. The milled fracture experiments provide greater ease in modeling reactive transport processes, however may not provide the best representation of reactive mineral surfaces that are present in the fractured reservoir. Using results from both experiments increases confidence in understanding reactive transport processes that may impact permeability in hydraulically-fractured reservoirs.

Similar to the matrix-scale experiments, the core flood experiments performed with the clay-rich and carbonate-rich end member HFTS samples demonstrated that calcite dissolution and iron oxide precipitation are major mineral reactions observed (**Figure 7.11(a)**). The majority of change occurred within 1 mm of the fracture surface for the core flood experiments, which is also consistent with observations observed with the matrix-

scale experiments described above. The clay-rich sample primarily showed iron oxidation at the fluid-mineral contact and into the matrix, and the carbonate-rich sample showed both iron oxidation and calcium depletion at the fluid-mineral contact and into the matrix (**Figure 7.11(b)**).

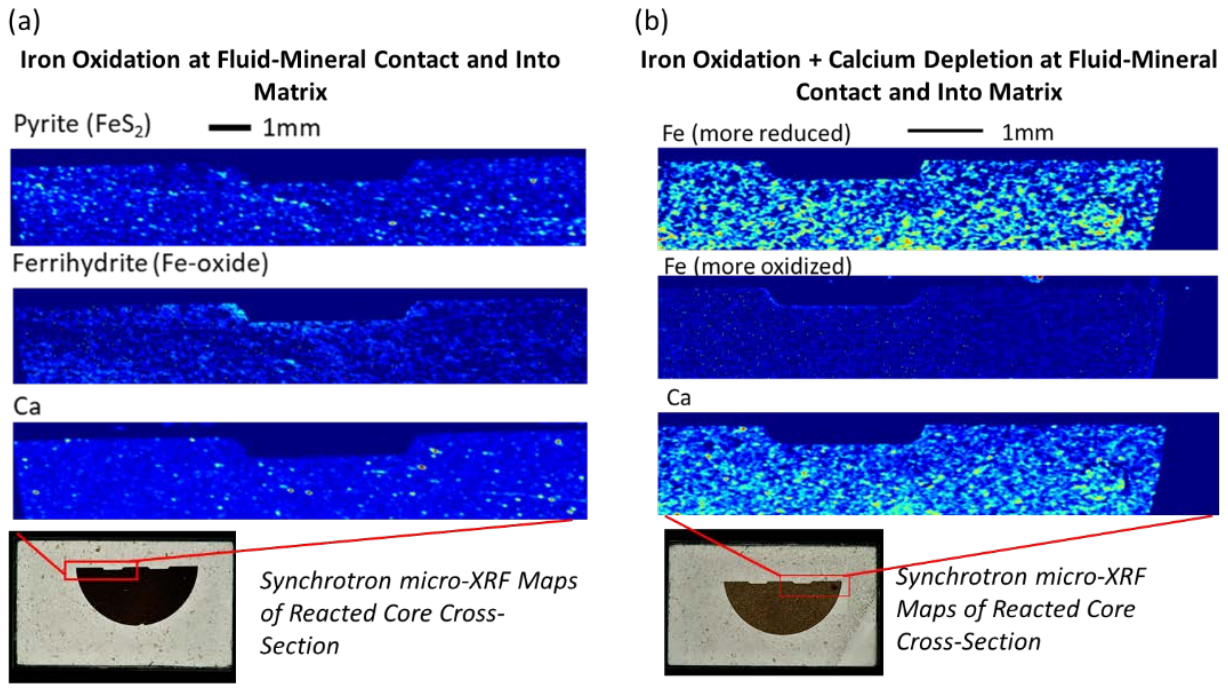

Figure 7.11: Synchrotron micro-x-ray fluorescence elemental maps from milled HFTS core flood experiments using (a) clay-rich and (b) carbonate-rich samples, respectively.

Simulations were performed with 2D cross-sections from the milled fracture experiments using the model framework detailed in Xiong et al. (2021). The flow rate, initial aperture size and influent chemistry follow the experiments. **Figure 7.12** shows the content (in volume fraction) of a few key primary and secondary minerals after 12 days of flow of HFF for the carbonate rich sample. The results highlight calcite dissolution and precipitation of Fe-bearing minerals as observed in the experiments. The layered structures illustrate the multiple reaction fronts for different minerals depending on local pH and reactivity. The comparison between the two columns highlights the role of a compact precipitation layer in controlling mass transfer. If the compact precipitation layer (or skin as referred to before) is considered (**Figure 7.12 (b,d,f)**), it slows down the mass transfer between the matrix and fracture significantly, as shown by the much less calcite dissolution.

The experimental studies from this project and previous work on Marcellus shale have suggested that scaling on the fracture surface can modify fracture permeability. The development of the scaling, however, varies significantly with the mineral composition and fluid chemistry. In the Wolfcamp fracture flow experiments, precipitates of hydroxyapatite were identified as a potential scaling product, whereas barite has been observed in other systems. In order to evaluate the dependence of potential permeability change on different physical conditions, a numerical test was performed with exaggerated hydroxyapatite precipitation. **Figure 7.13** shows permeability reduction as a result of mineral scaling with different initial fracture aperture and flow velocities for both clay-rich and carbonate-rich samples. The results show that the evolution of fracture permeability in the two mineral compositions are similar in the wider apertures, and the difference in mineral composition becomes more important when the fracture apertures are finer. It takes longer for the wider aperture to close to a certain point. In this case, the lower flow rate does not result in observable changes in permeability because the limited supply of the reactive fluid in the first place and it is expected to take much longer for observable changes.

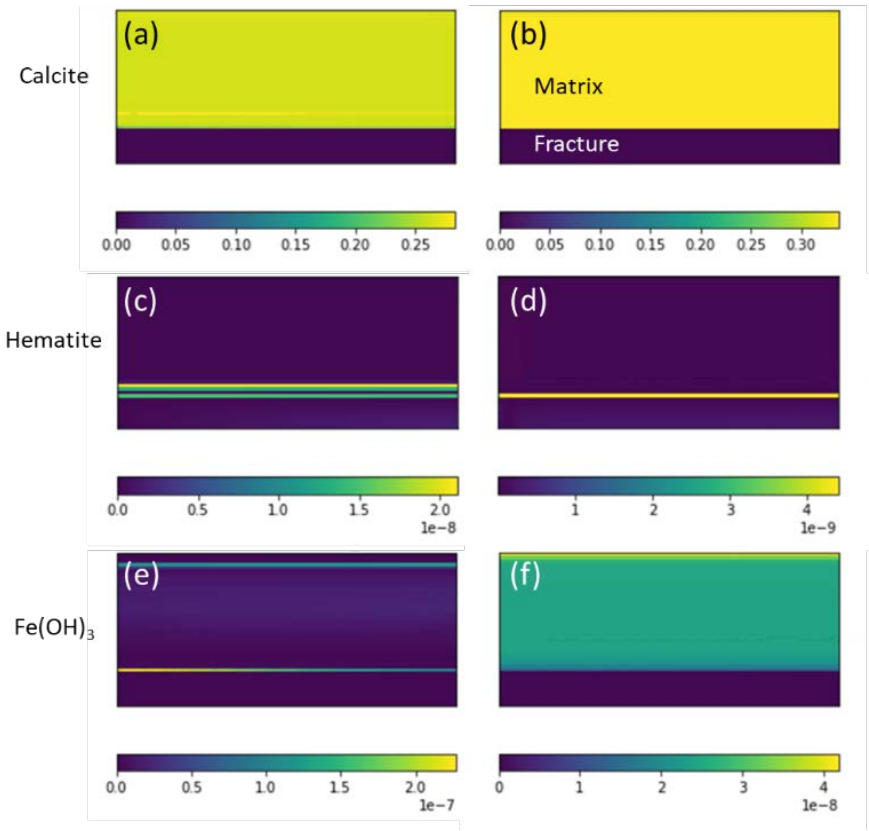

Figure 7.12: Volume fractures of (a-b) calcite, (c-d) hematite, and (e-f) ferrihydrite from simulations of core flood experiments with HFTS milled carbonate rich cores. The simulation of (b,d,f) allows compact precipitation layers to form, whereas the simulation of (a,c,e) does not.

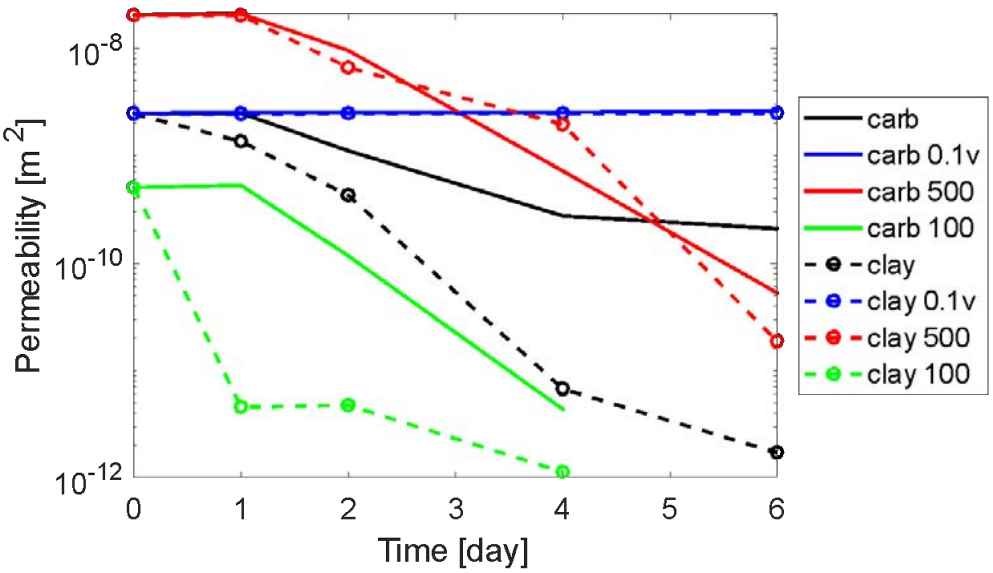

Figure 7.13: Simulated permeability evolution for both clay-rich and carbonate-rich mineral compositions in different initial fracture apertures and flow rates. In the legend, 100/500 are half aperture in microns, and 0.1v means the velocity is reduced by one order of magnitude compared to the experimental flow rate.

7.4 Micro-scale Chemistry Summary Observations

The combination of matrix and core flood experimentation, coupled with modeling of representative chemical-diffusion and reactive transport processes, provided insights on processes that may impact long-term hydrocarbon production from hydraulically-fractured shale reservoirs. Our integrated experimental and modeling study has shown clogging of microcracks and reduction of fracture-matrix exchange due to scaling. Diffusive fracture-matrix exchange rates were affected by a process of anion exclusion due to negatively charged clay surfaces in shale. A small amount of mineral scaling can reduce permeability significantly, where factors that impact permeability include: static experiments vs. fracture flow-through testing, mineralogy, fluid chemistry, and generation of microcracks. Future work to be performed includes: direct measurements of matrix permeability perpendicular to fracture face; detailed identification of skin composition, and relationship between mineral scaling and proppant interactions.

8. Summary and Conclusions

We have developed and demonstrated a new multi-scale simulation framework for unconventional stimulation and production in unconventional reservoirs. The framework comprises a seamless process for integrating a powerful geomechanical code for reservoir-scale stimulation (GEOS) with a high-performance multi-phase code for production (TOUGH+). To account for the impact of mechanical processes and chemical reactions occurring within individual fractures and at the fracture-shale interfaces, we have conducted micro-scale experimental and modeling studies and developed strategies to provide upscaled constitutive relationships for the reservoir scale models. We have tested the new modeling framework using field data and core samples from the HFTS, a recent field-based joint research experiment with intense monitoring of hydraulic fracturing and shale production in the Wolfcamp Formation in the Permian Basin, USA. Important achievements and findings are summarized below.

GEOS-TOUGH+ Integration

This project brought together two best-of-class HPC simulators for geomechanics (GEOS) and multiphase, multicomponent flow (TOUGH+). Coupling of these two simulators formed a highly efficient unified simulation framework for stimulation and production.

- To allow for seamless integration of the two simulators, we developed an automated procedure for coupling between the GEOS fracturing simulations and the TOUGH+ reservoir simulations.
- We then built high-resolution stimulation and production models for the HFTS field site and were able to demonstrate the overall efficiency of the simulation framework

Reservoir-Scale Stimulation Modeling

Fracture patterns observed from the HFTS show that fractures tend to propagate in groups, maintaining a dense spacing (i.e., they form so-called “fracture swarms”). These observations (which have been corroborated by other similar field experiments involving coring back) suggest that we needed to revise current conceptual models of stimulation and production in unconventional reservoirs. We developed a physics-based hydraulic fracturing model for the HFTS that achieved three main goals: (1) gain insights into key observations from the HFTS experiment, particularly the fracture swarms, (2) develop practical modeling methods to incorporate HFTS learnings, and (3) evaluate methods that can further optimize resource recovery.

- Based on statistical analysis and modeling of the HFTS data, we explored and evaluated possible mechanisms behind the observed fracture patterns.
- We developed a simplified way to model the effects of fracture swarming without the need to explicitly representing closely fractures in the mesh grid. This reduces the need for ad hoc parametric fitting. Our approach can readily be incorporated into existing simulators and has already been adopted by industry.
- Our 3D modeling of HFTS stages (including well trajectories and 3D reservoir structure) indicated that information known ahead of stimulation can be utilized to tailor pumping schedules to optimize fracture height, ensuring optimal resource usage for reservoir contact. This is in contrast with current state of practice where the same pumping schedule is typically used for each stage.
- Detailed modeling of near-wellbore processes suggests that fracture swarms originate in the near-wellbore region. The main implication of this finding is that the focus of well completion optimization should be on near-wellbore processes, including perforation clustering and phasing control, instead of the interactions with natural fractures.
- Our reservoir-scale hydraulic fracturing simulations produced complex three-dimensional fracture networks for the HFTS which were vetted against HFTS monitoring data and then handed over to the reservoir-scale production simulations.

Reservoir-Scale Production Modeling

The production model built for the HFTS deploys a multi-scale fracture network approach which explicitly accounts for non-uniform primary hydraulic fractures based on the GEOS model results while representing other fractures and the shale matrix with a multi-continuum model. Our sensitivity analysis pointed to three other important features of the model: (1) representation of non-uniform secondary fractures in addition to primary fractures, (2) a conductive "damage" zone near the well, and (3) stress-dependent fracture properties. The multi-scale model was tested on two production wells at the HFTS site, one located in the middle Wolfcamp formation and the other in the upper Wolfcamp formation. The goal of our modeling study was to advance knowledge in configuring a multi-scale fracture network for production simulations, to understand the role of primary vs. secondary fractures in multi-phase production, and to provide insights into selecting uncertain parameters and their transient behavior in direct comparison with the HFTS production data.

- We developed a procedure that imports the GEOS predictions of primary fracture geometry (number of fractures, location/shape, aperture) into the TOUGH+ model while maintaining both the detailed geometry of the stimulated zone (hydraulic fractures, stimulated natural fractures) as well as its internal state (spatial distribution of proppant, stress shadowing, etc.)
- We conducted a comprehensive sensitivity study to investigate the impact of multiple modeling and parameter choices on capturing the HFTS production behavior. In addition to fracture/well interference studies, we examined the effects of (1) uncertainties in initial shale permeability, (2) uncertainties in initial water and oil saturations, (3) degree and treatment of heterogeneity in the representation of the stimulated fractures, (4) changes in fracture permeability due to proppant rearrangement, embedment or breakage, (5) changes in fracture permeability due to chemical reactions to stimulation fluids, and (6) development of an altered (lower permeability) layer (skin) at the fracture-shale interface.
- We used the findings from micro-scale mechanics and reaction experiments on HFTS core samples to guide initial parameter selection for near-fracture and shale matrix properties. The micro-mechanical studies furthermore highlighted the importance of incorporating fracture closure into the production models to capture long-term production behavior.
- Our final model results demonstrate that production is driven by the combined conductivity and interplay of primary, secondary, and natural fractures. From comparison with HFTS data for oil, gas, and water production, we also learned that it is important to account for the non-uniform nature of primary and secondary fractures, and that transient fracture closure has an important impact on long-term production. Once these factors were accounted for, we achieved an excellent match between the production model and the HFTS data.

Experimental Studies on Fracture and Proppant Mechanics

We conducted a series of laboratory experiments on stress-dependent and time-dependent compaction of fractured Wolfcamp shale samples from the HFTS field laboratory. These tests examined propped fracture closure and studied the effects of shale minerology, heterogeneity, temperature, and acid treatment. Using a range of advanced testing methods, we made measurements over scales from single proppant grains to proppants layers interfacing with shale, under appropriate stresses and for both short and long timeframes.

- We developed and deployed a suite of new techniques to interrogate shale/proppant behavior such as 4D X-ray microCT at the micro-scale and visual observation at the mesoscale. These allowed direct imaging of time-dependent fracture closure as a result of micro-scale processes like proppant rearrangement, proppant embedment, or proppant crushing.
- Our experiments revealed a complex interplay between mechanical processes, shale mineralogy (carbonate-rich vs clay-rich HFTS samples), and potential presence of reactive fluids (such as acid hydraulic fracturing fluids). Overall, the impact of acid sample treatment on propped fracture behavior turned out to be relatively minor for HFTS samples.
- We examined the behavior of sub-monolayer propped fractures in HFTS shale under increasing effective stress states, to represent lowering of fluid pressure during production after hydraulic fracturing. A key

observation is that closure of fractures with sub-monolayer proppant distributions tends to follow a log-linear relationship. This means that initially fracture closure is most significant, yet continues over time, albeit at lower rates.

- We developed constitutive relationships of fracture closure as a function of stress for pristine and acid-treated carbonate-rich and clay-rich shale samples under sub-monolayer propped conditions. These were then used to inform the reservoir-scale production models.

Experimental Studies on Micro-scale Reactions within Fractures and at Fracture-Matrix Interfaces

Chemical reactions at the fracture-matrix interface may alter the shale pore space and fracture permeability, thereby impacting long-term production of hydrocarbons from fractured shale reservoirs. We conducted a comprehensive set of experimental and modeling studies on HFTS shale samples to evaluate the importance of micro-scale reaction processes occurring within the fractures, the shale matrix, and at the fracture-fluid interfaces.

- A first set of experiments was conducted to investigate reactions at the matrix surface due to exposure with hydraulic fracturing fluids. We learned that hydraulic fracturing additives may significantly alter the mineralogy of HFTS shales through the dissolution of carbonates and through rapid mineral precipitation forming a skin zone at she matrix surface. These processes can lead to clogging of microcracks and strong reduction of fracture-matrix exchange due to scaling. The rapid precipitation which can occur in both clay- and carbonate-rich rocks effectively eliminates additional fluid penetration into the shale matrix.
- In order to understand the rates of secondary mineral formation affecting skin formation at the fracture-matrix interface, we (1) carried out tracer experiments to determine diffusion rates for different ions and neutral species in the Wolfcamp Shale and (2) interpreted these with a rigorous pore-resolved modeling approach. The tracer experiments included an anion (bromide), a cation (rubidium), and an uncharged tracer D_2O. We learned that the diffusive fracture-matrix exchange rates are affected by a process of anion exclusion due to negatively charged clay surfaces in the shale.
- We finally conducted core flood experiments to evaluate how mineral reactions and scaling on the fracture surfaces impact flow pathways along primary fractures. We learned that calcite dissolution and iron oxide precipitation were the major mineral reactions observed in both clay-rich and carbonate-rich HFTS samples; the majority of these alterations occurred within 1 mm of the fracture face. Such scaling can modify fracture permeability, the extent of which varies significantly with the mineral composition and fluid chemistry and remains hard to predict.

The above research effort has been a close collaboration of four of DOE's national labs, namely Lawrence Berkeley National Laboratory (LBNL), Lawrence Livermore National Laboratory (LLNL), National Energy Technology Laboratory (NETL), and SLAC National Accelerator Laboratory (SLAC). Together, we (1) tested and validated the geomechanical simulator GEOS to enable prediction of stimulated fracture network evolution and permeability enhancement, (2) developed an optimized workflow for reservoir-scale stimulation and production predictions linking GEOS and the multi-phase flow simulator TOUGH+, and (3) demonstrated how micro-scale experimental studies provide important information on transient fracture property changes to the reservoir-scale production models. The project has enhanced the utilization and integration of HFTS results through the application of advanced computational tools and in return has utilized the HFTS field data and HFTS core samples to validate and improve these computational tools. Given the project's focus on fundamental properties and upscaling workflows, its impact will be far-reaching: the new modeling framework can be used to provide a better predictive physics-based understanding of stimulation and production processes in various unconventional oil and gas projects beyond the HFTS application. In addition, the framework has broad applicability across multiple other subsurface applications where multi-phase flow and fracture mechanics are important, such as subsurface energy storage, geologic carbon sequestration, or geothermal energy production.

Acknowledgments

This work was performed under the auspices of the U.S. Department of Energy by Lawrence Berkeley National Laboratory (LBNL) under Award Number DE-AC02-05CH11231, by Lawrence Livermore National Laboratory (LLNL) under Contract DE-AC52-07NA27344, by the National Energy Technology Laboratory (NETL) under the Onshore Unconventional Resources Field Work Proposal (1022415), and by the SLAC National Accelerator Laboratory under contract DE-AC02-76SF00515. LBNL, LLNL, NETL, and SLAC appreciate the funding and guidance for this project provided by the U.S. Department of Energy, Office of Fossil Energy and Carbon Management. We also appreciate the valuable data and discussions with our HFTS partners, in particular with Jordan Ciezobka from the Gas Technologies Institute (GTI).

References

Adachi J., Siebrits, E., Peirce, A. & Desroches, J. (2007). Computer simulation of hydraulic fractures. *Int*ernational Journal of Rock Mechanics and Mining Sciences, 44(5):739-757. https://doi.org/10.1016/j.ijrmms.2006.11.006

Alalli A., Li, Q., Jew, A., Kohli, A., Bargar, J., Zoback, M. and Kovscek, A. (2018). Effects of hydraulic fracturing fluid chemistry on shale matrix permeability. Unconventional Resources Technology Conference, Houston, TX, USA, URTEC- 2881314-MS. https://doi.org/10.15530/URTEC-2018-2881314

Alramahi, B. & Sundberg, M.I. (2012). Proppant embedment and conductivity of hydraulic fractures in shales, ARMA Paper#12-291, 46th US Rock Mechanics / Geomechanics Symposium held in Chicago, IL, USA, 24-27 June. https://onepetro.org/ARMAUSRMS/proceedings/ARMA12/All-ARMA12/ARMA-2012-291/122313

Birkholzer, J.T., Morris, J., Bargar, J.R., Brondolo, F., Cihan, A., Crandall, D., Deng, H., Fan, W., Fu, W., Fu, P., Hakala, A., Hao, Y., Huang, J., Jew, A.D., Kneafsey, T., Li, Z., Lopano, C., Moore, J., Moridis, G., Nakagawa, S., Noël, V., Reagan, M., Sherman, C.S., Settgast, R., Steefel, C.I., Voltolini, M., Xiong, W. & Ciezobka, J. (2021). A new modeling framework for multi-scale simulation of hydraulic fracturing and production from unconventional reservoirs, special issue on: "Multiscale and Multiphysics Processes in Unconventional Formations 2020", *Energies,* 2021, *14*(3), 641, https://doi.org/10.3390/en14030641

Chagneau, A., Tournassat, C., Steefel, C. I., Bourg, I. C., Gaboreau, S., Esteve, I., Kupcik, T., Claret, F. & Schäfer, T. (2015). Complete restriction of 36Cl–diffusion by celestite precipitation in densely compacted illite. *Environmental Science & Technology Letters*, *2*(5), 139-143. https://doi.org/10.1021/acs.estlett.5b00080

Ciezobka, J., Courtier, J. & Wicker, J. (2018). Hydraulic Fracturing Test Site (HFTS) - Project overview and summary of results. Unconventional Resources Technology Conference, Austin, TX, USA, URTEC-2937168-MS. https://doi.org/10.15530/urtec-2018-2937168

Clarkson, C. R., Yuan, B., Zhang, Z., Tabasinejad, F., Behmanesh, H., Hamdi, H., Anderson, D., Thompson, J. and Lougheed, D. (2020). Evaluation of the impact of multi-phase flow on reservoir signatures in the Wolfcamp shale. *Journal of Natural Gas Science and Engineering*, 76, 103187. https://doi.org/10.1016/j.jngse.2020.103187

Computer Modelling Group Ltd. (CMG) (2018). Thermal & Advanced Processes Reservoir Simulator. *STARS User Guide*. Calgary, AB.

Courtier, J., Chandler, K., Gray, D., Martin, S., Thomas, R., Wicker, J. & Ciezobka, J. (2017). Best practices in designing and executing a comprehensive Hydraulic Fracturing Test Site in the Permian Basin. Unconventional Resources Technology Conference, Houston, TX, USA, URTEC-2697483-MS. https://doi.org/10.15530/URTEC-2017-2697483

Cui, G., Tan, Y., Chen, T., Feng, X., Elsworth, D., Pan, Z. & Wang, C., (2020). Multidomain two-phase flow model to study the impacts of hydraulic fracturing on shale gas production. *Energy & Fuels,* 34, 4273–4288. https://doi.org/10.1021/acs.energyfuels.0c00062

Duan K., Kwok C.Y., Zhang Q., et al (2020) On the initiation, propagation and reorientation of simultaneously-induced multiple hydraulic fractures. *Computers and Geotechnics* 117:103,226. https://doi.org/10.1016/j.compgeo. 2019.103226.

Fu, P., Cruz, L., Settgast, R.R., Moos, D., and Ryerson, F.J. (2015). Numerical investigation of a hydraulic fracture bypassing a natural fracture in 3D. The 49th US Rock Mechanics / Geomechanics Symposium, ARMA 15-1671, San Francisco, CA, USA, Jun. 28-Jul.1, 2015.

Fu, W., Morris, J.P., Fu, P., Huang, J., Sherman, C.S., Settgast, R.R., Wu, H. & Ryerson, F.J. (2021). Developing upscaling approach for swarming hydraulic fractures observed at Hydraulic Fracturing Test Site through multiscale simulations. *SPE Journal*, 26(5), 2670-2684. https://doi.org/10.2118/199689-PA

Gale, J.F.W., Elliott, S.J. & Laubach, S.E. (2018). Hydraulic fractures in core from stimulated reservoirs: core fracture description of HFTS slant core, Unconventional Resources Technology Conference, Midland Basin, West Texas, URTeC: 2902624-MS. https://doi.org/10.15530/URTEC-2018-2902624

Hakala, J.A., Crandall, D., Moore, J., Phan, T.T., Sharma, S, & Lopano, C.L. (2017). Laboratory-scale studies on chemical reactions between fracturing fluid and shale core from the Marcellus Shale Energy and Environmental Laboratory (MSEEL) site. Unconventional Resources Technology Conference, Austin, TX, USA, July 24-26, URTEC-2670856-MS. https://doi.org/10.15530/URTEC-2017-2670856

Hao, Y., Settgast, R.R., Tompson, A.F.B., Fu, P., Morris, J.P. & Ryerson, F.J. (2016a). Discrete fracture modeling of multiphase flow and hydrocarbon production in fractured shale or low permeability reservoirs. American Geophysical Union Fall Meeting, San Francisco, CA, USA. https://ui.adsabs.harvard.edu/abs/2016AGUFM.H54C..07H/abstract

Hao, Y., Settgast, R.R., Tompson A.F.B, Fu, P., Morris, J.P. & Ryerson, F.J. (2016b). The effect of fracture-matrix interactions on multiphase flow in fractured reservoirs — Development of a discrete fracture model. XXI International Conference on Computational Methods in Water Resources, CMWR 2016, Toronto, Canada.

Hao, Y., Settgast, R.R., Tompson, A.F.B. & Ryerson, F.J. (2017). Numerical evaluation of multiphase flow processes and their effects on hydrocarbon production in hydraulically fractured reservoirs. 9th International Conference on Porous Media & Annual Meeting, Rotterdam, The Netherlands.

Harrison, A.L., Jew, A.D., Dustin, M.K., Thomas, D.L, Joe-Wong, C.M., Bargar, J.R., Johnson, N.B., Brown Jr., G.E. & Maher, K. (2017). Element release and reaction-induced porosity alteration during shale-hydraulic fracturing fluid interactions. *Applied Geochemistry*; 82:47-62. https://doi.org/10.1016/j.apgeochem.2017.05.001

Huang, J., Morris, J.P., Fu, P., Settgast, R.R., Sherman, C.S. & Ryerson, F.J. (2018). Hydraulic-fracture-height growth under the combined influence of stress barriers and natural fractures. *SPE Journal*. doi: 10.2118/189861-pa

Iyer, J., Walsh, S.D.C., Hao, Y., & Carroll SA. (2018). Assessment of two-phase flow on the chemical alteration and sealing of leakage pathways in cemented wellbores. *International Journal of Greenhouse Gas Control*, Volume 69, February, Pages 72-80. https://doi.org/10.1016/j.ijggc.2017.12.001

Jew, A.D., Dustin, M.K., Harrison, A.L., Joe-Wong, C.M., Thomas, D.L., Maher, K., Brown Jr., G.E. & Bargar, J.R. (2017a). Impact of organics and carbonates on the oxidation and precipitation of iron during hydraulic fracturing of shale. *Energy & Fuels*, 31:3643-3658. https://doi.org/10.1021/acs.energyfuels.6b03220

Jew, A.D., Harrison, A.L., Kiss, A.M., Dustin, M.K., Joe-Wong, C.M., Thomas, D.L., Maher, K., Brown Jr., G.E., Cercone, D. & Bargar, J.R. (2017b). Mineralogical changes that control pore-scale shale-gas properties. Unconventional Resources Technology Conference, Austin, TX, USA July 24-26. URTEC-2708858-MS. https://doi.org/10.15530/URTEC-2017-2708858

Jew, A.D., Li, Q., Cercone, D., Maher, K., Brown Jr., G.E. & Bargar, J.R. (2018). Barium sources in hydraulic fracturing systems and chemical controls on its release into solution. Unconventional Resources Technology Conference, Houston, TX, USA, July 23-25, URTEC-2899671-MS. https://doi.org/10.15530/URTEC-2018-2899671

Jew, A.D., Bargar, J.R., Brownlow, J. & Laughland, M. (2020). Strontium behavior in Midland Basin unconventional reservoirs: the importance of base fluids. Unconventional Resources Technology Conference, Austin, TX, USA, July 20-22. URTEC-2020-3016-MS. https://doi.org/10.15530/urtec-2020-3016

Jimenez, B. A. L. &Aguilera, R. (2019). Physics-Based Fluid-Flow Modeling of Liquids-Rich Shale Reservoirs Using a 3D Three-Phase Multiporosity Numerical-Simulation Model. *SPE Reservoir Evaluation & Engineering*. 22 (04): 1501–1526. doi:10.2118/191459-pa

Kempka, T., Class, H., Görk,e U.J., Norden, B., Kolditz, O., Kühn, M., Walter, L., Wang, W. & Zehner, B. A. (2013). Dynamic flow simulation code intercomparison based on the revised static model of the Ketzin Pilot Site. *Energy Procedia*; 40: 418-427. https://doi.org/10.1016/j.egypro.2013.08.048

Kim, J. & Moridis, G.J. (2014). Gas flow tightly coupled to elastoplastic geomechanics for tight- and shale-gas reservoirs: material failure and enhanced permeability, *SPE Journal*, 19(12), 1100-1125. doi: 10.2118/155640-PA

Kim, J., Um, E.S. & Moridis, G.J. (2018). Integrated simulation of vertical fracture propagation induced by water injection and its borehole electromagnetic responses in shale gas systems, *Journal of Petroleum Science and Engineering*, 165, 13-27, January. doi: 10.1016/j.petrol.2018.01.024

Kohli, A. & Zoback, M.D. (2021). Stratigraphically controlled stress variations at the Hydraulic Fracture Test Site-1 in the Midland Basin, TX. Energies 2021, 14, In Press.

Lecampion, B.A. & Bunger, X.Z. (2018). Numerical methods for hydraulic fracture propagation: A review of recent trends. *Journal of Natural Gas Science and Engineering*; 49: 66-83. https://doi.org/10.1016/j.jngse.2017.10.012

Li, Q., Jew, A.D., Kiss, A.M., Kohli, A., Alalli, A., Kovscek, A.R., Zoback, M.D., Cercone, D., Maher, K., Brown Jr., G.E. & Bargar, J.R. (2018). Imaging pyrite oxidation and barite precipitation in gas and oil shales. Unconventional Resources Technology Conference, Houston, TX, USA, July 23-25, URTEC-290247-MS. https://doi.org/10.15530/URTEC-2018-2902747

Li, Q., Jew, A.D., Kohli, A., Maher, K., Brown Jr., G.E. & Bargar, J.R. (2019). Thickness of chemically altered zones in shale matrices resulting from interaction with hydraulic fracturing fluid. *Energy & Fuels*; 33:6678-6889. https://doi.org/10.1021/acs.energyfuels.8b04527

Li, Z., Sherman, C.S., Reagan, M.T., Moridis, G.J. & Morris, J.P. (2021) "Effects of heterogeneous fracture aperture on multiphase production from shale reservoirs," in review for *Transport in Porous Media.*

Li, Z., Reagan, M.T. & Moridis, G.J. (2022) "History-matching shale reservoir production with a multi-scale, non-uniform fracture network," *in preparation for submission to SPE Journal.*

Liu, Q, Jew, A.D., Brown, Jr., G. E., Bargar, J.R. & Maher, K. (2020). Reactive Transport Modeling of Shale-Fluid Interactions after Imbibition of Fracturing Fluids. *Energy & Fuels*; 34, 5, 5511-5523. https://doi.org/10.1021/acs.energyfuels.9b04542

Iyer, J., Walsh, S.D.C., Hao, Y. & Carroll, SA. (2018). Assessment of two-phase flow on the chemical alteration and sealing of leakage pathways in cemented wellbores. *International Journal of Greenhouse Gas Control*, Volume 69, February, Pages 72-80. https://doi.org/10.1016/j.ijggc.2017.12.001

McClure, M., Picone, M., Fowler, G., Ratcliff, D., Kang, C., Medam, S. & Frantz, J. (2020). Nuances and frequently asked questions in field-scale hydraulic fracture modeling. SPE Hydraulic Fracturing Technology Conference and Exhibition, The Woodlands, TX, USA, 4-6 February, SPE-199726-MS. https://doi.org/10.2118/199726-MS

Moridis, G.J. & Pruess, P. (2014). User manual of the TOUGH+ v1.5 core code: A general purpose simulator of non-isothermal flow and transport through porous and fractured media. Lawrence Berkeley National Laboratory Report, LBNL-6869E. https://tough.lbl.gov/assets/files/02/documentation/TH_Manual_v1.5s.pdf

Nakagawa, S. & Borglin, S.E. (2019). Laboratory in-situ visualization of long-term fracture closure and proppant embedment in brittle and ductile shale samples. 53rd US Rock Mechanics/Geomechanics Symposium, New York, NY, USA, 23–26 June, ARMA-2019–1996. https://onepetro.org/ARMAUSRMS/proceedings-abstract/ARMA19/All-ARMA19/ARMA-2019-1996/125115

Olorode, O.M., Freeman, C.M., Moridis, G.J. & Blasingame, T.A. (2013). High-resolution numerical modeling of complex and irregular fracture patterns in shale gas and tight gas reservoirs, *SPE Reservoir Evaluation & Engineering*; 16(4):443-455, SPE-152482-PA, https://doi.org/10.2118/152482-PA

Raterman, K. T., Farrell, H. E., Mora, O. S., Janssen, A. L., Gomez, G. A., Busetti, S., et al. (2018). Sampling a stimulated rock volume: An eagle Ford example. SPE Reservoir Evaluation and Engineering, 21(4), 927–941. https://doi.org/10.2118/191375-PA

Raterman ,K.T., Liu, Y. & Warren, L. (2019). Analysis of a Drained Rock Volume: An Eagle Ford Example, URTeC 263, *Proc.* Unconventional Resources Technology Conference, Denver, Colorado, USA, 22-24 July 20. https://doi.org/10.15530/urtec-2019-263

Salahshoor, S., Maity, D. & Ciezobka, J. (2020). Stage-level data integration to evaluate the fracturing behavior of horizontal wells at the Hydraulic Fracturing Test Site (HFTS): an insight into the production performance. Unconventional Resources Technology Conference, Austin, TX, USA, July 20-22, URTEC-2020-3058-MS. https://doi.org/10.15530/urtec-2020-3058

Savitski, A.A. (2020) On a Poroelastic Nature of Multi-Stranded Hydraulic Fractures in Heterogeneous Unconventional Rocks. The 54th U.S. Rock Mechanics/Geomechanics Symposium, physical event cancelled, June 2020. ARMA-2020-1571. https://onepetro.org/ARMAUSRMS/proceedings/ARMA20/All-ARMA20/ARMA-2020-1571/447688

Sherman C. S., Aarons L.R., Morris J.P., Johnson S., Savitski A.A. & Geilikman M.B. (2015). Finite Element Modeling of Curving Hydraulic Fractures and Near-Wellbore Hydraulic Fracture Complexity. The 49th U.S. Rock Mechanics/Geomechanics Symposium, San Francisco, California, June. ARMA-2015-530

Settgast, R.R., Fu, P., Walsh, S.D.C, White, J.A., Annavarapu, C. & Ryerson, F.J. (2017). A fully coupled method for massively parallel simulation of hydraulically driven fractures in 3-dimensions. *International Journal for Numerical and Analytical Methods in Geomechanics*; 41(5):627-653. https://doi.org/10.1002/nag.2557

Sherman, C.S., Mellors, R., Morris, J.P. & Ryerson, R. (2019a) Geomechanical modeling of distributed fiber-optic sensor measurements. *Interpretation*; 7(1):SA21-SA27. https://doi.org/10.1190/INT-2018-0063.1

Sherman, C.S., Morris, J.P., Fu, P. & Settgast, R.R. (2019b). Recovering the microseismic response from geomechanical simulations. *Geophysics*; 84(4):1-45 https://doi.org/10.1190/geo2018-0184.1

Soler, J. M., Steefel, C. I., Gimmi, T., Leupin, O. X. & Cloet, V. (2019). Modeling the ionic strength effect on diffusion in clay. The DR-A experiment at Mont Terri. *ACS earth and space chemistry*, *3*(3), 442-451. https://doi.org/10.1021/acsearthspacechem.8b00192

Steefel, C.I. & Tournassat, C.A. (2021). A model for discrete fracture-clay rock interaction incorporating electrostatic effects on transport. *Computational Geosciences*; 25, 395-410. https://doi.org/10.1007/s10596-020-10012-3

Steefel, C.I., Appelo, C.A.J., Arora, B., Jacques, D., Kalbacher, T., Kolditz, K., Lagneau, V., Lichtner, P.C., Mayer, K.U., Meeussen, J.C.L., Molins, S., Moulton, D., Shao, H., Simunek, J., Spycher, N., Yabusaki, S.B. & Yeh, G.T. (2015). Reactive transport codes for subsurface environmental simulation, *Computational Geosciences*, 19(3), 445-478. https://link.springer.com/article/10.1007/s10596-014-9443-x

Stegent, N. & Candler, C. (2018). Downhole microseismic mapping of more than 400 fracturing stages on a multiwell pad at the Hydraulic Fracturing Test Site (HFTS): discussion of operational challenges and analytic results. Unconventional Resources Technology Conference, Houston, TX, USA, July 23-25, URTEC-2902311-MS. https://doi.org/10.15530/URTEC-2018-2902311

Tinnacher, R. M., Holmboe, M., Tournassat, C., Bourg, I. C. & Davis, J. A. (2016). Ion adsorption and diffusion in smectite: Molecular, pore, and continuum scale views. *Geochimica et Cosmochimica Acta,* 177, 130-149. https://doi.org/10.1016/j.gca.2015.12.010

Tournassat, C.M. & Steefel, C.I. (2019a) Reactive transport modeling of coupled processes in nanoporous media. *Reviews in Mineralogy and Geochemistry* 85: 75-109. https://doi.org/10.2138/rmg.2019.85.4

Tournassat, C.M. & Steefel, C.I. (2019b). Modeling diffusion processes in the presence of a diffuse layer at charged mineral surfaces: a benchmark exercise. *Computational Geosciences*, 25, 1-18 and 1319-1336. DOI: https://doi.org/10.1007/s10596-019-09845-4

Tournassat, C. M., Steefel, C.I. & Gimmi, T. (2020). Solving the Nernst-Planck equation in heterogeneous porous media with finite volume methods: Averaging approaches at interfaces. *Water Resources Research* https://DOI.org/10.1029/2019WR026832

Voltolini, M., H. Barnard, P. Creux & J. Ajo-Franklin (2019), A new mini-triaxial cell for combined high-pressure and high-temperature in situ synchrotron X-ray microtomography experiments up to 400 degrees C and 24 MPa, *Journal of Synchrotron Radiation*, *26*(1), 238-243, doi:10.1107/S1600577518015606.

Voltolini, M. & Ajo-Franklin, J. (2020), Evolution of propped fractures in shales: The microscale controlling factors as revealed by in situ X-Ray microtomography. J. Pet. Sci. Eng. 2020, 188, 106861.

Voltolini, M., J. Rutqvist & T. Kneafsey (2021), Coupling dynamic in situ X-ray micro-imaging and indentation: A novel approach to evaluate micromechanics applied to oil shale, *Fuel*, *300*, 120987, doi: https://doi.org/10.1016/j.fuel.2021.120987

Wan X, Rasouli V, Damjanac B, et al (2020) Coupling of fracture model with reservoir simulation to simulate shale gas production with complex fractures and nanopores. *J. Petroleum Science and Engineering* 193, 107422. https://doi.org/10.1016/j.petrol.2020.107422

Weijermars, R., Nandlal, K., Tugan, M.F., Dusterhoft, R., & Stegent, N. (2020). Wolfcamp Hydraulic Fracture Test Site drained rock volume and recovery factors visualized by scaled complex analysis method (CAM): emulating multiple data sources (production rates, water cut, pressure gages, flow regime changes, sand *b*-sigmolds). Unconventional Resources Technology Conference, Austin, TX, USA, July 20-22, URTEC-2020-2434-MS. https://doi.org/10.15530/urtec-2020-2434

Wu, Y., Cheng, L., Killough, J., Huang, S., Fang, S., Jia, P., Cao, R. & Xue, Y. (2021). Integrated characterization of the fracture network in fractured shale gas reservoirs—stochastic fracture modeling, simulation and assisted history matching, J*ournal of Petroleum Science and Engineering*, 205, 108886. doi:10.1016/j.petrol.2021.108886.

Xiong, W., Gill, M., Moore, J., Crandall, D., Hakala, J.A. & Lopano, C. (2020). Influence of reactive flow conditions on barite scaling in Marcellus Shale during stimulation and shut-in period of hydraulic fracturing. *Energy & Fuels*; 34(11): 13625-13635. https://doi.org/10.1021/acs.energyfuels.0c02156

Xiong, W., Deng, H., Moore, J., Crandall, J., Hakala, J. A. & Lopano, C. (2021). Influence of flow pathway geometry on barite scale deposition in marcellus shale during hydraulic fracturing, *Energy & Fuels*, 35 (15), 11947-11957. DOI:10.1021/acs.energyfuels.0c02156

Zakhour, N., Jones, M., Zhao, Y., Orsini, K. & Sahni, V. (2021). HFTS-2 Completions Design and State-of-the-Art Diagnostics Results, Unconventional Resources Technology Conference, Houston, Texas, USA, July 2021, URTEC-2021-5242-MS. https://doi.org/10.15530/urtec-2021-5242

Zhang, J., Ouyang, L., Hill, A.D. & Zhu, D. (2014). Experimental and numerical studies of reduced fracture conductivity due to proppant embedment in shale reservoirs, SPE-170775-MS, *Society of Petroleum Engineers Annual Technical Conference and Exhibition*, Amsterdam, the Netherland, 27-29, October. https://doi.org/10.2118/170775-MS

Zhang, K., Moridis, G.J., Wu, Y-S. & Pruess, K. (2008). A Domain decomposition approach for large-scale simulations of coupled processes in hydrate-bearing geologic media*, Proc.* 6th International Conference on Gas Hydrates, Vancouver, British Columbia, Canada, Country of Publication: United States. https://www.osti.gov/servlets/purl/949049